Advancements in Methodologies and Theories Regarding Model Membrane Environments by Total Internal Reflection with Fluorescence Correlation Spectroscopy

by
Jamie Kay Pero

A dissertation submitted to the faculty of the University of North Carolina at Chapel Hill in partial fulfillment of the requirements for the degree of Doctor of Philosophy in the Department of Chemistry.

Chapel Hill
2006

Approved by:

Advisor: Professor Nancy L. Thompson

Reader: Professor Linda L. Spremulli

Reader: Professor James W. Jorgensen

ABSTRACT

Jamie Kay Pero: Advancements in Methodologies and Theories Regarding Model Membrane Environments by Total Internal Reflection with Fluorescence Correlation Spectroscopy
(Under the Direction of Nancy L. Thompson)

Total internal reflection with fluorescence correlation spectroscopy (TIR-FCS) was utilized to determine the diffusion coefficient of nine fluorescently labeled antibodies, antibody fragments, and antibody complexes approximately 85 nm from a planar membrane. The diffusion coefficient decreased with increasing molecular size over what would be expected from the Stokes-Einstein Equation. Theory was derived specific to use with TIR-FCS to describe spatially dependent diffusion near membranes. The decreased diffusion is likely due to increased frictional coefficients when molecules are in close proximity to membranes. This described spatially dependent diffusion could be one contributor to the nonideality observed in ligand-receptor kinetics at membranes.

A stacked phospholipid bilayer system was developed by utilizing the interaction between NeutrAvidin and biotin. A biotinylated bilayer was deposited on a substrate and then treated with NeutrAvidin. Finally, a second biotinylated bilayer was allowed to adsorb and fuse atop the NeutrAvidin. This stacked bilayer system was characterized using epi-fluorescence, fluorescence pattern photobleaching recovery (FPPR), order parameter measurements, and atomic force microscopy (AFM). These techniques indicated that the stacked bilayer was relatively continuous but did exhibit some gaps where bilayer was missing. Fluorescence experiments indicated that the second bilayer was less fluorescent

than the primary bilayer. The stacked bilayer system will have application in multilayer systems and as a cushioning system. Other applications are likely forthcoming.

High refractive index substrates would be beneficial for application in TIR-FCS because they produce much shallower evanescent wave depths (18-43 nm) than fused silica (63-104 nm). It was verified that phospholipid bilayers can be formed upon TiO_2 and $SrTiO_3$. A second verification was required because conflicting reports were present in the literature. TIR-FCS was attempted upon these substrates with some success. The data were fit to a simplified version of the appropriate autocorrelation function. The data did autocorrelate, but the fit was extremely noisy and did not fit well at fast times (< 0.1ms). TiO_2 and $SrTiO_3$ were determined to be natively luminescent in the visible region with $SrTiO_3$ being about 6x more luminescent than TiO_2. Further investigations are required to fully amend the use of TiO_2 to TIR based techniques.

To Mom and Dad…..

Thanks for the love, support, financial aid

and occasional harassment (Dad).

And to Ellie Mae……

My constant companion in grad school

and the best beagle ever!!!

ACKNOWLEDGEMENTS

As I grow nearer to completing my thesis, I find myself growing more reflective and searching for some level of fruition for this chapter of my life. I realize at this time that I cannot separate the work and the role of graduate student from who I inherently am. I have come to a type of symbiotic relationship between me and my research. Consequently, those who I am thanking now, I am thanking for molding me into who I am today.

I would like to begin with my advisor. When I look back to four years ago I am embarrassed at how naïve and rough I was. I had no clue what I was going to learn personally and professionally in the next part of my life. It takes special people to do that year after year, individual by individual. So, Nancy, thank you for allowing me to screw up and grow up.

And mom and dad….you know me better than any other people on this earth. You have seen the full range of my personality. You know the worst and the best of me. And yet you are still there for me, encouraging me on and seeing talent that I don't believe is there. From spelling bees to drama play and on to thesis'……you've always thought I could move mountains. I appreciate that unwavering faith in me and most of all the deep love. This PhD is as much yours as it is mine. I love you both.

To my brothers…..Occasionally you have thought I was nuts and high-spirited. Other times you've thought I was mischievous, but there you were riling me up and getting me going or lending a sympathetic ear. I love you all for different reasons. Jeremy, I admire your patience, heart, and awareness of that greater humanity that so few possess. Jeff, I love your competitive spirit, belief in yourself, and conquering attitude. Jordan, I am moved by your sensitivity, your HARD work, and the depth of your soul.

Thank you to my grandmothers. Neither of my grandfathers got to see me reach this point in their lives. But I am sure that they see this and that they know it is for them. Grandma Melba, Grandma Ann, Grandpa Pete, and Grandpa Rollie, you have laid the stepping stones that allowed me to get here. You might not see the big picture of all that you

have done. Please look at my accomplishments as a reflection of what your sacrifice has brought. I love you all!!!

To my friends……There are so many of you and so many reasons to thank you so I am going to keep this brief but know how much you have helped me to get to this point. If you hadn't talked me through so much of this, I don't know that I would be here. Thank you to Emily and Kristin for dancing in lab, yogurt runs, the spice girls, and our "infamous" lab talks. Thank you to Patricia for taking me in my first year and giving me an instant group of friends. I truly appreciate our friendship. Here's to Italy!!! Thank you to Erin, Melissa, Katie, and Ginger for the occasional house fire and dinner party but especially for our "group counseling sessions." Thank you to Jenn for not seeing me as a nuisance our first year and always being willing to teach me things. Your friendship means a lot. Thank you also to Caia, Christie, Kalpana, Domenick, Becky, and everyone else. Chapel Hill would not have been the same without our adventures and our support system!!!

And finally thank you to Justin. I met you late in my graduate career. But you more than anyone else know what was put into this thesis. You saw me cry, worry, and wear myself out. And you still like me! Thank you for housing me, caring about me, and being willing to take a leap of faith. Please know that I see the deep goodness in you and your spirit. I am completely aware of how much I need you. Thank you also to Susan and Scooter Parker for allowing me to hibernate in their basement and providing food and computer paper during the writing of this thesis!

As for professional acknowledgements: thank you to Lisa Charlton, Julie Bryant, and Gary Pielak for assistance with the FPLC, Ashutosh Tripathy for help with the FPLC-DLS experiments, and Gerald. J. Sprangrude of the University of Utah for the 31-11 antibodies. Thank you to Emily Haas for her exceptional work on both the size dependent diffusion project and the high refractive index project (which she was the lead investigator on). Thank you to Ryan Fuierer of Asylum Research and Chuck Mooney of North Carolina State University for help with the AFM experiments. Thank you also to my mother, who reformatted all of my references for this thesis and did countless other tasks to help me finish this.

TABLE OF CONTENTS

LIST OF TABLES

LIST OF FIGURES

LIST OF ABBREVIATIONS

31-11	Type of IgG Antibody
1B711	Type of IgG Antibody
AbC	Antibody Complex
AFM	Atomic Force Microscopy
Biotin-cap-DPPE	1,2-Dipalmitoyl-*sn*-Glycero-3-Phosphoethanolamine-N-(Cap Biotinyl) (Sodium Salt)
Biotin-LC-DPPE	*N*-[6-[[Biotinoyl]Amino]Hexanoyl]-Dipalmitoyl-L-α-Phosphatidylethanolamine, Triethylammonium Salt
BS^3	Bis(sulfosuccinimidyl) suberate
dH_20	Deionized Water
DLS	Dynamic Light Scattering
DMSO	Dimethyl Sulfoxide
DNP	Dinitrophenyl
erfc	Complementary Error Function
Fab, $(Fab')_2$	Fragments of Antibodies that Bind Antigens and Determine their Specificity
FCS	Fluorescence Correlation Spectroscopy
FcγRII	Mouse Fc Receptor FcγRII
FITC	Fluorescein Isothiocyanate
FNA	Fluorescently Labeled NeutrAvidin
FPLC	Fast Protein Liquid Chromatography
FPPR	Fluorescence Pattern Photobleaching Recovery
FRET	Fluorescence Resonance Energy Transfer
Ig	Immunoglobulin

LB	Langmuir-Blodgett Bilayer Preparation
LS	Langmuir-Schafer Bilayer Preparation
Mar18.5	Type of IgG Antibody
MW	Molecular Weight
N.A.	Numerical Aperture
NBD-PC	1-Acyl-2-[12-(7-Nitro-2-1,3-Benzoxadiazol-4-yl) Aminododecanoyl]-Glycero-3-Phophocholine
PBS	Phosphate Buffered Saline
PMT	Photomultiplier Tube
POPC	1-Palmitoyl-2-Oleoyl-Glycero-3-Phosphocholine
SDS-PAGE	Sodium Dodecylsulfate-Polyacrylamide Gel Electrophoresis
STM	Scanning Tunneling Microscopy
SUV	Small Unilamellar Vesicles
TIR	Total Internal Reflection
TIR-FCS	Total Internal Reflection with Fluorescence Correlation Spectroscopy
VA-TIR	Variable Angle-Total Internal Reflection

LIST OF SYMBOLS

$< >$	time or ensemble average
a	stripe periodicity in the sample plane
A	solution concentration of a ligand
α	incidence angle of the laser beam (measured normal from substrate)
α	also the intercept (chapter 2)
α_c	critical angle for TIR
B	a measured constant in order parameter measurements
$\langle B \rangle$	average measured blank signal for TIR-FCS
β	the bleach fraction in FPPR
β	also the slope (chapter 2)
χ^2	the chi-squared statistical goodness of a fit
d	depth of the evanescent wave for TIR
D	diffusion coefficient
D_i	diffusion coefficient of the ith species in FPPR
δ	fluctuation in a quantity for TIR-FCS
$\delta F(t)$	fluorescence fluctuation at time t in TIR-FCS
$\delta(z-z')$	a Dirac delta function
	extinction coefficient or molar absorptivity
η	solvent viscosity
$\varphi(z,z',\tau)$	the concentration fluctuation autocorrelation function in TIR-FCS
f_i	the fraction of the fluorescence recovery associated with the ith species in FPPR
f_o	the resonant frequency in AFM

F_n	the F-statistic associated with the *n* species model
$F(t)$	instantaneous fluorescence intensity at time *t* in TIR-FCS and FPPR
$F(-)$	the pre-bleach fluorescence in FPPR
$F(\psi)$	the fluorescence as a function of beam polarization angle in order parameter measurements
$<F>$	temporally averaged fluorescence intensity for TIR-FCS
G_∞	baseline correction term for data fitting in TIR-FCS
$G(\tau)$	fluorescence fluctuation autocorrelation function
$G_e(\tau)$	autocorrelation function for diffusion through the evanescent wave
$G_s(\tau)$	autocorrelation function for diffusion through solution for FCS
γ	abbreviations for parameters in Stokes-Einstein Equation (Chapter 2)
γ	the dichroic factor in order parameter measurements
Ψ	the angle that the beam polarization makes with the incidence plane in order parameter measurements
h	observation area radius defined by aperture for TIR-FCS
I_o	maximum intensity of the evanescent field
$I(z)$	evanescent intensity
k	the spring constant in AFM
k_i	characteristic rate for the recovery of the *i*th species for FPPR
k	Boltzmann Constant
λ	vacuum wavelength of laser light
m_i	percent mobility associated with the *i*th species in FPPR
m_o	the mass that loads the spring in AFM
n	the number of fluorophore populations in FPPR

N	the number of data points for F-statistics
n_1, n_2	refractive index of substrate and water, respectively
N_e	average number of fluorescent molecules in the observation volume
N_s	average number of fluorescent molecules in the focused spot for FCS
$N(\theta)$	the orientation distribution of fluorophore absorption dipoles in order parameter measurements
r	hydrodynamic radius
P_i	Legendre Polynomial
p_i	the probability value with regards to the statistical goodness of a fit
R	the correlation coefficient with regards to the goodness of a fit
R_e	rate of diffusion through the evanescent wave for TIR-FCS
R_s	rate of diffusion through solution for FCS
s	the $1/e^2$-radius of the focused spot for FCS
s_i	the order parameter
S_e	initial slope of the autocorrelation function for diffusion through the depth of the evanescent intensity
S_s	initial slope of the autocorrelation function for diffusion through a focused spot for FCS
$\langle S \rangle$	average measured total fluorescence signal for TIR-FCS
σ	structure parameter in FCS
t	time
T	absolute temperature
τ	correlation time
z	distance in solution from interface

Chapter 1 Introduction

Throughout the centuries, science has proven itself a vast playground for the curious and imaginative. As man and womankind's understanding of the universe has grown through their investigations, most of the simple scientific principles have been deduced. The deduction of "simple" science has fueled a hunger for the more complex. As graduate students in science, we find ourselves embracing this complexity. Interfaces are at no loss for complexity. When two separate species or phases are forced into contact with each other, many interesting phenomena occur. This is where proven principles break down and boundary values reap their reason. Couple the inherent complexity of an interface to the doubly complex nature of biological material and you have a membrane.

The biological membrane mediates a myriad of functions, and it is the site of much of the interesting chemistry with regards to cellular function. Although many of the mysteries of the biological membrane remain to be discovered, it is known to play a central role in neurotransmission (Kim and Huganir, 1999), immunological response (Ravetch and Bolland, 2001), and nutrient uptake (Zorzano *et al.*, 2000). The membrane is central in many of these processes because it serves as a final gateway restricting what may enter and mingle with the fragile components inside the cell. It is this role as the gateway which also necessitates that the membrane be intrinsically linked to ligand-receptor interactions. Consequently, biological membranes are complex phospholipid bilayers containing integral transmembrane proteins (Wagner and Tamm, 2000), lipid rafts (Edidin, 2003; Lagerholm *et al.*, 2005), receptors (Lieto *et al.*, 2003) and a plethora of other relevant structures. The complexity of

the membrane impedes the elucidation of its properties. Resultantly, simplified model membrane systems have been employed in its study.

Several different techniques have been developed to make planar supported model phospholipid bilayers. The earliest attempts date back to the early 1900's when in 1918 Langmuir transferred a floating monolayer to a substrate (Stryer, 1995). This subsequently led to the development of the Langmuir-Blodgett (LB) and the Langmuir-Schaefer (LS) techniques in which a bilayer is created by the successive transfer of a monolayer to a substrate from the air/water interface (Wright *et al.*, 1988; Tamm and McConnell, 1985). In the 1980's the McConnell lab developed a simpler technique to produce phospholipid bilayers known as vesicle fusion (Brian and McConnell, 1984). In vesicle fusion, small unilamellar vesicles (SUVs) are produced by tip sonication. They are then allowed to adsorb and fuse to form a bilayer. Recent advancements have produced hybrids of the two techniques (Kalb *et al.*, 1992). The utility of phospholipid bilayers has seen extension beyond its use as a model membrane system. Phospholipid bilayers now find application in biosensors (Pompeo, *et al.*, 2005; Amenitsch et al, 2004), the biofunctionalization of inorganic solids (Sackmann, 1996), and immobilization of proteins and DNA (Pompeo *et al.*, 2005; Sackmann, 1996; Amenitsch *et al.*, 2004).

The continued use of phospholipid bilayers in experimental settings requires that the methodology continue to grow alongside the current needs in experiments. This requires the amendment of model membrane technology to increasingly complex and stringent requirements. One such current requirement is the production of "cushioning systems" for model membranes. The desire to produce cushioned membranes was born from several contributing factors including the need to shelter the membrane from the roughness of the

surface (Spinke *et al.*, 1992). Protecting the model membrane from the surface roughness creates more "fluid" membranes. Also, model membranes are currently limited in their ability to mimic the biological membrane because they do not allow transmembrane proteins to retain their lateral mobility (Wagner and Tamm, 2000; Sackmann, 1996; Naumann *et al.*, 2002; Kühner *et al.*, 1994; Wong, *et al.*, 1999; Huang, 1985; Spinke *et al.*, 1992). A cushioning system would limit interactions between the transmembrane protein and the substrate. This could possibly allow a transmembrane protein to have lateral mobility similar to that seen in biological membranes. Currently, several cushioning systems have been proposed (Wanger and Tamm, 2000; Sackmann, 1996; Naumann *et al.*, 2002; Kühner *et al.*, 1994; Wong, *et al.*, 1999; Huang, 1985; Spinke *et al.*, 1992). Many involve the use of polymers and ultra-thin polymer films (Sackmann, 1996).

A novel approach to the development of a cushioning system is to utilize the interactions of biotin and avidin to produce a stacked bilayer system. The utility of such a system would also see usage in multilayer applications. This stacked bilayer system has been constructed (see Chapter 3) by first depositing phospholipid vesicles containing a small fraction of biotin onto a fused silica substrate. The biotinylated vesicles are allowed to fuse at and adsorb to the substrate. Then NeutrAvidin (a commercially available derivative of avidin) is applied to the bilayer. Finally, biotinylated vesicles are applied atop this system and allowed to adsorb and become a bilayer. The primary bilayer and NeutrAvidin serve as the cushioning system atop which the secondary bilayer rests. The continuity and homogeneity of this system has been analyzed by fluorescence microscopy and atomic force microscopy.

Another area requiring advancement in membrane science is the theory surrounding ligand-receptor interactions near model or cellular membranes. As was aforementioned, the inherent gate-like nature of the biological membrane mandates that numerous different ligands diffuse up to and possibly bind to the membrane (Figure 1.1). The theory surrounding ligand-receptor interactions and their association/dissociation kinetics at membranes has never adequately modeled what is seen experimentally (Hsieh and Thompson, 1995; Payne *et al.*, 1997; McKiernan *et al.*, 1987; Anderson and McConnell, 1999; Sahu *et al.*, 2000; Domagala *et al.*, 2000). The deviations from expectation caused scientists to postulate that other factors influence ligand translational mobility in very close proximity to membranes (see Chapter 2). One such possibility is related to physical chemistry and the effect that the wall-like boundary of the membrane has upon the translational mobility of the ligand. If the close proximity of the membrane causes an increase in the frictional coefficient of the ligand, the diffusion coefficient will decrease from what was previously anticipated (Forster and Lauffenburger, 1994). One way to measure the effects that the close proximity of the membrane has upon the diffusion of the ligand would be to study ligand translational mobility as a function of ligand radii. If the membrane is effecting the diffusion of these ligands, the trend would manifest itself more for larger particles (Frej and Prieve, 1993; Bevan and Prieve, 2000; Lin *et al.*, 2000; Dufresne *et al.*, 2000; Pagac *et al.*, 1996; Pralle *et al.*, 1998; Sholl *et al.*, 2000; Oetama and Walz, 2005).

Figure 1.1 The Diffusing and Binding of Ligands at a Model Membrane.
The nature of the biological membrane requires that numerous different ligands diffuse up and bind to receptors embedded in the membrane. The membrane contains many different receptor types. This schematic represents a simplified version of what is occurring.

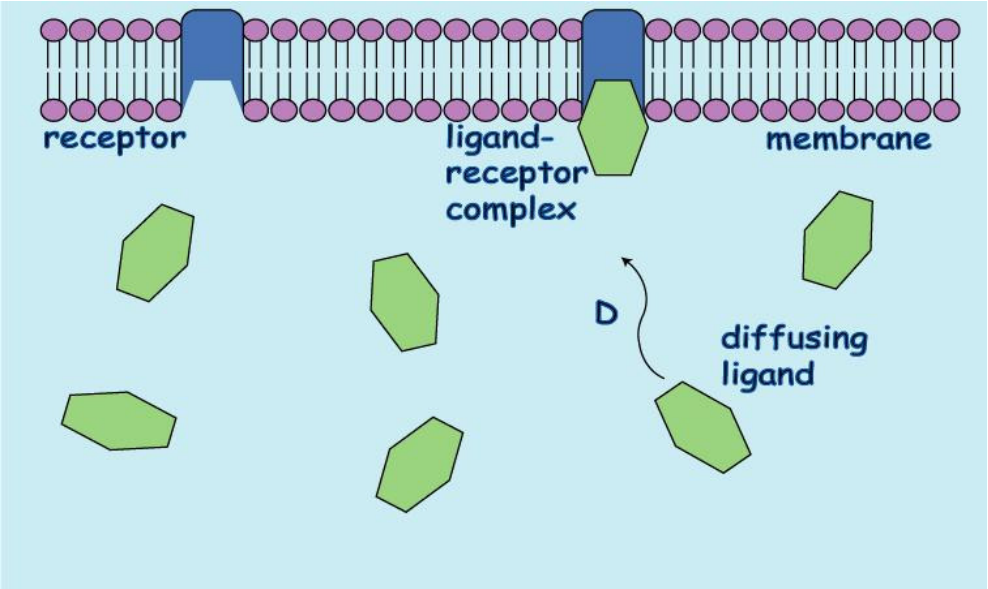

The study of diffusion and binding near model membranes requires specialization of existing techniques so that information gathered is specific to the interface and does not include information about bulk solution. One popular way in which this is done is by total internal reflection (TIR). Total internal reflection occurs when a plane wave traveling in a medium of higher refractive index (n_1) impinges on a planar medium of lower refractive index (n_2) at an angle (defined from the normal to the interface) greater than the critical angle (α_c)

$$\alpha_C = \sin^{-1}(\frac{n_2}{n_1}) \qquad (1.1).$$

During internal reflection, the plane wave completely reflects into the higher refractive index medium and a surface-associated evanescent wave is generated in the lower refractive index medium (Thompson and Pero, in press). The evanescent field propagates parallel to the interface and penetrates into the lower refractive index medium with a distance on the order

of the incident light wavelength. Resultantly, a small distance from the interface (63-104 nm at the fused silica/water interface) is selectively excited, and interactions in close vicinity to the model membrane can be probed. The depth of the evanescent wave is defined by

$$d = \frac{\lambda}{4\pi\sqrt{n_1^2 \sin^2 \alpha - n_2^2}} \tag{1.2}$$

where d is the evanescent wave depth, λ is the vacuum wavelength of light, and α is the incident angle of the light.

Total internal reflection has been combined with many fluorescence techniques to render them surface sensitive (Thompson and Pero, 2005). One such technique is fluorescence correlation spectroscopy (FCS). FCS first made its debut in 1974 when other correlation based techniques such as light scattering were being introduced (Elson and Magde, 1974; Elson, 1985). In FCS, a small observation volume is defined by placing an aperture (usually 50-200 μm in radius) at the confocal image plane of a microscope. By using this small observation volume to monitor a dilute fluorescently-labeled solution (~15-100 nM), temporal fluctuations in the measured fluorescence can yield information about the processes giving rise to these fluctuations (Thompson, 1991). These fluctuations can be caused by molecules moving into and out of the observation volume or changes in the fluorescent state of molecules (singlet to triplet and vice-versa) (Elson and Magde, 1974, Thompson, 1991; Gösch and Rigler, 2005; Fradin *et al.*, 2005). Consequently, FCS takes advantage of what effectively can be considered the inherent noise in a fluorescent measurement to derive information about the molecular motion and fluorescent properties of its participants. These fluctuations are then autocorrelated

$$G(\tau) = \frac{\langle \delta F(t+\tau)\delta F(t) \rangle}{\langle F \rangle^2} \tag{1.3}$$

where $F(t)$ is the instantaneous fluorescence intensity at time t, $\langle F \rangle$ is the average fluorescence intensity over the course of the experiment, τ is the correlation time, and $\delta F(t)$ (defined by $\delta F(t) = F(t) - \langle F \rangle$) is the fluorescence fluctuation. $G(\tau)$ decays monotonically with τ to zero at $\tau = \infty$. A number of recent reviews have been published describing FCS (Vukojevic *et al.*, 2005; Gosch and Rigler, 2005; Haustein and Schwille, 2004; Enderlein *et al.*, 2004; Pramanik, 2004; Weiss and Nilsson, 2004; Kahya *et al.*, 2004; Levin and Carson, 2004; Muller *et al.*, 2003; Hink *et al.*, 2003; Thompson *et al.*, 2002; Frieden *et al.*, 2002; Rigler and Elson, 2001).

In 1977 total internal reflection was combined with fluorescence correlation spectroscopy (TIR-FCS) in an instrument known as a virometer (Hirschfeld and Block, 1977; Hirschfeld *et al.*, 1977). The virometer was a rudimentary, proof-of-principle instrument that was devised to identify ethidium bromide stained viral molecules by their rate of diffusion through the evanescent wave. In 1981, TIR-FCS was brought to fruition and the theory was derived (Thompson *et al.*, 1981). The derivation of the theory for TIR-FCS paved the way for its application in biophysics. The advantages of using TIR-FCS as opposed to FCS are most profound for studying dynamic processes at interfaces (Figure 1.2). By using a TIR set-up, the technique becomes especially applicable to membrane science. However, there are additional advantages that are useful in other aspects. For instance, FCS measurements require that the area in which measurements be taken remain small. This is easily accomplished in the xy plane by placing an aperture at a confocal image plane in the path of light (Thompson, 1991). TIR increases the ability to limit sample observation volume by making it possible to specify the z-distance that is probed by changing the incidence angle of the impinging light (Eq. 1.2). Furthermore, although conventional solution-based FCS has

been used to study the kinetics of some systems, this type of FCS has some distinct disadvantages in this area of investigation. Using FCS to probe the kinetics of two ligands binding involved watching the change in the rate of translational diffusion upon binding. This is not optimum because to see significant changes in translational mobility the size increase upon binding must be of a significant magnitude, and this is rarely the case. TIR-FCS circumvents this problem by immobilizing a nonfluorescent ligand to the surface. Then a fluorescent ligand must diffuse into the evanescent wave and bind to a surface-immobilized ligand to elicit fluorescence, thus making kinetic investigations much more facile.

Figure 1.2 Total Internal Reflection with Fluorescence Correlation Spectroscopy. a) Light is totally internally reflected through a fused silica prism to selectively excite molecules near the interface. b) The experimental apparatus for TIR-FCS. After light is totally internally reflected, it is sent through a pinhole at the confocal image plane. Photons are measured by a photomultiplier tube and then autocorrelated. c) The measured fluorescent intensity displays temporal fluctuations in the signal commonly referred to as noise. d) The fluorescent fluctuations are autocorrelated. The fluorescent fluctuations yield information about the movement of molecules in close proximity to the membrane and about transitions in fluorescent state.

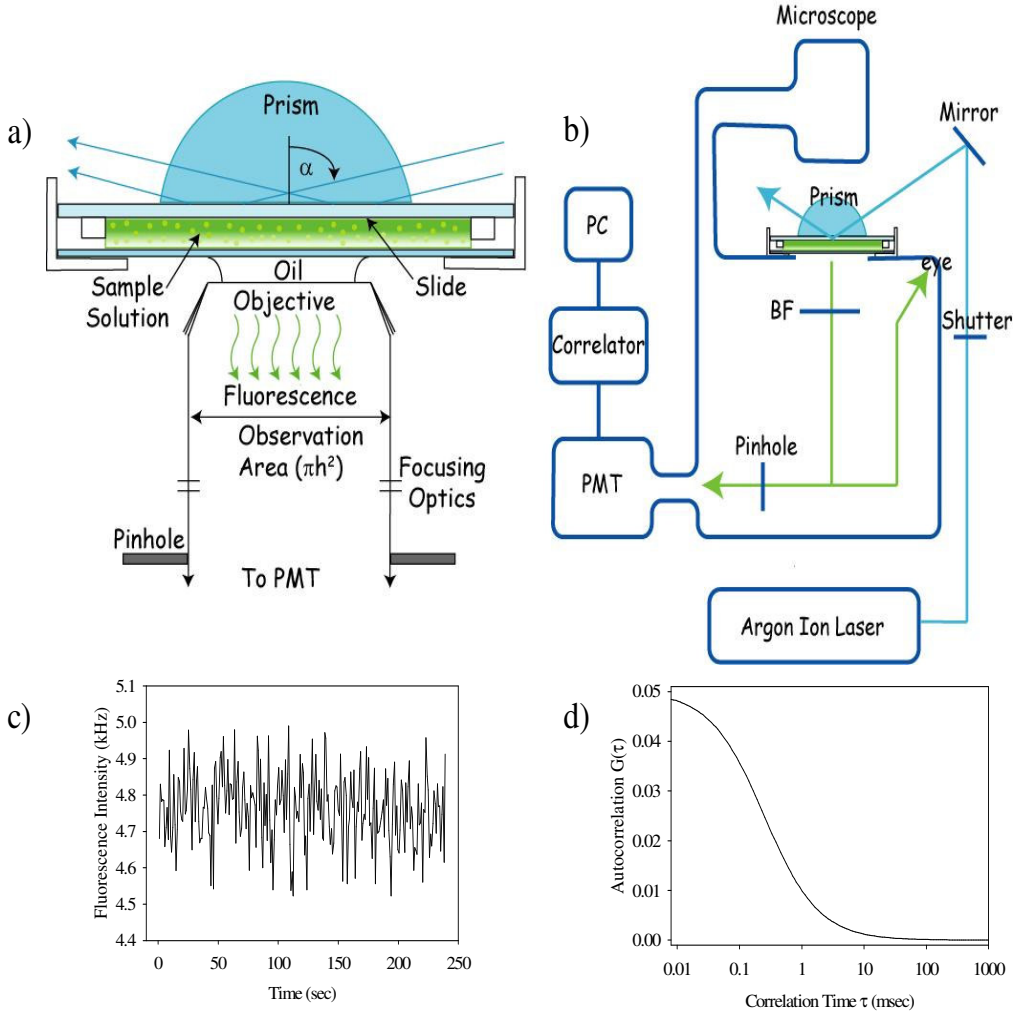

From the advent of TIR-FCS there existed a lag time during which the technique saw little application. However, now TIR-FCS is beginning to see abundant application and it appears that the technique is fast becoming a staple in biophysical research. A recent review of TIR-FCS provides detailed information about its applications (Thompson and Pero, in

press). However, a brief review of the use of TIR-FCS has been included here. Shortly after the first theoretical paper, a second short theory paper was published (Thompson, 1982). This paper hypothesized that TIR-FCS could be used to measure the surface binding kinetics of nonfluorescent ligands competing with fluorescent ligands for the same binding sites. The first experimental example that united the theory and TIR-FCS was when the reversible kinetics of tetramethylrhodamine-labeled immunoglobulin and insulin interacting with fused silica coated with serum albumin was measured (Thompson and Axelrod, 1983).

TIR-FCS was used to measure the diffusion coefficients and concentrations of fluorescently-labeled IgG diffusing within the depth of the evanescent wave (Starr and Thompson, 2001; Starr and Thompson, 2002). Also, TIR-FCS was recently demonstrated to measure the kinetics of a specific and reversible association between fluorescently labeled ligands (IgG) in solution and their receptors (mouse FcγRII) embedded in substrate-supported planar membranes (Lieto *et al.*, 2003; Scwhille, 2003). This application is noteworthy because it was the first demonstration of nonfluorescent and fluorescent ligands (of the same type) being measured by TIR-FCS as proposed by the second theory paper (Thompson, 1982). The next extension of this would be to monitor the binding of ligands of different types (one fluorescently-labeled species and one unlabeled species). Although this has not occurred to date, investigations of this nature are being proposed.

Of late, two studies monitored the diffusion of fluorescein within the evanescent wave depth using TIR-FCS (Harlepp *et al.*, 2004; Hassler *et al.*, 2005). These represent the first studies demonstrating the application of TIR-FCS by through-objective as opposed to through-prism optics (Hassler *et al.*, 2005) and also the use of TIR-FCS to calibrate the depth of the evanescent wave. The application of TIR-FCS to live cell studies still remains limited.

However, TIR-FCS has been used to monitor the motions of fluorescently labeled, intracellular vesicles near the plasma membranes of adherent cells (Johns *et al.*, 2001; Holt *et al.*, 2004).

TIR-FCS is also being extended beyond usage in the area of biophysics. TIR-FCS has been used to monitor the reversible kinetics of rhodamine 6G interacting with C-18-modified silica surfaces (Hansen and Harris, 1998a; Hansen and Harris, 1998b). Subsequently, a comprehensive set of measurements employed TIR-FCS to investigate molecular transport in substrate-supported, sol-gel films (McCain and Harris, 2002; McCain *et al.*, 2004a; McCain *et al.*, 2004b).

Some recent interest in TIR-FCS has been in its use with high refractive index substrates to generate very small evanescent waves. Smaller evanescent waves would be of use because they would facilitate the study of systems with weaker binding constants and provide information about chemistry occurring closer to surfaces (Thompson and Pero, 2005). Recently, it has been proven that phospholipid bilayers can be formed upon titanium dioxide and strontium titanate (Starr and Thompson, 2000; Rossetti *et al.* 2005). Consequently, the first step to amending the use of high refractive index substrates to biophysical surface studies has been taken. Furthermore, combining high refractive index substrates with techniques like variable angle total internal reflection (VA-TIR) will allow depth profiling studies to be performed. VA-TIR changes the incidence angle of the impinging laser light and produces smaller evanescent depths by Eq. 1.2.

This thesis represents the compilation of new methodologies and theories all intrinsically related to model membranes, total internal reflection, and TIR-FCS. Their development should modify existing methodology, facilitate the growth of new experimental

protocols, and lead to the modification of theories governing interactions near membranes. It is hoped that this contribution provides a stepping stone upon which future contributors may lay a firm foot.

Pero, J.K., Haas, E.M., and Thompson, N.L. 2006 *J. Phys. Chem. B.* 110:10910-10918.

Chapter 2 Size Dependence of Protein Diffusion Very Close to Membrane Surfaces: Measurement by Total Internal Reflection with Fluorescence Correlation Spectroscopy

2.1 Abstract

The diffusion coefficients of nine fluorescently labeled antibodies, antibody fragments and antibody complexes have been measured in solution very close to supported planar membranes by using total internal reflection with fluorescence correlation spectroscopy (TIR-FCS). The hydrodynamic radii (3 to 24 nm) of the nine antibody types were determined by comparing literature values with bulk diffusion coefficients measured by spot FCS. The diffusion coefficients very near membranes decreased significantly with molecular size, and the size dependence was greater than that predicted to occur in bulk solution. The observation that membrane surfaces slow the local diffusion coefficient of proteins in a size-dependent manner suggests that the primary effect is hydrodynamic as predicted for simple spheres diffusing close to planar walls. The TIR-FCS data are consistent with predictions derived from hydrodynamic theory. This work illustrates one factor that could contribute to previously observed non-ideal ligand-receptor kinetics at model and natural cell membranes.

2.2 Introduction

The interactions of ligands with their receptors at biological interfaces such as membranes are at the heart of many if not all biological processes including, for example, neurotransmission (Kim and Huganir, 1999), immunological response (Ravetch and Bolland,

2001), and nutrient uptake (Zorzano *et al.*, 2000). Previous studies have indicated that the association/dissociation kinetics of ligands in solution with receptors in natural or model membranes are very often not adequately explained as simple, reversible, bimolecular reactions between point particles (Hsieh and Thompson, 1995; Payne *et al.*, 1997; McKiernan *et al.*, 1987; Anderson and McConnell, 1999; Sahu *et al.*, 2000; Domagala *et al.*, 2000). Numerous hypotheses have been developed to account for the observed non-ideality including models with an increased number of discrete states (Lauffenburger and Lindermann, 1993) or models in which the system is described as containing a continuum of bound states (Kopelman, 1988; Frauenfelder *et al.*, 1991; Murray and Honig, 2002). Other investigations into the molecular details of ligand-receptor kinetics have included rebinding effects (Lagerholm and Thompson, 1998; Levin *et al.*, 2002), rotational mobility or orientational effects (Shoup *et al.*, 1981; Schweitzer-Stenner et. al., 1992). An additional possibility is that the observed non-ideality arises at least in part from deviations of the ligand translational mobility in close proximity to membranes from the bulk diffusion coefficient.

Total internal reflection with fluorescence correlation spectroscopy (TIR-FCS) is a method particularly well-suited to probing molecular motions and interactions close to surfaces. In TIR-FCS, a laser beam is internally reflected at the interface of a planar surface and an aqueous medium. The internal reflection generates a surface-associated evanescent field that penetrates only slightly into the aqueous medium and excites fluorescence from molecules bound to the surface or in solution but very close to the surface. The fluorescence arising from a small surface-adjacent volume, defined by the depth of the evanescent field along with an image-plane aperture, is monitored and fluctuates as molecules move into and

out of the volume. The time-dependence of the autocorrelation function of the fluorescence fluctuations provides information about the local translational mobility of the fluorescent molecules and if they reversibly interact with surface sites, the kinetics associated with the surface interaction.

The theoretical basis for using TIR-FCS to examine near-surface dynamics, including translational diffusion in solution very close to the surface as well as the kinetics of reversible association and dissociation with the surface, has been established (Thompson *et al.*, 1981; Starr and Thompson, 2001; Lieto and Thompson, 2004). A number of experimental TIR-FCS studies have also been carried out. Initially, TIR-FCS was used to examine the reversible kinetics of tetramethylrhodamine-labeled immunoglobulin and insulin interacting with fused silica coated with serum albumin (Thompson and Axelrod, 1983) and of rhodamine 6G interacting with C-18-modified silica surfaces (Hansen and Harris, 1998a; Hansen and Harris, 1998b). Subsequently, a comprehensive set of measurements employed TIR-FCS to investigate molecular transport in substrate-supported, sol-gel films (McCain and Harris, 2002; McCain *et al.*, 2004a; McCain *et al.*, 2004b). Two recent studies monitored the diffusion of fluorescein within the evanescent wave using TIR-FCS (Harlepp *et al.*, 2004; Hassler *et al.*, 2005). The first demonstration of TIR-FCS as a method for monitoring the kinetics of a specific and reversible association between fluorescently labeled ligands (IgG) in solution and their receptors (mouse FcγRII) embedded in substrate-supported planar membranes has been recently described (Lieto *et al.*, 2003). Versions of TIR-FCS have also been used to monitor the motions of fluorescently labeled, intracellular vesicles near the plasma membranes of adherent cells (Johns *et al.*, 2001; Holt *et al.*, 2004).

The work described here addresses the nature of protein diffusion very near model phospholipid membrane surfaces. The question considered is the manner in which the membrane affects local protein diffusion and therefore might affect the kinetics of interaction between protein ligands and their membrane-associated receptors. In a previous work, comprehensive TIR-FCS measurements were carried out for monoclonal mouse IgG diffusing close to substrate-supported planar model membranes (Starr and Thompson, 2002). The main conclusion of this work was that if local electrostatic fields significantly affect protein diffusion close to membrane surfaces, the effects are confined to distances much smaller than 100 nm from the surface. However, this work did suggest that hydrodynamic effects might affect protein mobility close to membrane surfaces in a manner that might be observable even at distances extending 100 nm or more from the membrane.

Indeed, there exists a long-lived literature describing decreased diffusion of spherical particles close to planar walls. The core of these theories is related to the development of the notion of frictional coefficients when addressing macromolecular hydrodynamics. In these continuum-based theoretical treatments, the frictional coefficients for sphere motion through a viscous medium close to and both tangential or normal to the surface are increased, and the diffusion coefficients are decreased. These effects, for spheres diffusing close to walls, have been theoretically predicted for decades and the signature is an increased dependence of the local diffusion coefficient on the size of the sphere (Forster and Lauffenburger, 1994). The theoretical predictions have been experimentally verified, in part, for large colloidal particles (Frej and Prieve, 1993; Bevan and Prieve, 2000; Lin *et al.*, 2000; Dufresne *et al.*, 2000; Pagac *et al.*, 1996; Pralle *et al.*, 1998; Sholl *et al.*, 2000; Oetama and Walz, 2005).

In the work described herein, the diffusion coefficients of nine fluorescently labeled antibody fragments, antibodies and antibody complexes (with hydrodynamic radii ranging from 3 to 24 nm) adjacent to planar supported model membranes were measured by using TIR-FCS. The results show that the local diffusion coefficient decreases with the hydrodynamic radius, over and above that predicted by the Stokes-Einstein equation describing diffusion in bulk solution, and in a manner consistent with theoretical predictions according to hydrodynamic theories describing particle motions next to walls.

2.3 Theoretical Background

2.3.1 Apparatus

A laser beam is internally reflected at a substrate/solution interface and creates an evanescent intensity that penetrates exponentially with characteristic depth d into the solution adjacent to the surface (Thompson and Pero, in press; Abramowitz and Stegun, 1968) (Figure 2.1). The evanescent intensity, *I(z)*, is given by

$$I(z) = I_0 \exp(-\frac{z}{d}) \qquad (2.1)$$

where z is the distance in solution from the interface, d is the depth of the evanescent wave, and I_0 is the intensity at the interface. In the measurements described here, the interface of a fused silica substrate (refractive index $n_1 = 1.467$) and an aqueous salt solution (refractive index $n_2 \approx 1.337$) (Starr and Thompson, 2002) is illuminated by a 488.0 nm laser line. For these refractive indices, the critical angle for internal reflection is $\alpha_C = 65.7^o$. Thus, the incidence angle (α) can in practice range from $\alpha \approx 71°$ to $\alpha \approx 85°$. For these conditions, the

evanescent depth ranges from $d \approx 105$ nm to $d \approx 65$ nm. Fluorescence is collected through a 60x, 1.4 N.A. objective. The evanescent intensity along with a small circular aperture (50 μm radius) placed at an intermediate image plane of a microscope, corresponding to a radius $h \approx 1$ μm in the sample plane, defines a small observation volume.

Figure 2.1 Schematic of TIR-FCS.
A small sample volume is defined by the depth of the evanescent intensity, *d*, in combination with a circular aperture placed at an intermediate image plane of the microscope that defines an area of radius *h* in the sample plane. The fluorescence measured from the small sample volume adjacent to the surface fluctuates with time as molecules diffuse close to the surface, and the fluorescence fluctuations are autocorrelated.

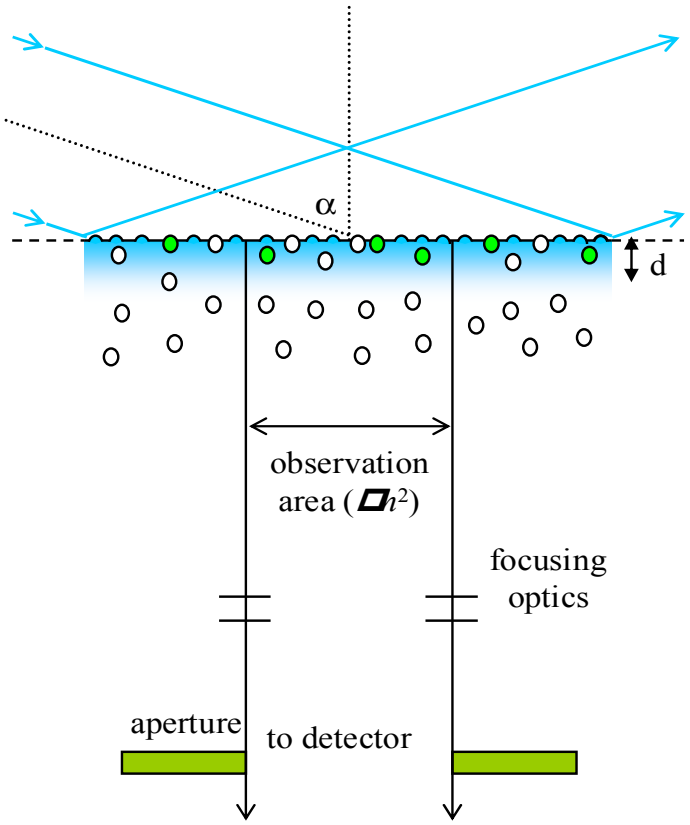

2.3.2 Fluorescence Fluctuation Autocorrelation Function G(τ)

Individual fluorescent molecules in solution diffuse into and out of the defined observation volume. Their motion causes the measured fluorescence to fluctuate with time. These fluctuations are defined as the difference between the instantaneous fluorescence intensity, *F(t)*, and its time-averaged value, <*F*>; i.e., $\delta F(t) = F(t) - \langle F \rangle$. The fluorescence fluctuations are autocorrelated to obtain information about the diffusion of fluorescent molecules in the observation volume. The fluorescence fluctuation autocorrelation function is defined as

$$G(\tau) = \frac{\langle \delta F(t+\tau)\delta F(t) \rangle}{\langle F \rangle^2} = \frac{\langle \delta F(\tau)\delta F(0) \rangle}{\langle F \rangle^2} \tag{2.2}$$

2.3.3 Magnitude of the Fluorescence Fluctuation Autocorrelation Function

As shown previously (Starr and Thompson, 2001), if the concentration of fluorescent molecules in solution does not depend on *z*, as we assume here, the magnitude of the fluorescence fluctuation autocorrelation function ($G_e(0)$) is

$$G_e(0) = \frac{1}{2N_e} \tag{2.3}$$

where N_e is the average number of fluorescent molecules in the observed volume, defined here as

$$N_e = \pi h^2 dA \tag{2.4}$$

$G_e(0)$ is inversely related to the solution concentration A.

2.3.4 Shape of the Fluorescence Fluctuation Autocorrelation Function for Spatially Independent Diffusion.

In this work, we assume that the sample volume radius along the surface, h, is much greater than the evanescent depth, d. When the diffusion coefficient, D, does not depend on z, the theoretical form of the TIR-FCS fluorescence fluctuation autocorrelation function is (Starr and Thompson, 2001)

$$G_e(\tau) = G_e(0)\left\{(1-2R_e\tau)\exp(R_e\tau)erfc[(R_e\tau)^{1/2}] + 2(\frac{R_e\tau}{\pi})^{1/2}\right\} \tag{2.5}$$

where

$$R_e = \frac{D}{d^2} = \frac{\gamma}{d^2 r} \qquad \& \qquad \gamma = \frac{kT}{6\pi\eta} \tag{2.6}$$

Here, R_e is the rate for diffusion in solution through the depth of the evanescent intensity, r is the hydrodynamic radius, k is Boltzmann's constant, T is the absolute temperature, and η is the solution viscosity. As shown in Figure 2.2a, $G_e(\tau)/G_e(0)$ decays monotonically with time. The magnitude of the initial slope is (Abramowitz and Stegun, 1968)

$$S_e = \left| \left\{ \frac{d}{d\tau} \left[\frac{G_e(\tau)}{G_e(0)} \right] \right\}_{\tau=0} \right| = R_e \qquad (2.7)$$

The time at which $G_e(\tau)$ equals one half of its initial value is 3.3 R_e^{-1}.

Figure 2.2 Fluorescence Fluctuation Autocorrelation Function for Spatially Independent Diffusion.

$G(\tau)/G(0)$ decays with time. The blue line shows $G_e(\tau)/G_e(0)$ for evanescent illumination (Eq. 2.5). In this case, the initial slope is $-R_e$ and the half-time for decay is 3.3 R_e^{-1}. The pink line shows $G_s(\tau)/G_s(0)$ for illumination with a focused spot in solution (Eq. 2.12). In this case, the initial slope is $-R_s$ and the half-time for decay is R_s^{-1}.

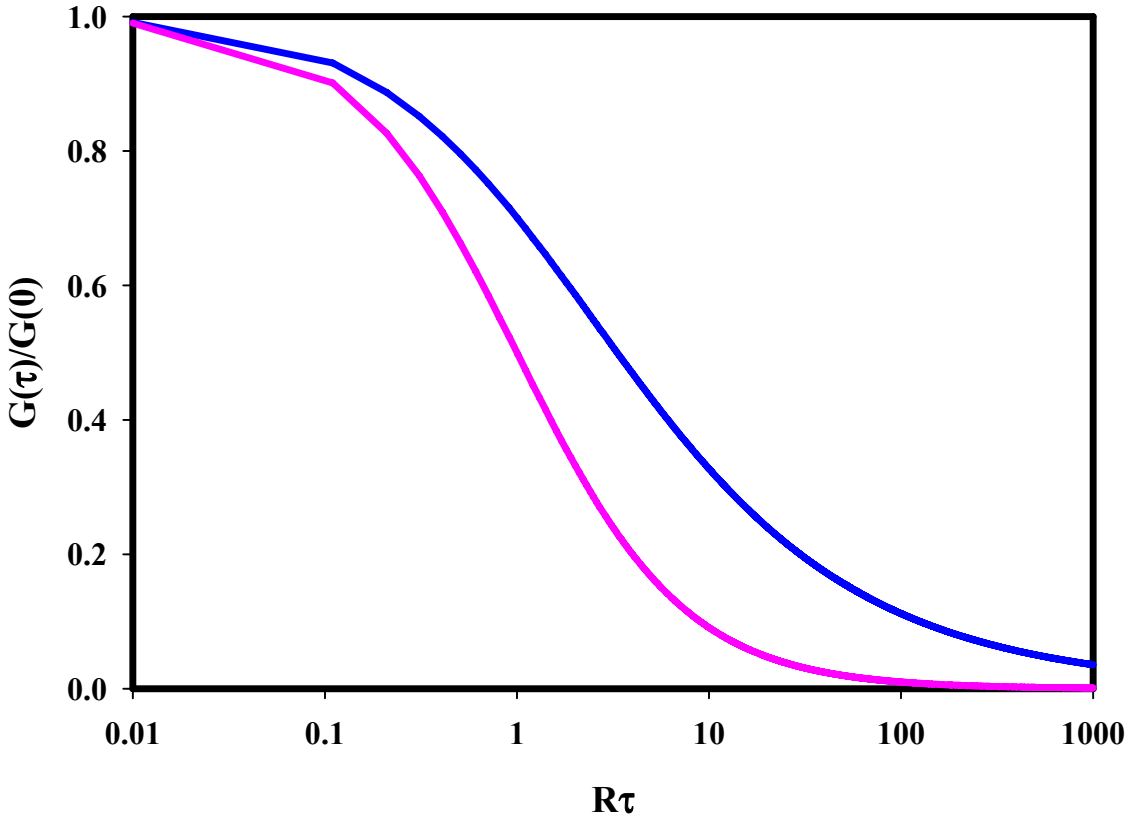

2.3.5 Spatially Dependent Diffusion Coefficients

In this work, we are particularly concerned with the situation in which the diffusion coefficient depends on the distance from the interface. We test the hypothesis that the diffusion coefficient of proteins near membrane surfaces is significantly slowed by

hydrodynamic effects. In this case, even in the absence of local potentials, this coefficient is predicted to depend on z (and the sphere radius, denoted here by r) for a sphere diffusing next to a wall. The predicted form of $D(z, r)$, for diffusional motion normal to the interface, is (Brenner, 1961; Lin *et al.*, 2000; Oetama and Walz, 2005)

$$\frac{D}{D(z,r)} = \frac{4}{3}\sinh[\cosh^{-1}(1+\frac{z}{r})]\sum_{k=1}^{\infty}\frac{k(k+1)}{(2k-1)(2k+3)} \left\{\frac{2\sinh[(2k+1)\cosh^{-1}(1+\frac{z}{r})]+(2k+1)\sinh[2\cosh^{-1}(1+\frac{z}{r})]}{4\sinh^2[(k+0.5)\cosh^{-1}(1+\frac{z}{r})]-(2k+1)^2\sinh^2[\cosh^{-1}(1+\frac{z}{r})]}-1\right\} \quad (2.8)$$

where r is the particle radius, z is the distance between the sphere edge and the wall, and $D(\infty, r) = D$ is the diffusion coefficient in the bulk far from the wall. A much simpler, approximate form for Eq. 2.8 has been reported (Sholl *et al.*, 2000) as

$$\frac{D(z,r)}{D} = \frac{6z^2+2rz}{6z^2+9rz+2r^2} \quad (2.9)$$

Numerical calculations show that Eqs. 2.8 and 2.9 deviate by no more than 0.6%. The function $D(z,r)/D$, which ranges from zero to one as a function of z, is shown in Figure 2.3a.

Figure 2.3 Distance-Dependent Diffusion for a Sphere Near a Wall.
(a) The diffusion coefficient as a function of the sphere radius r and the distance from the wall z increases from zero at the wall to the bulk diffusion coefficient as z approaches infinity. This plot was calculated from Eq. 2.9 and also equals Eq. 2.8. The distance for which $D(z,r) = (1/2)D$ is $z/r = (5+73^{1/2})/12=1.13$. (b) The value of Eq. 2.10 (with Eq. 2.9), calculated numerically, is shown for particle radii ranging from $0 \leq r \leq 30$ nm and for evanescent depths of (black) $d = 65$ nm, (pink) $d = 75$ nm, (green) $d = 85$ nm, (blue) $d = 95$ nm and (red) $d = 105$ nm. The effect on S_e/R_e is more prominent for larger radii and thinner evanescent wave depths.

a)

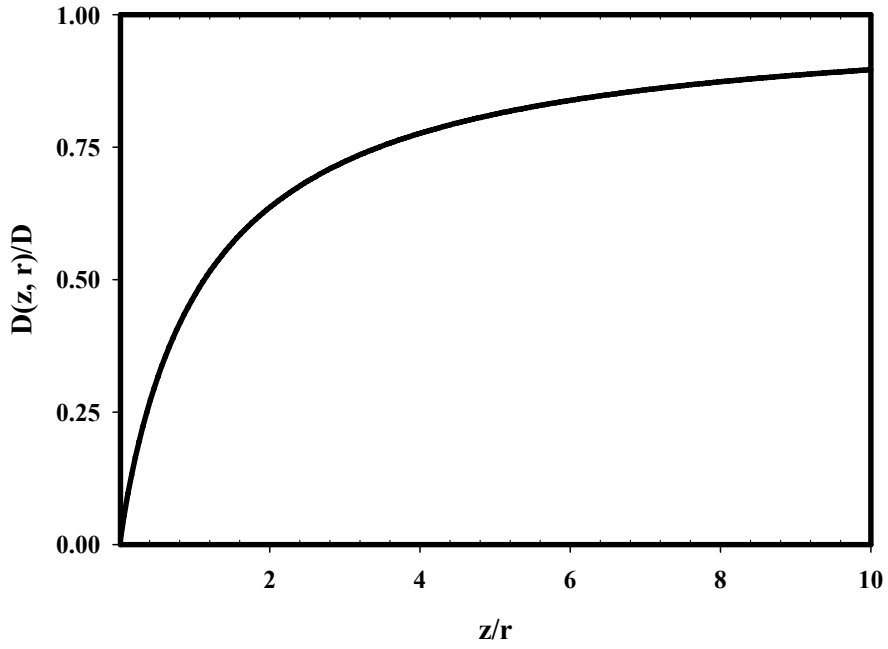

b)

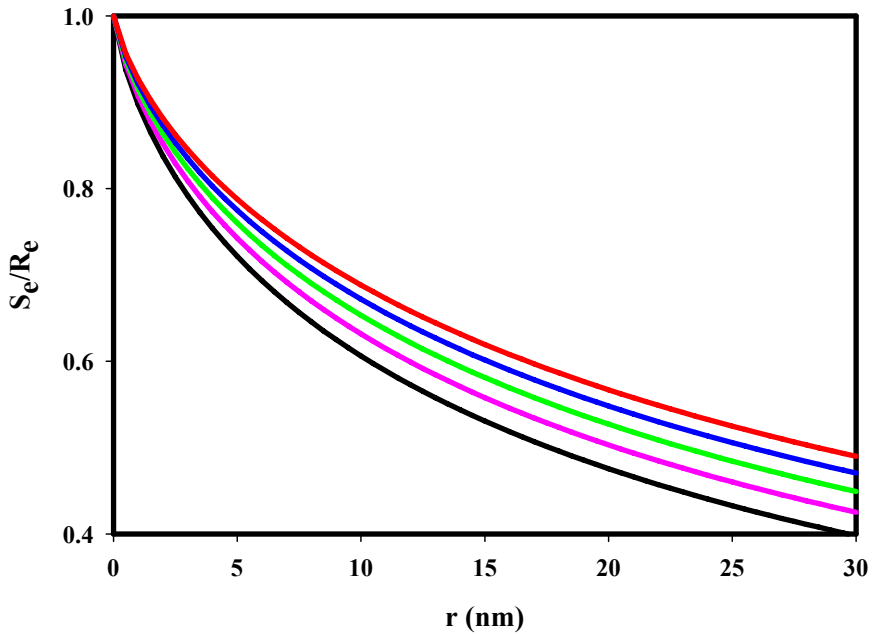

2.3.6 Shape of the Fluorescence Fluctuation Autocorrelation Function for Spatially Dependent Diffusion

The generalization of Eq. 2.5 for the case in which the diffusion coefficient depends on z is not known. However, as shown in the Appendix, if $D(0) = 0$ (see Eq. 2.9), the magnitude of the initial slope of the normalized fluorescence fluctuation autocorrelation function is

$$S_e(r) = R_e \left| \left\{ \frac{\int_0^\infty \exp(-\frac{2z}{d}) \frac{D(z,r)}{D} dz}{\int_0^\infty \exp(-\frac{2z}{d}) dz} \right\} \right| \tag{2.10}$$

where R_e is given by Eq. 2.6. The value of S_e/R_e was calculated numerically from Eqs. 2.9 and 2.10 and is shown in Figure 2.3b. The ratio S_e/R_e decreases for larger particle radii and for thinner evanescent wave depths. Remarkably, S_e is predicted to be measurably less than that for pure bulk diffusion, R_e, even in cases where the particle radius is significantly less than the evanescent wave depth.

2.3.7 Fluorescence Correlation Spectroscopy with a Focused Spot in Solution

In some measurements, the bulk diffusion coefficients of different protein preparations were examined by carrying out fluorescence correlation spectroscopy far from the membrane surface. In these measurements, the sample volume was defined by tightly focusing the laser beam and aligning a confocal pinhole in a back image plane. In this case (Thompson, 1991),

$$G_s(0) = \frac{1}{N_s} \tag{2.11}$$

where N_s is the average number of molecules in the new sample volume. The shape of the fluorescence fluctuation autocorrelation function is approximated as (see Methods)

$$G_s(\tau) \approx \frac{G_s(0)}{1 + R_s \tau} \tag{2.12}$$

where

$$R_s = \frac{4D}{s^2} = \frac{4\gamma}{s^2 r} \tag{2.13}$$

s is the $1/e^2$-radius of the focused spot and γ is defined in Eq. 2.6 (Figure 2.2b). The magnitude of the initial slope is

$$S_s = \left| \left\{ \frac{d}{d\tau} \left[\frac{G_s(\tau)}{G_s(0)} \right] \right\}_{\tau=0} \right| = R_s \tag{2.14}$$

and the half-time for decay is R_s^{-1}.

2.4 Materials and Methods

2.4.1 Antibody Preparation

Antibodies of the type IgM (Sigma-Aldrich, St. Louis, MO), IgA (Sigma-Aldrich), IgG F(ab')$_2$ (Jackson ImmunoResearch Laboratories, Inc., West Grove, PA), and IgG Fab (Jackson ImmunoResearch Laboratories) were dialyzed into phosphate-buffered saline (PBS; 0.05 M sodium phosphate, 0.15 M NaCl, pH 7.4). IgG antibodies were obtained from the anti-dinitrophenyl mouse-mouse hybridoma 1B711 (American Type Culture Collection, Rockville, MD), the anti-rat IgG mouse-mouse hybridoma MAR18.5 (American Type Culture Collection), and the anti-Thy-1 rat-mouse hybridoma 31-11 (Gerald J. Spangrude, University of Utah, Salt Lake City). Hybridomas were maintained in culture and the secreted antibodies were purified from cell supernatants by affinity chromatography with DNP-conjugated human serum albumin for 1B711 antibodies (Starr and Thompson, 2002), with Protein G for MAR18.5 antibodies, and with MAR18.5 for 31-11 antibodies (Poglitsch and Thompson, 1990). For MAR18.5 purification, the wash buffer was PBS and the elution buffer was 0.1 M glycine, 0.01% NaN_3, pH 2.7. Each liter of supernatant yielded approximately 10-15 mg of antibody as determined spectrophotometrically by assuming that the molar absorptivity at 280 nm was 1.4 mL mg^{-1} cm^{-1}. All antibodies were subjected to SDS-PAGE with silver staining and FPLC-dynamic light scattering to ascertain their purity.

Covalently conjugated antibody complexes (AbC's) were engineered to make molecules of differing radii than those found naturally and provide a broader range of molecular sizes to study. 31-11 antibodies were mixed with MAR18.5 antibodies at a 2:1 ratio as a MAR18.5 antibody can in principle bind two 31-11 antibodies on their light chains. After mixing the antibodies the final antibody concentration ranged between 3-10 mg/mL in

PBS. Bis(sulfosuccinimidyl) suberate (BS^3) (Pierce Biotechology, Rockford, IL) was then added to the antibodies in a 20-120 molar excess to bind the antibodies together and prevent equilibrium dissociation. The reaction with BS^3 was carried out for 30 minutes and then quenched with 25-45 mM glycine, at room temperature. The mixture was then dialyzed against PBS at 4^{o}C to remove excess glycine and BS^3.

The mixture of antibody complexes was then subjected to SDS-PAGE analysis with silver staining to determine the number of products formed. The gels indicated that a broad range of products had been created. This mixture of AbC's was dialyzed into PBS with 0.5 M NaCl and passed through a 0.2 μm filter. The AbC's were separated using an ÄKTA FPLC interfaced with a Tricorn Superose 6 column (Amersham Biosciences, Piscataway, NJ). The FPLC was operated at a flow rate between 0.4-0.5 mL/min and 0.5 mL fractions were collected. Analysis of the chromatographic trace revealed that the separation was incomplete and produced one broad peak. Numerous separations were performed under the same conditions and the eluents were pooled fraction by fraction. The broad peak was divided into five groups. The first of the five groups was discarded as it contained extremely large AbC's. The remaining four groups were dialyzed into PBS and named AbC1, AbC2, AbC3, and AbC4 with AbC1 being the largest and first to elute and AbC4 being the smallest and last to elute.

All antibodies and AbC's were fluorescently labeled using the AlexaFluor488 Protein Labeling Kit (Molecular Probes, Inc., Eugene OR). The free dye was removed by using size exclusion chromatography with Sephadex G-25 or G-50 in PBS. The molar concentrations of antibody or AbC and the molar ratios of AlexaFluor488 to antibody or AbC (0.5-9 dyes/protein) were determined spectrophotometrically according to the manufacturer's

protocol. The molar extinction coefficients (in $M^{-1}cm^{-1}$) for the antibodies and antibody complexes were approximated by multiplying 1.4 L/cm g by the estimated molecular weights. The estimated molecular weights for the AbCs were determined by using a Wyatt DAWN EOS light scattering instrument interfaced to an Amersham Biosciences ÄKTA. As described above, the FPLC separation was incomplete. Consequently, the peak was split into five segments, the first segment was excluded, and the light scattering software was used to determine an average molecular weight for the remaining four segments. Immediately before use, Fab, $F(ab')_2$, IgG, and AbC4 were clarified using 0.1 μm and then 0.02 μm filters; IgM, IgA, AbC1, AbC2, and AbC3 were clarified using 0.2 μm filters.

2.4.2 Phospholipid Vesicles

Small unilamellar vesicles of 1-palmitoyl-2-oleoyl-glycero-3-phosphocholine (POPC) (Avanti Polar Lipids, Birmingham, AL) were prepared by tip sonication of 2 mM suspensions of POPC in water as previously described (Lagerholm *et al.*, 2000). In some experiments, 2 mol% of the fluorescent lipid 1-acyl-2-[12-(7-nitro-2-1,3-benzoxadiazol-4-yl) aminododecanoyl]-glycero-3-phophocholine (NBD-PC) was included to monitor bilayer formation and quality (see below). Vesicle suspensions were clarified by air ultracentrifugation (130000*g*, 30 min) immediately before use.

2.4.3 Substrate-Supported Phospholipid Bilayers

Substrate-supported planar phospholipid bilayers were formed as previously described (Starr and Thompson, 1993). Fused silica substrates were cleaned extensively by boiling in detergent (ICN, Aurora, OH), bath sonicating, rinsing thoroughly with deionized water, and drying at 160 ˚C. Substrates were cleaned in an argon ion plasma cleaner (15 minutes, 25 °C) (PDC-3XG, Harrick Scientific, Ossining, NY). Planar bilayers were formed

by applying 75 μL of the vesicle suspension to a fused silica substrate (1 h, 25 °C), and rinsing with 3 mL of PBS. Fluorescence imaging microscopy and fluorescence pattern photobleaching recovery indicated that bilayers containing NBD-PC were continuous and fluid. For TIR-FCS measurements, bilayers without NBC-PC were treated with 400 μL of 15-90 nM antibody or AbC in PBS. For FCS experiments with a focused spot, bilayers without NBC-PC were treated with a mixture of 3 nM antibody or AbC and 27 nM unlabelled antibody or AbC.

2.4.4 Fluorescence Microscopy

TIR-FCS and FCS with a focused spot were carried out on an instrument consisting of an argon ion laser (Innova 90-3; Coherent, Palo Alto, CA), an inverted microscope (Zeiss Axiovert 35), and a single-photon counting photomultiplier (RCA C31034A, Lancaster, PA). All experiments were conducted at 25 °C using the 488 nm laser line. For TIR-FCS measurements, the laser beam was s-polarized while incident on the fused silica/aqueous interface and generated an evanescent field polarized parallel to the interface. The incidence angle was ≈ 71-85°, corresponding to theoretically predicted evanescent wave depths ranging from 105-65 nm (see above). For conventional FCS measurements, the laser beam was focused in the protein solution approximately 20 μm from the bilayer surface to form a small Gaussian-shaped illumination with a radius on the order of s ≈ 1 μm.

In both TIR-FCS and focused beam experiments, a pinhole with a radius of 50 μm placed at an internal image plane defined an area with a radius of h ≈ 1 μm when projected onto the sample plane. The fluorescence arising from the volume defined by the excitation light and the pinhole was collected through a 60x, 1.4 N.A. objective. The fluorescence signal was autocorrelated by a PC-based correlator board (model 5000/E, ALV).

Autocorrelation functions were obtained within 5-10 min using incident laser intensities of 4-17 μW/μm^2 for TIR-FCS experiments or 5-30 μW/μm^2 for FCS experiments using the focused beam. The resulting evanescent intensities at the interface differed by a factor of ≈ 0.2-2.5. (Thompson *et al.*, 2005) Average blank signals were measured from samples containing buffer adjacent to supported bilayers. Possible detector afterpulsing was examined by using a published procedure (Hillesheim and Muller, 2005). The measurements demonstrated that any afterpulsing present was extremely minimal and in any case much faster that the time range of the TIR-FCS data (see Figure 2.4).

2.4.5 Data Analysis

Autocorrelation functions were background-corrected by multiplying by the factor $\langle S\rangle^2/\langle F\rangle^2$, where $\langle F\rangle = \langle S\rangle - \langle B\rangle$ was the average fluorescence calculated by subtracting the average measured blank signal $\langle B\rangle$ from the average measured total signal $\langle S\rangle$ (Thompson, 1991). TIR-FCS autocorrelation functions were fit to Eq. 2.5 with Eq. 2.3 plus an arbitrary constant G_∞, and the free parameters were R_e, N_e, and G_∞. Autocorrelation functions measured using the focused beam were fit to Eq. 2.12 with Eq. 2.11 plus an arbitrary constant G_∞, and the free parameters were R_s, N_s, and G_∞. For spot FCS measurements, the more general expression, $G_s(\tau) \approx G_s(0)[1+R_s\tau]^{-1}[1+(R_s\tau/\sigma^2)]^{-1/2}$, where σ is the "structure parameter", may also be used for data analysis. However, the value of σ in our apparatus is approximately three, and the second factor in the more general expression is negligible (Allen and Thompson, 2006).

Figure 2.4 Representative TIR-FCS Autocorrelation Functions.
The background-corrected $G_e(\tau)$ are for (a) AbC1 or (b) AbC4 in PBS adjacent to a POPC membrane. The fluorescence was monitored and autocorrelated for 300 s. The average signals $\langle S \rangle$ and background intensities $\langle B \rangle$ were (a) 10.61 & 0.04 kHz and (b) 10.03 & 0.19 kHz. The best fits of these particular functions to Eq. 2.5 with Eq. 2.3 gave (a) $N_e = 2.55$, $R_e = 0.826$ ms^{-1}; and (b) $N_e = 4.81$, $R_e = 4.51$ ms^{-1}. Note that the theoretical curves accurately find the initial slope (insets).

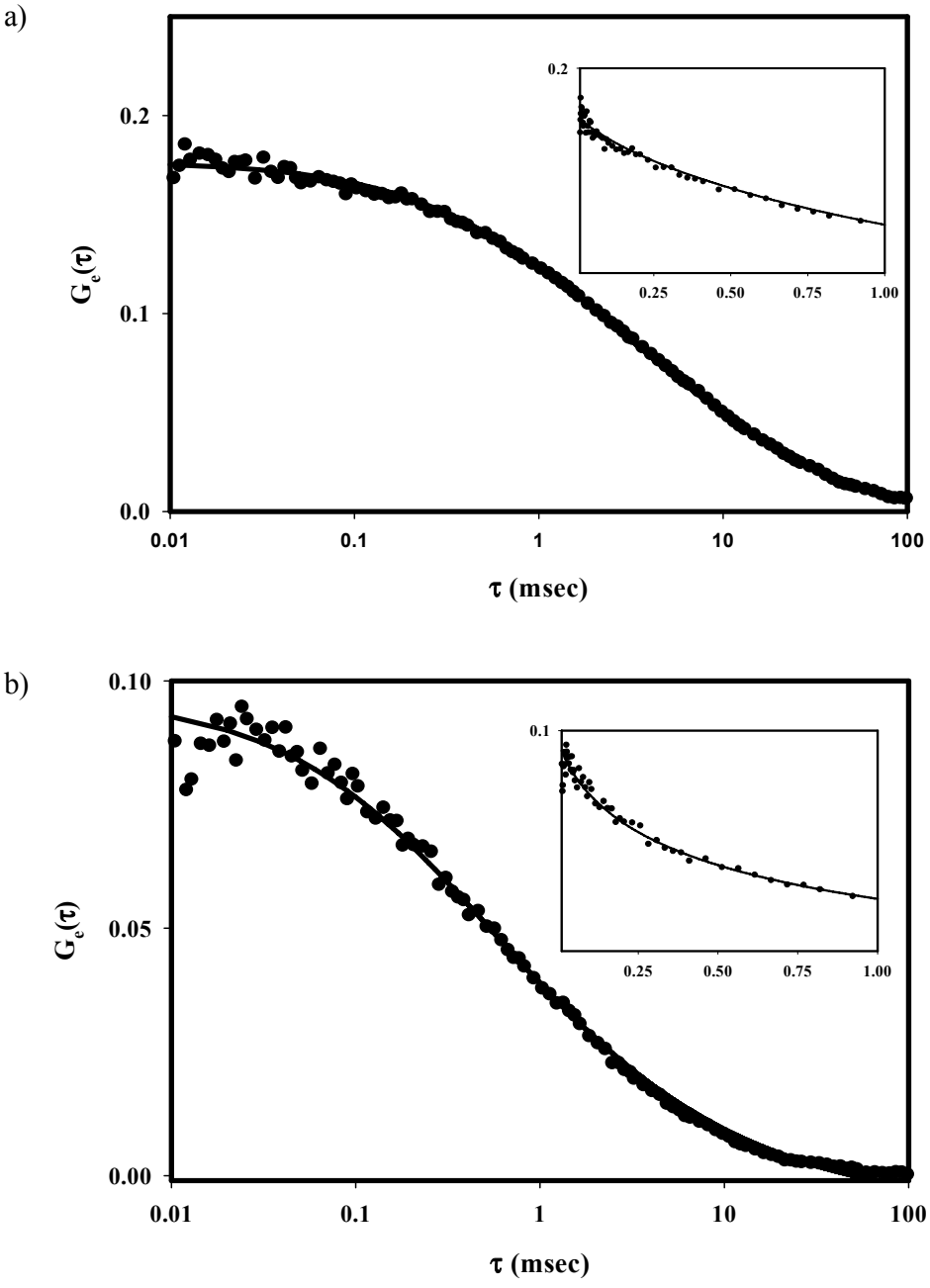

2.5 Results

As viewed through a 1.4 N.A. objective using evanescent illumination, samples consisting of soluble antibodies or AbC's near planar model POPC membranes displayed visually apparent fluorescence fluctuations which appeared as fluorescent twinkles against a uniform background. The temporal fluctuations in fluorescence, as measured through a small pinhole at a back image plane (Figure 2.1), were autocorrelated (Eq. 2.2). These TIR-FCS measurements were carried out for nine antibodies or AbC's. Correlation functions for matched samples not containing fluorescent solutes were not measurable.

Background-corrected TIR-FCS autocorrelation functions, $G_e(\tau)$, were fit to Eq. 2.5 (with Eq. 2.3) plus an arbitrary constant G_∞, with free parameters N_e, R_e, and G_∞. Typical experimentally obtained $G_e(\tau)$ and their best fits to this theoretical form, for two of the nine samples, are shown in Figure 2.4. The best-fit values of the arbitrary offset, G_∞, were on the average less than ~10% in magnitude compared to the best-fit values of $G_e(0)$. The best-fit values of N_e ranged from ~2 to 20, consistent with the expected values of N_e for solution concentrations A = 15-90 nM, an evanescent wave depth d = 85 nm (see below) and an observation area radius h = 1.0 μm (Eq. 2.4). The best fit-values of R_e ranged from 7.8 ms^{-1} to 0.8 ms^{-1} and decreased systematically with molecular size, consistent with expectations. To ensure that the TIR-FCS data did not show photoartifacts, the incident intensity was kept between 4 and 17 $\mu W/\mu m^2$ (Starr and Thompson, 2002) and $G_e(\tau)$ were measured for at least two different incident intensities. No significant change in the best-fit parameters was observed for the two different intensities.

In principle, Eq. 2.5 does not describe the precise shape of the autocorrelation function when the diffusion coefficient depends on the distance from the surface (see above).

The form of this function is unknown, but the magnitude of its initial slope S_e is predicted by Eq. 2.10 (see Appendix). Thus, it is important to note that the best-fits of the experimental autocorrelation functions to Eq. 2.5 accurately find the initial slope (Figure 2.4), upon which further analysis is based. Both the magnitude of the initial slope S_e and the characteristic time for decay of Eq. 2.5 are equal to R_e (Eqs. 2.6 and 2.7).

Conventional FCS measurements with a focused spot were carried out in solutions adjacent but not close to planar membranes, on each of the nine sample types, to determine the hydrodynamic radii of the AbC molecules and the IgA molecule. These autocorrelation functions were background-corrected and the resulting functions $G_s(\tau)$ were fit to Eq. 2.12 (with Eq. 2.11) plus an arbitrary constant G_∞, with free parameters N_s, R_s and G_∞. Hydrodynamic radii for IgG Fab, IgG $(Fab')_2$, IgG and IgM were taken from the literature (Armstrong *et al.*, 2004). The literature value for the IgA radius was not included because it was for monomeric IgA and dynamic light scattering measurements (see Methods) indicated that the IgA used here was dimeric and trimeric in form. At room temperature in aqueous solution, $\gamma \approx 218$ μm^2-nm-s^{-1} (Eq. 2.6). Linear regression of the measured values of R_s as a function of the inverse of the four literature values of r (Eq. 2.13) implied $4\gamma s^{-2} = 793.9$ nm s^{-1}, consistent with a (reasonable) s value of ≈ 1 μm. The constant $4\gamma s^{-2}$ was then used with the other measured values of R_s and Eq. 2.13 to determine the radii of the AbC's and IgA (Table 1).

Table 2.1 Hydrodynamic Radii.

Protein	Hydrodynamic Radius (nm)
IgG Fab	2.91[a]
IgG $(Fab')_2$	4.48[a]
IgG	5.29[a]
IgA	6.92[b]
IgM	12.65[a]
AbC4	4.73[b]
AbC3	6.60[b]
AbC2	12.98[b]
AbC1	23.73[b]

Diffusion rates in bulk solution, R_s, were determined for all nine molecule types by using conventional FCS with a spot focused far from the membrane surface. [a]IgG Fab, IgG $(Fab')_2$, IgG, and IgM radii are from the literature (Armstrong *et al.*, 2004). The average measured values of R_s for these four molecules were plotted against the reciprocal of their radii and used to find a best- fit value for the constant $4\gamma s^{-2}$ (Eqs. 2.6 and 2.13). [b]The best-fit value of this constant was used with Eq. 2.13 to determine the radii r for the remaining five molecules, IgA and AbC1-4.

For the three molecules with the smallest literature-derived molecular radii (Fab, $(Fab')_2$ and IgG) there should be only small surface effects and their bulk diffusion coefficients can be estimated by using the measured values of R_e and $D = R_e d^2$ (Eq. 2.6). For evanescent wave depths ranging from 80 to 90 nm, these calculations implied D values of 50-63 $\mu m^2 s^{-1}$, 36-45 $\mu m^2 s^{-1}$, and 29-37 $\mu m^2 s^{-1}$, respectively. These values are in good agreement with expectations (i.e., slightly lower than) the values predicted by $D = \gamma r^{-1}$ (Eq. 2.6) and the hydrodynamic radii given in Table 1, which are 75 $\mu m^2 s^{-1}$, 49 $\mu m^2 s^{-1}$, and 41 $\mu m^2 s^{-1}$.

The average best-fit values of R_e(= S_e) for each of the nine sample types are shown as a function of the hydrodynamic radius in Figure 2.5a. As expected, S_e decreased significantly with increasing molecular size. In addition, the S_e values agreed very well with the values predicted by Eqs. 2.6, 2.9 and 2.10. These predicted values are also shown in

Figure 2.5a, for $\gamma = 2.18 \times 10^5$ nm^3-ms^{-1} and evanescent wave depths of d = 75, 85, and 95 nm.

Although there is good agreement between the measured and predicted values of S_e, a decrease in the bulk diffusion coefficient is predicted with molecular size, even in the absence of surface effects, by the Stokes-Einstein Equation (Eq. 2.6). A more stringent test for the presence of surface effects is to remove the influence of the Stokes-Einstein Equation and question if the values of S_e still decrease with molecular radius; i.e., to question if the product rS_e decreases with r. In the absence of surface effects, $S_e = \gamma(rd^2)^{-1}$ is predicted to be inversely proportional to r and $rS_e = \gamma d^{-2}$ to be independent of r. Figure 2.5b shows the measured values of the product rS_e as a function of r. Although the values of the standard deviations of these products relative to the average product magnitudes are ~15%, the average product values themselves do not strictly monotonically decay, although, overall, rS_e appears to decrease with r. (A possible source of noise in the relative average values of the products was day-to-day variability in the incidence angle and therefore evanescent wave depth).

Figure 2.5 S_e and rS_e as a Function of r.
(a) The measured values of S_e decrease significantly with the hydrodynamic radius r. (b) The measured values of rS_e also decrease with r. In both (a) and (b), each experimental point shows the average and standard deviation found from approximately 35 independently measured autocorrelation functions. These values are compared with theoretical predictions (Eqs. 2.6, 2.9 and 2.10 with $\gamma = 2.18 \times 10^5$ nm^3-ms^{-1}) for evanescent wave depths d equal to (blue) 75 nm, (pink) 80 nm, (green) 85 nm, (light blue) 90 nm, and (red) 95 nm.

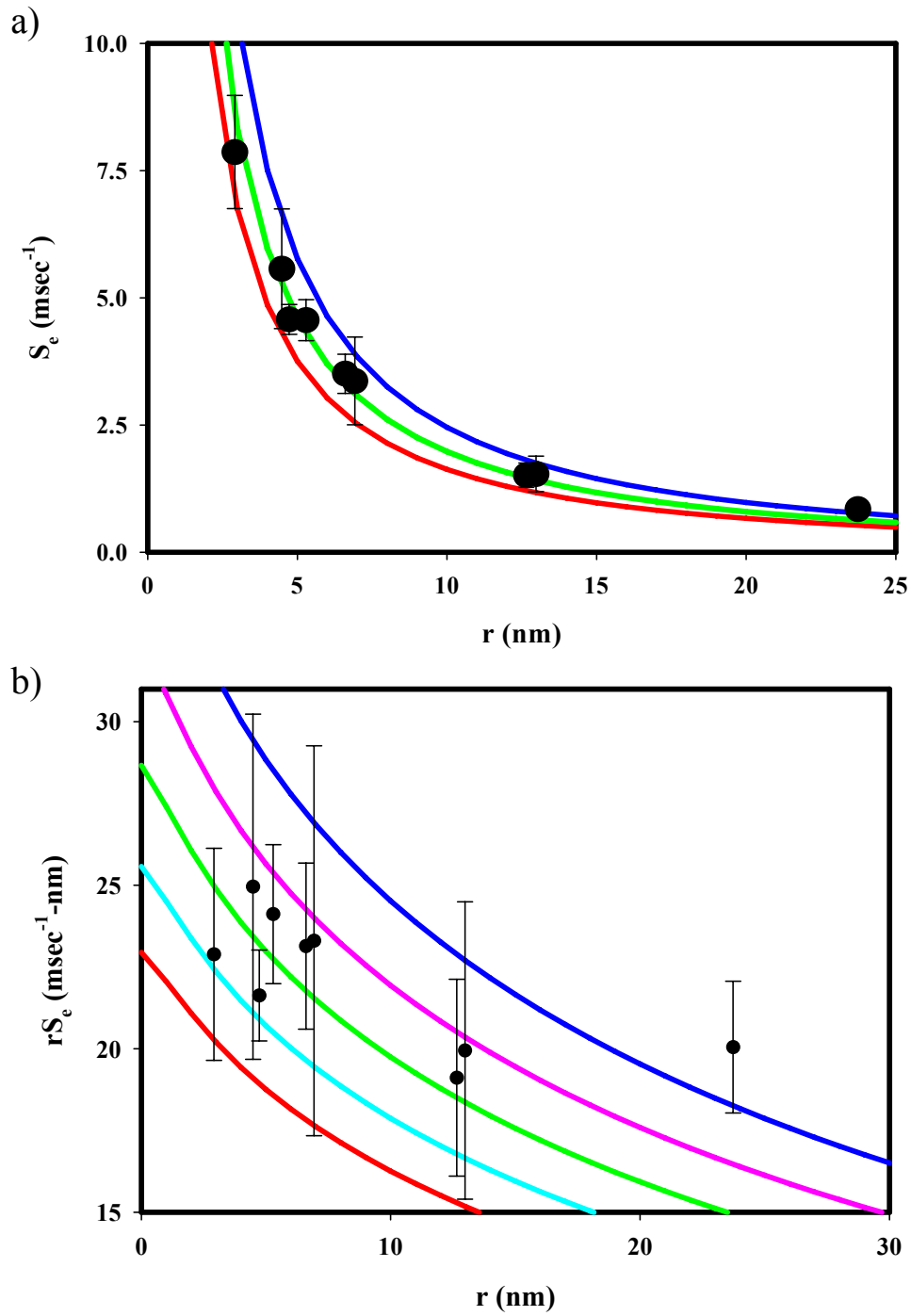

To determine statistically whether or not rS_e in fact decreased with r, linear regression analyses with four data sets were carried out: (1) the nine average values of rS_e vs. r shown in Figure 2.5b; (2) the first eight average values of rS_e vs. r shown in Figure 2.5b (because the last point, for AbC1, seemed not to be as low as one might predict); (3) the 312 individual values of rS_e used to construct the nine average values of rS_e shown in Figure 2.5b; and (4) the 290 individual values of rS_e used to construct the first eight average values of rS_e shown in Figure 2.5b. The results of these analyses are as follows, where α denotes the intercept, β denotes the slope, and R denotes the correlation coefficient: (1) $\alpha = 24.1$ nm-ms^{-1}, $\beta = -0.225$ ms^{-1}, $R = 0.725$; (2) $\alpha = 25.5$ nm-ms^{-1}, $\beta = -0.437$ ms^{-1}, $R = 0.814$; (3) $\alpha = 24.2$ nm-ms^{-1}, $\beta = -0.255$ ms^{-1}, $R = 0.364$; and (4) $\alpha = 25.3$ nm-ms^{-1}, $\beta = -0.425$ ms^{-1}, $R = 0.401$.

The most important question is whether or not the correlation coefficients R indicate a statistically significant decrease in the product rS_e with r. The probabilities p_1 that the correlation coefficients would be of their magnitude or greater, in the absence of a correlation between rS_e and r and given the number of data points included in the various sets, are as follows (Taylor, 1997): (1) $p_1 = 0.027$; (2) $p_1 = 0.014$; (3) $p_1 << 0.0001$; (4) $p_1 <<<0.0001$. The first two values of p_1 imply that the product rS_e most likely decreases with r. However, these cases are more stringent tests in that all of the data points are not included in the analysis. The last two values of p_1, which are found from the more accurate analysis, imply that the product rS_e almost certainly decreases with r. This result is the main conclusion of the work presented here: After accounting for the decrease in the diffusion coefficient in bulk as a function of molecular size, there remains a statistically significant decrease in the diffusion coefficient of proteins close to membrane surfaces that increases in strength with

molecular size. The most likely explanation for this result is that it is a consequence of the predicted decrease in diffusion of particles close to walls due to hydrodynamic effects.

To evaluate the magnitudes of the intercepts α and slopes β, the theoretically predicted values of rS_e were calculated from Eqs. 2.6, 2.9 and 2.10 for the nine hydrodynamic radii shown in Table 1. These values were subjected to linear regression for six cases. The value of γ was assumed to be 2.18 x 10^5 nm^3-ms^{-1} (see above) and the evanescent wave depth d was assumed to equal 80, 85 or 90 nm. The first set of three fits were carried out for all nine r values and for the three assumed evanescent wave depths. These calculations implied intercepts α ranging from 23 to 28 nm-ms^{-1} and slopes β ranging from -0.41 to -0.54 ms^{-1}. The second set of three fits were carried out for the first eight points and for evanescent wave depths equal to 80, 85 or 90 nm. These calculations implied intercepts α ranging from 23 to 29 nm-ms^{-1} and slopes β ranging from -0.54 to -0.71 ms^{-1}. Thus, the measured values of the intercept, α = 24-25 nm-ms^{-1} (see above) agree extremely well with the predicted values. However, the measured values of the slope β do not have quite as good agreement with the theoretically predicted values. For the data sets containing all nine points, the theoretically predicted values (-0.41 to -0.54 ms^{-1}) are higher in magnitude than the experimental values (-0.23 to -0.26 ms^{-1}) by factors ranging from 1.6 to 2.3. For data sets containing only the first eight points, the theoretically predicted values (-0.54 to -0.71 ms^{-1}) are higher than the experimental values (-0.43 to -0.44 ms^{-1}) by factors ranging from 1.2 to 1.6. This result suggests that other factors may have contributed to the observed decrease in rS_e; however, agreement is still very good given the noise in the data.

Figure 2.5b shows the measured values of rS_e as a function of r, along with the theoretically predicted values numerically calculated from Eqs. 2.6, 2.9 and 2.10 with γ =

2.18 x 10^5 nm^3-ms^{-1}. Given the statistical significance of the main conclusion, that the product rS_e decreases with r, the agreement between the measured values of rS_e and the theoretically predicted values, with no adjustable parameters, is remarkable. As a final statistical test, weighted, reduced χ^2 values for comparing the measured and predicted values of rS_e were calculated as a function of the evanescent wave depth (d = 75, 70, 85, 90 and 95 nm) and by including all nine or the first eight points. In the both cases, χ^2 was minimized at d = 85 nm. For all nine points, the minimum value of χ^2 was 1.02 and for the first eight points, the minimum value of χ^2 was 0.34. The probabilities p_2 of finding χ^2 values equal to or larger than the determined ones, given that the data are well described by the theory, were calculated to equal 0.42 and 0.95, respectively. These values of p_2 are well above the conventional value ($\leq$ 0.05) for which it is concluded that significant disagreement exists between data and theoretical predictions (Taylor, 1997). Therefore, the statistical analysis confirms the visual impression that the data in Figure 2.5b agree well with the theoretical predictions.

2.6 Discussion

Although the parameters governing protein diffusion in homogeneous, aqueous solution are well characterized (Russell *et al.* 1989; Weissman *et al.*, 1979; Gaigalas *et al.*, 1992; Kuehner *et al.*, 1997; Le Bon *et al.*, 1999; Beretta *et al.*, 2000; Bowen *et al.*, 2000; Grigsby *et al.*, 2000), very little is known about the manner in which cell membrane surfaces affect the diffusion of nearby proteins causing putative deviations from what one would expect in bulk solution. This question is of biological significance at least in part because of the role that diffusion can play in the kinetics of protein-protein interactions. If membrane surfaces significantly change the local diffusion properties of protein ligands, the effects

could govern the kinetics of ligand-receptor interactions and therefore associated cellular responses.

In a previous study, it was shown that TIR-FCS can be used to characterize protein diffusion very close to substrate-supported planar membranes (Starr and Thompson, 2002). In this work, TIR-FCS measurements were carried out for a model protein, monoclonal mouse IgG; for a variety of electrostatic conditions including membranes that were positively charged, negatively charged or zwitterionic; for different solution pH values spanning the isoelectric point of the IgG; and for solutions with different ionic strengths. No statistically significant change in the local diffusion coefficient was observed for differently charged membranes or IgG molecules; however, the IgG diffusion did decrease somewhat with increasing ionic strength, suggesting that salt-induced changes in the IgG molecules might be changing the local diffusion coefficient indirectly through hydrodynamic effects.

In the work described here, the hypothesis that protein ligands close to membrane surfaces experience hydrodynamic reductions in diffusion was tested according to the primary signature of this predicted effect, that planar surfaces restrict the local diffusion of spherical particles in a manner that depends on the particle size. To do so, nine different proteins with similar chemical characteristics (i.e., all derived from antibodies) but different sizes were assembled (Table 1). As shown in Figure 2.5a, the local diffusion rate as measured by TIR-FCS decreased significantly with the molecular radius, as expected. As shown in Figure 2.5b, even after accounting for the decrease in the diffusion coefficient with molecular radius that would be expected in bulk solution, the local diffusion coefficient still decreased with molecular size, consistent with the hydrodynamic hypothesis. Remarkably, (1) the data are entirely consistent with predictions for the manner in which a planar surface

affects the local mobility of a spherical particle (Brenner, 1961; Lin *et al.*, 2000; Sholl *et al.*, 2000; Oetama and Walz, 2005.) (Eqs. 2.8 and 2.9), with no adjustable parameters included in the comparison of theory and data; and (2) the effects are long-range in that they are observable even at an evanescent wave depth of $d \approx 85$ nm. We therefore tentatively conclude that future reaction-diffusion models for cell-surface ligand-receptor interactions should account for these hydrodynamic effects on local ligand diffusion.

In future studies measurements carried out as a function of the incidence angle and therefore the evanescent wave depth could provide additional confirmation of the observed effect. Opportunities also exist for using substrates with very high refractive indices (e.g., single crystal TiO_2 or $SrTiO_3$) to create extremely thin evanescent waves (as low as 18 nm) (Starr and Thompson, 2000). Eq. 2.7 predicts that, in the absence of hydrodynamic effects, no reduction in the product rS_e will be observed. Much different results are expected in the presence of hydrodynamic effects and the results are predicted to be more prominent for thinner evanescent waves (Eq. 2.10). Other possibly useful approaches include the use photon counting histograms (Kask and Palo, 2001) or high-order autocorrelation (Thompson and Mitchell, 2001).

It will also be important to carry out these measurements near natural cell membranes. For adherent, thick cells, TIR-FCS can in principle monitor the diffusion of cytoplasmic molecules close to the inner membrane leaflet (Mashanov, *et al.*, 2004; Ueda *et al.*, 2001). This method is also likely to be adaptable to external ligands interacting with very thin extended regions of adherent cells where the double-membrane and cellular interior are thin enough so that the evanescent wave extends through the entire cell to the outer leaflet of the apical cell membrane.

Chapter 3 Stacked Phospholipid Bilayers on Planar Supports

3.1 Abstract

A stacked bilayer system has been created utilizing the interactions of biotin and NeutrAvidin. This stacked system contains a primary bilayer of biotinylated lipids, followed by a layer of NeutrAvidin, and finally a secondary bilayer of biotinylated lipids. The stacked bilayer system and various control systems were characterized using FPPR, order parameter measurements, intensity measurements by epi-illumination, and atomic force microscopy. Results from these experiments indicate that the system is semi-continuous. It appears to have "holes" and the second bilayer is often "dimmer" in fluorescence microscopy. It appears that 20% lipid transfer occurs for some control samples where the secondary bilayer transfers lipids to the primary bilayer. Further studies are required to see if transmembrane proteins can be successfully inserted into this system. Overall, this system is continuous and quite possibly has broad application in fields utilizing multilayers, planar membranes as models for biological membranes, and biomolecular devices.

3.2 Introduction

The use of planar supported lipid layers has seen vast application and widespread use since their inception (Brian and McConnell, 1984) in a large number of applications. The widest application for lipid layers has been as simplified models of biological membranes (Wagner and Tamm, 2000; Kühner *et al.*, 1994; Wong, *et al.*, 1999; Amenitsch et al, 2004). However, they have also sparked an impressive number of applications in the construction of

biomolecular devices such as sensors (optical and electrical) (Pompeo, *et al.*, 2005; Sackmann, 1996; Amenitsch et al, 2004), the biofunctionalization of inorganic solids (Sackmann, 1996), and immobilization of proteins and DNA (Pompeo *et al.*, 2005; Sackmann, 1996; Amenitsch et al, 2004). Lipid multilayers (stacks of bilayers) have also been utilized for many different purposes. The main application of multilayers has been in light scattering techniques. The stacked system enhances the scattering signal over that seen for monolayers and single bilayers (Amentisch *et al.*, 2004). However, multilayers also find usage as a model system for myelin in the central nervous system (Lanteri *et al.*, 2000), and in atomic force microscopy (AFM) where they are much more stable than monolayers when in contact with the tip (Lanteri *et al.*, 2000).

Much recent interest in the field of lipid bilayers has been devoted to developing cushioning systems that limit the bilayer's interaction with the substrate upon which they are formed. This interest came about as the utility of lipid bilayers to serve as model membranes became limited by their inability to incorporate transmembrane proteins (Wanger and Tamm, 2000; Sackmann, 1996; Naumann *et al.*, 2002; Kühner *et al.*, 1994; Wong, *et al.*, 1999; and Huang, 1985; Spinke *et al.*, 1992). Bilayers supported on glass or silica substrates are separated from the substrate by approximately 10-20 . While this distance is sufficient to maintain the lateral mobility of the lipids themselves, integral membrane proteins interact with the hydrophilic substrate thus impeding their lateral mobility (Wagner and Tamm, 2000). Lipid bilayer cushioning systems would also be of importance because the roughness of the substrate upon which bilayers form prevents the undisturbed (self-) organization of lipids as a monomolecular layer (Spinke *et al.*, 1992). A cushioning system would "protect" the bilayer from the surface roughness and produce a more fluid membrane. Several

different methods have been proposed to make bilayer cushions (Wanger and Tamm, 2000; Sackmann, 1996; Naumann *et al.*, 2002; Kühner *et al.*, 1994; Wong, *et al.*, 1999; Huang, 1985; Spinke *et al.*, 1992). Many involve the use of polymers or ultra thin polymer films like dextran (Sackmann, 1996). Recently, biotinylated lipid bilayers have also been formed on a layer of streptavidin (Proux-Delrouyre *et al.*, 2002; Berquand *et al.*, 2003).

Another possibility in the field of lipid layers is to construct a system of stacked bilayers utilizing the interaction of avidin (or one of its chemical derivatives) and biotin. Avidin is a homotetrameric protein found natively in egg white (Lieto, 2003). Avidin binds four molecules of D-biotin with one of the highest affinity coefficients found in nature ($K_d \sim 10^{-15}$ M). Due to its large affinity coefficient, avidin or streptavidin (a bacterial protein similar in structure to avidin) has seen many applications. Two binding sites are found on each side of avidin or streptavidin and one molecule of avidin has the approximate size of 56 x 50 x 40 (Rosano *et al.*, 1999; Livnah *et al.*, 1993). Before a bilayer was built upon a layer of avidin, the use of avidin in lipid layers was well described. This began with the binding of avidin to biotinylated monolayers (Schmidt *et al.*, 1992; Zhao and Reichert, 1992; Zhao *et al.*, 1993), bilayers (Spinke *et al.*, 1992; Edmiston and Saavedra, 1998; Kaasgaard *et al.*, 2002), and vesicles (Chiruvolu *et al.*, 1994).

The stacked system we propose involves the fusion and adsorption of vesicles upon a fused silica substrate to form a biotinylated bilayer. Then the bilayer is treated with NeutrAvidin. NeutrAvidin is a commercially available derivative of avidin that has reduced nonspecific adsorption as compared to Avidin or Streptavidin. Finally, a second set of biotinylated lipid vesicles is applied and allowed to form a bilayer (Figure 3.1). We have characterized this system and its continuity using various fluorescence techniques (FPPR,

order parameter measurements, and intensity measurements) and AFM. This stacked system would bring together many diverse participants in the world of lipid layers including lipid multilayers, bilayer cushioning systems, and model biological membranes. Due to its versatility, the stacked bilayer system is likely to have applicability beyond what is now imagined.

Figure 3.1 Stacked Bilayer System.
A primary bilayer containing 0.3% biotinylated lipids is formed by vesicle fusion on a fused silica substrate. This bilayer is then treated with NeutrAvidin, and then a second bilayer is deposited by vesicle fusion atop the NeutrAvidin.

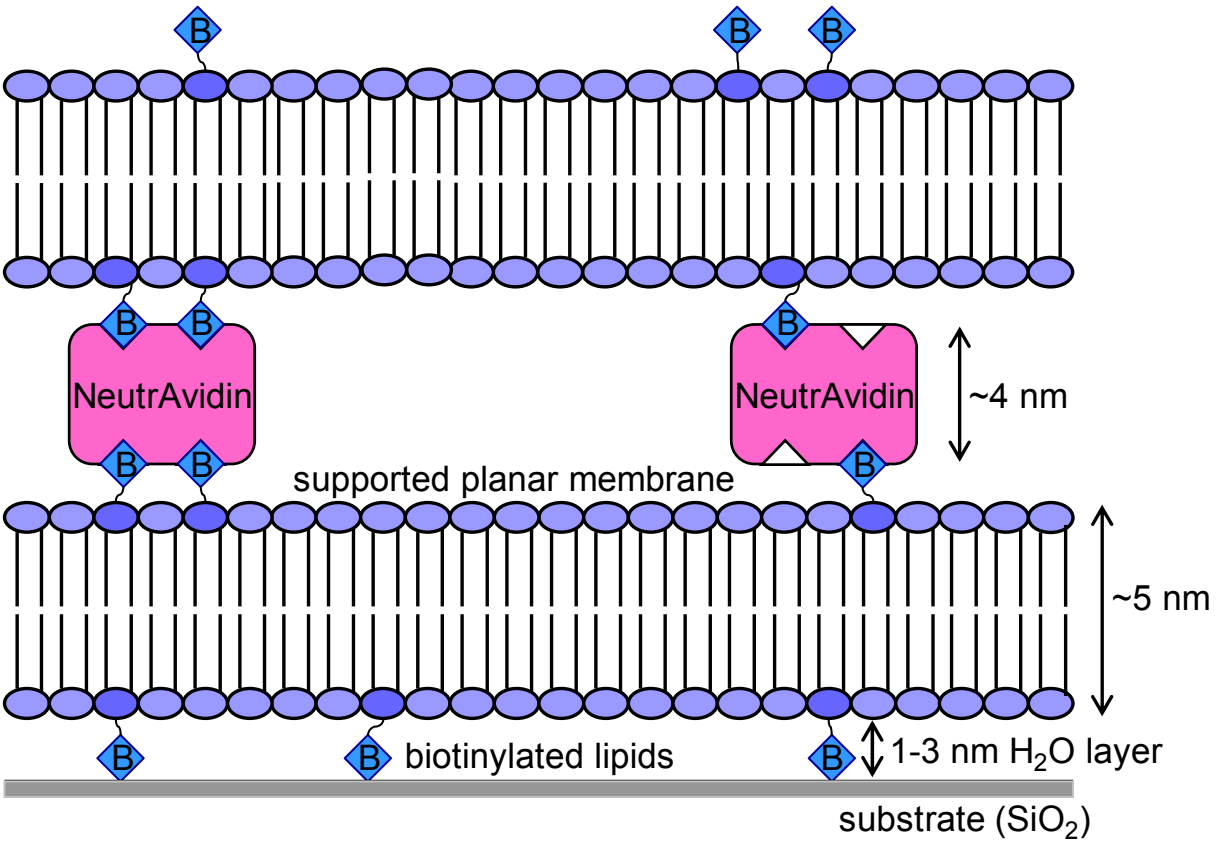

3.3 Theoretical Background

3.3.1 Fluorescence Pattern Photobleaching Recovery (FPPR)

Fluorescence pattern photobleaching recovery (FPPR) is a technique that can measure the translational mobility of bound proteins and phospholipid bilayers (Starr and Thompson, 2002). FPPR utilizes a Ronchi ruling placed at the back image plane of the microscope to create a spatial gradient of both the fluorescence observation and bleaching intensity in an expanded Gaussian beam. The utility in this technique is that samples are first hit by an intense brief pulse of light which effectively bleaches all molecules touched by the laser's radiation. A subsequent post bleach fluorescence recovery is then due to unbleached molecules moving from the non-illuminated regions into the laser beam's path. Assuming one had a sample in which the fluorescent species were 100% mobile, a maximum recovery in the fluorescence would lie midway between the pre-bleach and post-bleach fluorescence intensity. The recovery in the fluorescence intensity can then be used to extrapolate information about molecular movement within the sample and obtain a diffusion coefficient (D) (Smith and McConnell, 1978; Starr and Thompson, 2000; Lieto, 2003)

$$k_i = \left(\frac{2\pi}{a}\right)^2 D_i \tag{3.1}$$

where k_i is the characteristic rate for the recovery of the ith species and a is the stripe periodicity. k_i can be found from the theoretical form for the shape of the fluorescence recovery curve

$$\frac{F(t)}{F(-)} = 1 - \beta + \frac{\beta}{2}\sum_{i=1}^{n} f_i \left[1 - \frac{8}{\pi^2}\left(e^{-k_i t} + \frac{1}{9}e^{-9k_i t} + \ldots\right)\right] \tag{3.2}$$

where $F(-)$ is the pre-bleach fluorescence ($t < 0$), β is the bleached fraction, n is the number of fluorophore populations, and f_i is the fraction of the fluorescence recovery associated with

the *i*th species. One premise in the use of this form of the recovery equation is that the illuminated area is much larger than the stripe periodicity. To ascertain that this premise is met control measurements are performed where the bleaching experiment is conducted without the Ronchi ruling so that the entire observation area is bleached. If the premise is true and fluorescence recovery from diffusing unbleached species outside the observation area is negligible, then the post-bleach fluorescence for this measurement will remain constant and show no recovery. However, if the control measurement demonstrates a fluorescent recovery, then a theoretical treatment for samples with multi-component diffusion in FPPR can be used (Starr and Thompson, 2002). This theoretical treatment can account for recovery from outside the observation area.

3.3.2 *F*-Statistics

The use of F-statistics in FPPR analysis came about in an attempt to explain why FPPR experimental data were not fitting the theoretical equations as well as one might hope (Wright *et al.*, 1988). It was found that by assuming there are two mobile fluorescent populations (*i*=2 in Eqs. 3.1 and 3.2) FPPR data often more adequately fit to Eq. 3.2 (Wright *et al.*, 1988). However, this is to be expected as *i*=2 introduces more free parameters for which to fit to in comparison to *i*=1. To prove that *i*=2 actually produces a more accurate representation of the experimental data a statistical approach must be pursued. The *F*-statistic equation mathematically probes the significance of the improvement of the fit by using an *n* species model over an *n*-1 species model

$$F_n = \frac{\chi^2_{n-1} - \chi^2_n}{2\chi^2_n}(N - 2n - 1) \tag{3.3}$$

where χ_n^2 is the chi-squared goodness-of-fit statistic (Taylor, 1982) for the n mobile species model function, and N is the number of data points. Mathematically, the n species model produces a significant improvement over the n-1 species model if F_n is greater than 3.

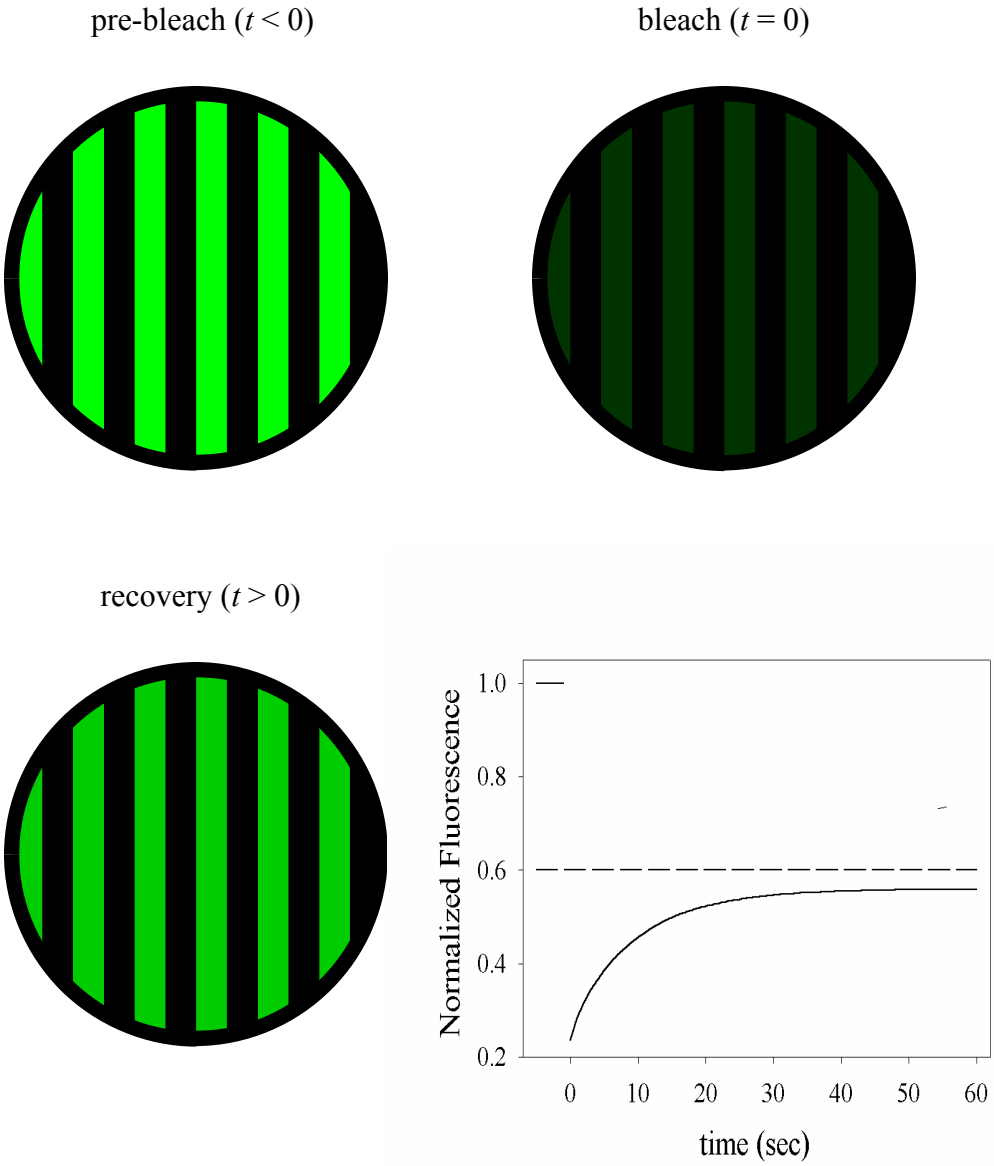

Figure 3.2 FPPR Experiment.
A Ronchi ruling is placed in the laser's path to create a stripe pattern. The sample is illuminated with less intense laser light and fluorescence is recorded (pre-bleach). The sample is then briefly illuminated by an intense beam of laser light that photobleaches the sample (bleach). Less intense laser light is then used to watch the fluorescent recovery of the sample as unbleached molecules diffuse into the observation area from behind the width of the stripe (recovery). The recovery is monitored and fit to Eq. 3.2.

3.3.3 Order Parameter Measurements

The evanescent light that propagates at the interface between two media of differing refractive index during total internal reflection is polarized. A consequence of the inherent polarization is that by altering the polarization angle of the incident light, it is possible to alter the polarization of the evanescent wave. The evanescent polarization can indirectly provide information about the order of the sample in which total internal reflection is occurring. Order parameter measurements utilize this principle to probe the orientation distribution of transition dipoles in phospholipid bilayers (Thompson *et al.*, 1984). Here the fluorescence is recorded as a function of the excitation light's polarization. As the excitation light rotates through all possible orientation angles, the evanescent light rotates primarily between perpendicular and parallel to the interface and provides information about the polar tilt angle (Lieto, 2003). When using epi-illumination, the light propagates normal to the surface and yields information about the azimuthal asymmetry in the orientation distribution (Thompson *et al.*, 1984; Timbs and Thompson, 1990).

The experiment is performed with a high numerical aperture that collects approximately half of the light that is emitted. It is the change in fluorescent intensity as the polarization angle is rotated that provides insights in the order of the system. The light that is emitted as well as absorbed is dependent upon the distribution of the absorption dipole orientations. The theoretical equation for azimuthally asymmetric samples that have been normalized to one is

$$F(\psi) = 1 + B(\cos^2 \psi - \cos^2 \psi_0) \tag{3.4}$$

where ψ is the angle that the beam polarization makes with the incidence plane, ψ_0 is the angle at which $F(\psi)$ is a maximum (0 or 90°), and B is a measured constant (positive or

negative, respectively). The constant B depends on the following parameters: (1) the evanescent field polarization, which depends on the incident angle (α) and polarization (ψ) of the totally internally reflected beam, and the relative refractive index of the substrate/solution interface (n); (2) the dichroic factor (γ), which describes the relative fluorescence collection efficiency for emission dipoles oriented perpendicular or parallel to the optical axis of the objective; and (3) the orientation distribution of fluorophore absorption dipoles, $N(\theta)$ (Lieto, 2003). The orientation distribution of dipoles is normalized to one and is written as an expansion in Legendre polynomials P_i, with order parameters s_i,

$$N(\theta) = \sum_{i=1}^{\infty} s_i P_i(\cos\theta)$$
$$\int_{allspace} N(\theta)\sin\theta d\theta = 1 \qquad (3.5)$$

The only order parameters in $N(\theta)$ that affect B are s_2 and s_4. In the theoretically ideal situation, when $\gamma = 0$, B depends only on s_2 (Thompson *et al.*, 1984). Consequently, s_2 is often referred to as the order parameter. However, in experimental practice $\gamma \neq 0$ because the substrate affects the angular distribution of emitted fluorescence from the molecules with different orientations, and this causes that the fluorescence is not truly collected over 2π steradians.

Practically, even though $\gamma \neq 0$ the effect of s_4 has been found to be negligible for small values of γ (Timbs and Thompson, 1984). The value of γ for an experimental set-up similar to the one used here is 0.1 (Burghardt and Thompson, 1984). Consequently, it is assumed that information about the polar tilt angle is extracted from s_2.

3.3.4 Atomic Force Microscopy

AFM is a sensitive surface imaging technique that allows one to map surfaces on the nanometer scale. AFM came about as an extension of scanning tunneling microscopy

(STM). Scientists performing STM experiments noted that a finite force existed between the tip and sample when in close proximity (Binning and Quate, 1986). It was eventually realized that the finite force that existed between the tip and sample is that of a van der Waals force. The van der Waals attraction causes the cantilever tip to deflect as the surface of a sample changes. The advent of AFM extended STM to samples that were formerly off-limits including nonconductive, soft, and live biological samples (Yang *et al.*, 2002).

In AFM, a tip (often constructed of Si or Si_3N_4) is attached to a flexible cantilever that is oscillated by a vibration piezo (Fig. 3.3). The tip is rastered across the surface of a sample, and the cantilever moves and deflects as the surface features of a sample change on the atomic scale. These oscillations are detected by focusing a laser on the back of the tip, and a photodiode is used to detect oscillations in the light intensity. An image is created by plotting the z-movement of the piezo as a function of the x-y position (Yang *et al.*, 2002). The z-movement of the tip is related to its spring constant. The resonant frequency, f_o, of the spring system can be found by (Binning and Quate, 1986)

$$f_0 = \frac{1}{2\pi}\left(\frac{k}{m_o}\right)^{1/2} \tag{3.6}$$

where k is the spring constant, and m_o is the mass that loads the spring. An experimental consequence of this relationship is that AFM is susceptible to vibrational noise from the surrounding environment, and care must be taken to minimize it.

The widespread use of AFM has brought about many variations of the technique. However, AFM is mainly operated in two modes: contact and tapping mode. In contact mode, the tip is maintained in constant contact with the sample. Consequently, contact mode can be damaging to samples of an extremely soft nature. Alternatively, in tapping mode the tip gently taps along the surface (brought about by the vibration piezo) and images the

surface in a less invasive way. Contrarily, tapping mode provides less image resolution than contact mode.

AFM was originally conceived as a method to image atomic features in air. However, its application to biological samples necessitated that the technique be amended to imaging in liquid. Liquid imaging is now possible and AFM has been used to image many biologically relevant systems (Yang et al, 2002). Its application to planar model membranes and biological cell membranes has also been demonstrated (Lagerholm *et al.*, 2005; Yuan and Johnston, 2000; Rinia *et al.*, 2001; Pompeo *et al.*, 2005). With reference to lipid membranes structures, AFM is particularly advantageous due to its ability to image the surface nanostructure of lipids with high spatial resolution and in real time (Pompeo *et al.*, 2005). The advantageous nature of using AFM to study lipids is often most vividly realized in tapping mode.

Figure 3.3 Schematic of AFM.
A cantilever with a tip is oscillated by a vibration piezo and is rastered across the surface. A laser is tightly focused on the tip and the signal is recorded by a photodiode. Oscillations in the recorded light signal are representative of the surface morphology and allow an image of the surface to be produced. Figure courtesy of Asylum Research.

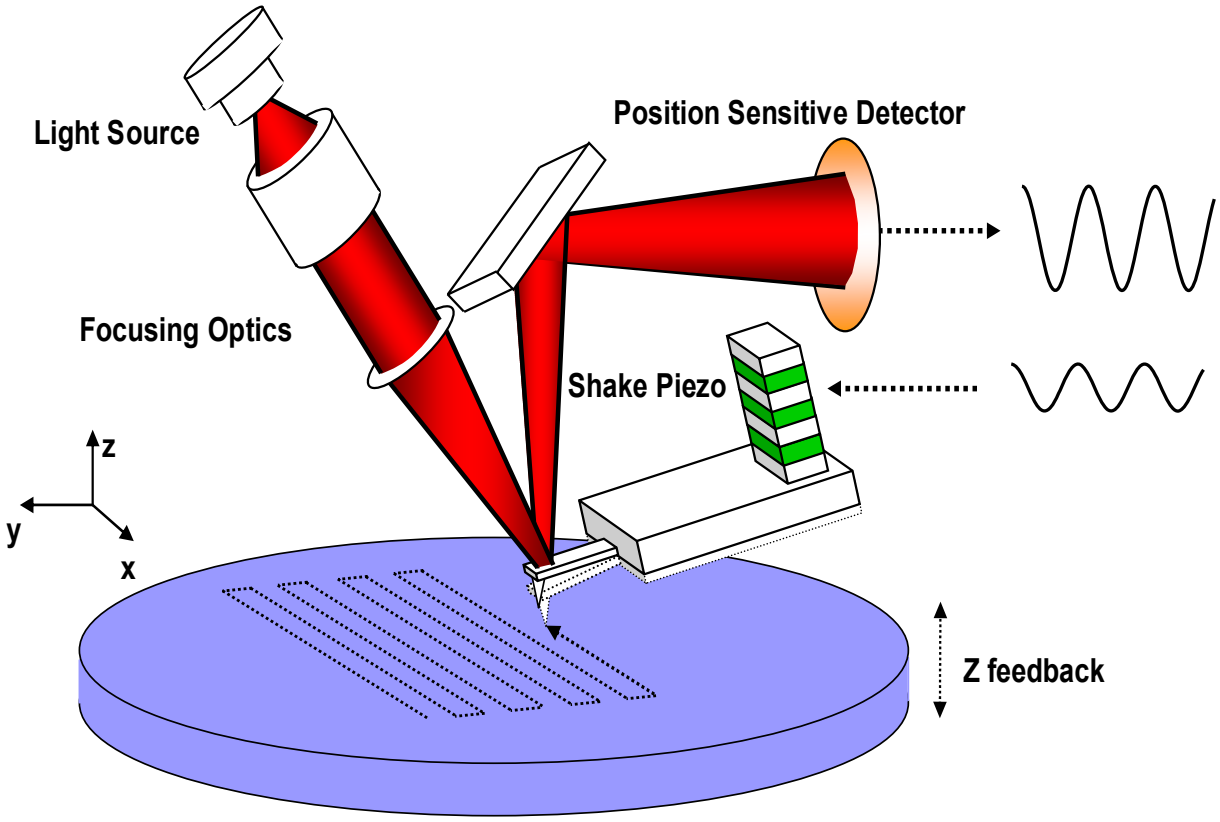

3.4 Materials and Methods

3.4.1 Avidin and Soluble Biotin

NeutrAvidin™ biotin-binding protein (60,000 MW) (Pierce, Rockford, IL) was dissolved in deionized water (dH_20) and either dialyzed into 1× PBS (NeutrAvidin is not directly soluble in PBS, so it must first be brought up in water), or combined with 5× PBS to bring the final buffer concentration to 1×, and stored at 4°C. For some control measurements

fluorescently labeled NeutrAvidin was utilized. A standard Thompson laboratory protocol for labeling with fluorescein isothiocyanate (FITC) was followed. NeutrAvidin (0.4–0.8 mg ml^{-1}) was first dialyzed into 0.1 M sodium bicarbonate buffer. Then a 20-50 molar excess of FITC was added from a 4 mg ml^{-1} solution in DMSO. The labeling reaction was allowed to proceed for 1 h at room temperature before the sample was passed down a Sephadex G-100 size exclusion column to remove the free dye and then immediately dialyzed into PBS. The concentration of NeutrAvidin and the molar ratio of FITC to protein (1.2–1.8) were determined spectrophotometrically with an extinction coefficient at 280 nm of 1.66 ml mg^{-1} cm^{-1} for NeutrAvidin (Pierce). NeutrAvidin was clarified by air ultracentrifugation (130,000*g*, 30 min) immediately before use to separate the heavier aggregates. To ensure that aggregates were not used during the experiments, NeutrAvidin was only taken from the top of the test tube.

3.4.2 Sonicated Vesicles

Small unilamellar vesicles (SUVs) were prepared from mixtures of 1-palmitoyl-2-oleoyl-*sn*-glycero-3-phosphocholine (POPC; 760.1 MW), 1-acyl-2-[12-[7-nitro-2-1,3-benzoxadiazol-4-yl]aminododecanoyl]-*sn*-glycero-3-phosphocholine (chain-labeled NBD-PC; 857.06 MW) (Avanti Polar-Lipids, Inc., Birmingham, AL), *N*-[6-[[biotinoyl]amino]hexanoyl]-dipalmitoyl-L-α-phosphatidylethanolamine, triethylammonium salt (Biotin-LC-DPPE; 1132.61 MW) (Pierce), and 1,2-Dipalmitoyl-*sn*-Glycero-3-Phosphoethanolamine-N-(Cap Biotinyl) (Sodium Salt) (Biotin-cap-DPPE; 1053.40 MW) (Avanti Polar-Lipids, Inc., Birmingham, AL) . Pierce discontinued production of Biotin-LC-DPPE midway through this project, and so Avanti's Biotin-cap-DPPE was utilized. It should be noted that they are the same molecule. Lipids were dried under vacuum for 30-90 min to

evaporate the chloroform solvent, suspended in dH_20 such that the total concentration of lipids was 2 mM, and tip sonicated (Fisher Sonic Dismembrator, Model 300 with intermediate titanium tip) (typically for 10-15 min at ~60% maximum power) on ice to form SUVs. Suspensions contained POPC and 0.3 mol% Biotin-LC-DPPE or Biotin-cap-DPPE. For fluorescence investigations, certain vesicle suspensions were made with the addition of 2 mol% NBD-PC. Vesicle suspensions were clarified immediately before use by air ultracentrifugation at 130,000*g* for 30 min.

3.4.3 Slide Cleaning

All microscope slides were cleaned with detergent and plasma cleaned immediately before use as described in Section 2.4.3. Sample dishes were soaked in Alkanox detergent overnight to remove any residual fluorophore from previous experiments and then rinsed thoroughly with two carboys of water. Immediately before use sample dishes were cleansed with ethanol and rinsed clean with dH_2O.

3.4.4 Intensity Measurement and FPPR Measurement Slide Preparation

Order parameter measurements and FPPR measurements were taken in sample dishes containing a small hole in the bottom and a No. 0 glass cover slip securely glued above the hole. This sample dish was filled with PBS buffer, and a fused silica substrate (1in x 1in x 1mm) (Quartz Scientific) rested inside the sample dish. The bilayer was adsorbed face-up on the fused silica. Initially this fused silica substrate was secured to a glass microscope slide (3 in × 1 in × 1 mm) with Teflon tape as the spacer (to ensure adequate space for bilayer formation). The bilayer was allowed to fuse and absorb here. Once bilayer formation was complete, the sample was placed under buffer and transferred to the sample dish for microscopy.

3.4.5 Order Parameter Measurement Slide Preparation

Order parameter measurements were conducted on slides made for use with total internal reflection microscopy (Section 2.4.3).

3.4.6 Atomic Force Microscopy Slide Preparation

Special slides were constructed for use on the AFM. A well was made on fused silica slides (3 in × 1 in × 1 mm) using "Plumber's Goop" (Lowe's Hardware) and allowed to dry overnight in a vacuum dessicator. Glass microscope slides (1.5 cm x 1.5 cm x 1 mm) with attached Teflon spacer were placed in the well and fastened to the slide using a binder clip. Vesicles were allowed to fuse and adsorb between these two slides. Immediately before measurements, the samples were placed under buffer and the glass slide was discarded. Care was taken to ensure that the well had adequate buffer to avoid exposure of the bilayer to air.

3.4.7 Sample Preparation

Primary planar bilayers were formed by applying at least 65 µl of a vesicle suspension to the substrates (30–60 min, 25°C), and then rinsing with 3 ml of PBS. For samples containing NeutrAvidin, 250 µl of 20 (only for experiments in Section 3.5.3) or 40 µg ml^{-1} NeutrAvidin in PBS was added (30 min, 25°C), followed by rinsing with 3 ml of PBS. For samples with a second bilayer, 250 µl of a vesicle suspension was added (60 min, 25°C), followed by rinsing with 3 ml of PBS. For negative control measurements when investigating the specificity of NeutrAvidin binding to Biotin-LC-DPPE, either primary bilayers were formed without biotinylated lipids or a high molar excess of free biotin (100x or 500x) was added to the NeutrAvidin before application to the primary bilayers. When measuring fluorescence intensities of samples, background samples contained only PBS.

3.4.8 FPPR and Intensity Measurements

Experiments were carried out at 25°C using the 488 nm line of an argon ion laser, in combination with an inverted microscope and a PMT as described in Section 2.4.5. A Ronchi ruling (50 lines per inch) was inserted in a back image plane of the microscope projecting a striped pattern onto the sample plane with a periodicity of 19.5 μm. The excited fluorescence was collected through an image plane aperture and a 40x, 0.75 NA water immersion objective. The laser power was set between 0.3-0.5 W for FPPR, and set to 50 mW for intensity measurements. Neutral density filters were inserted in its path such that the brightest sample yielded count rates in the range of ~1500-2500 counts per 50 ms interval when illuminated with the observation beam. For intensity measurements, the fluorescence counts were averaged over 2.5 s. For fluorescence pattern photobleaching recovery (FPPR) experiments, the bleach beam power was 81% of the total beam power (no filters), bleach pulse durations were 50–500 ms, and fractional bleach depths were 0.3–0.9. The ratio of bleach to observation intensity was typically ~10^4-10^6. Fluorescence recovery was typically monitored for 35–75 s after photobleaching, and data were curve-fit to theoretical forms using Sigma Plot 5.0

3.4.9 Order Parameter Measurements

For order parameter measurements, the laser beam was passed through a polarization rotator and was totally internally reflected at the substrate/solution interface through a fused silica prism; fluorescence was collected through a 60x, 1.4 N.A. oil immersion objective. The laser power was set at 50 mW. The observe beam was used to illuminate the samples, and neutral density filters were inserted in its path so that the count rate was always below 3000 counts per 50 ms time interval. This was done to ensure that the sample was not being

photobleached over the time period of the measurement. Fluorescence intensities were background subtracted and each sample was normalized to one. Correction factors for each polarization angle were determined so that $F(\psi)$ for a sample with randomly oriented fluorophore absorption dipoles (FITC-NeutrAvidin on fused silica) had B equal to the theoretically predicted value (see Eq. 3.4). For an incident angle $\alpha = 70°$ and relative refractive index $n = 0.909$, $B = 0.16$ for $\gamma = 0$, $B = 0.13$ for $\gamma = 0.1$, and $B = 0.09$ for $\gamma = 0.2$. Normalized and corrected data were fit to Eq. 3.4 with Sigma Plot 5.0.

3.4.10 Atomic Force Microscopy

All AFM images were obtained using a Molecular Force Probe 3D from Asylum Research (Santa Barbara, CA) controlled with Igor Pro 5.04B (Wavemetrics; Lake Oswego, OR). Olympus gold-coated "Biolever" cantilevers with nominal spring constants of 30 pN/nm (determined using the thermal noise method (Butt and Jaschke, 1995) were purchased from Asylum Research. Tips were cleaned with chloroform and gently dried in a stream of N_2. All AFM images were obtained with AC mode in water using Si_3N_4 tips at scan rates of 0.68 to 0.98 Hz. Images were analyzed using the MFP-3D software.

3.5 Results

3.5.1 Control Measurements

Seventeen different sample compositions (Table 3.1) were proposed to probe different aspects of the stacked bilayer system. The purpose of the various sample compositions was to investigate the nature of the stacked bilayer system, to compare the stacked bilayer to a single bilayer, to ascertain if a stacked bilayer was, in fact, formed, and to ascertain its continuity. The numerical identifiers for each sample type are maintained

throughout the rest of the paper. All sample types were formed by sonicated vesicles made as illustrated in Section 3.4.2.

Table 3.1 Sample Composition.

Sample Number	Primary Bilayer[a]	NeutrAvidin[b]	Secondary Bilayer
#1	B-POPC	No	No
#2	B-POPC	Yes	No
#3	B-POPC	No	B-POPC
#4	B-POPC	No	NBD-PC, B-POPC
#5	B-POPC	Yes	B-POPC
#6	B-POPC	Yes	NBD-PC, B-POPC
#7	NBD-PC, B-POPC	No	No
#8	NBD-PC, B-POPC	Yes	No
#9	NBD-PC, B-POPC	No	B-POPC
#10	NBD-PC, B-POPC	No	NBD-PC, B-POPC
#11	NBD-PC, B-POPC	Yes	B-POPC
#12	NBD-PC, B-POPC	Yes	NBD-PC, B-POPC
#13[c]	B-POPC	Yes (Fluorescent)	No
#14	B-POPC	Yes (Fluorescent)	B-POPC
#15	POPC	Yes (Fluorescent)	No
#16	NBD-PC, POPC	No	No
#17	NBD-PC, POPC	Yes	No

[a]Samples represented as B-POPC contain a mixture of 0.3 mol% Biotin-cap-DPPE (or Biotin-LC-DPPE) and 99.7% POPC. Samples represented as NBD-PC, B-POPC contain the same 0.3 mol% Biotin-cap-DPPE, and 2-3 mol% NBD-PC, and 96.7-97.7% POPC. Samples represented as NBD-PC, POPC contain 2-3 mol% NBD-PC and 97-98% POPC. [b]Samples with a yes located in the NeutrAvidin column were treated with 40 μg/ml NeutrAvidin in PBS. [c]For samples #13, #14, and #15 the NeutrAvidin was rendered fluorescent via reaction with FITC (see Section 3.4.1).

3.5.2 Intensity Measurements

Intensity measurements were performed on 1-4 samples/sample type using epi-illumination with a Ronchi ruling placed at the back image plane to aid in aligning the sample. Nine different spots were analyzed on each sample. During analysis data sets were analyzed by day, and each individual sample type was averaged together. The data were then background corrected using the average signal from sample #1-#3 and #5 as they should are essential background measurements. The data were then normalized to sample #7. After this

was done, it was then possible to average together all the data sets for one sample type (as the effects of taking the data at different intensities had been removed). Data can be seen in Table 3.2

Table 3.2 Fluorescence Intensity Results.

Sample #	Expected F[a]	Average F[b]
#1	0	0.02 ± 0.03
#2	0	0.02 ± 0.03
#3	0	0.02 ± 0.03
#4	0	0.19 ± 0.17
#5	0	0.02 ± 0.03
#6	F	0.57 ± 0.10
#7	F	1.00 ± 0.09
#8	F	0.97 ± 0.19
#9	F	0.80 ± 0.17
#10	F	0.97 ± 0.09
#11	F	0.70 ± 0.22
#12	2F	1.44 ± 0.21

[a]The expected fluorescence is an *a priori* estimate of the fluorescence assuming the sample composition is that of a stacked bilayer. [b]The average fluorescent signal is a compilation of 1-4 of days of data. 9 measurements were taken at different spots on each sample to get a more accurate representation of the variability within a sample. Uncertainties are standard deviations.

Samples #1, #2, #3, and #5 are effectively background measurements as they contain no fluorescent lipids. The low F values for these samples are indicative of no contamination. Sample #4 has no NeutrAvidin between the bilayers and consequently, the second bilayer should not form. As the second bilayer contains the fluorescent tag for this sample, it was anticipated that sample #4 should show no fluorescence. Experimentally, sample #4 displayed a small amount of fluorescence (0.19 ± 0.17) indicating possibly 20% nonspecific binding and/or lipid transfer. Sample #6 is similar to sample #4. Sample #6 differs because it contains the NeutrAvidin spacer and should form a secondary bilayer. The sample's experimental F value of 0.57 ± 0.10 is below the anticipated F value of 1. However, the

increase in F for sample #6 indicates that the stacked bilayer was possibly formed. The decrease in fluorescence under what was anticipated for the secondary bilayer is a theme that is realized throughout the fluorescence experiments.

Sample #7 is the benchmark, and all others samples were normalized by it. Sample #7 is a single fluorescent bilayer, and it displays the expected F value. Sample #8 is a single bilayer with the NeutrAvidin spacer on top, and its displayed F value of 0.97 ± 0.19 fits well with expectations. Sample #8 illustrates that the NeutrAvidin spacer does not interfere with the primary bilayer. The F value of Sample #9 is 0.80 ± 0.17, and it is 20% lower than what was anticipated. Sample #9 is two bilayers formed atop each other with no NeutrAvidin spacer. The results for sample #9 fit well with sample #4 and suggest 20% reverse lipid transfer. Sample #10 displays an F value of 0.97 ± 0.09 and fits well with expectation. As there was no increase in the fluorescence with the addition of a secondary bilayer with no NeutrAvidin, it argues against the theory that nonspecific binding is occurring. Sample #11 represents the stacked bilayer system, and its F-value of 0.70 ± 0.22 is a little lower than anticipated suggesting once again that a little lipid transfer is occurring. Sample #12 is also a stacked bilayer system in which both layers are fluorescent. The displayed F value of 1.44 ± 0.21 for sample #12 is lower than was assumed. The lower experimental F value fits well with sample #6 and indicates again that the stacked bilayer has lower fluorescence for the secondary layer. This is possibly due to the collection optics or incomplete formation of the secondary bilayer. Overall, the intensity experiments provide preliminary evidence for the formation of a stacked bilayer system.

3.5.3 Specificity of NeutrAvidin Binding to Biotinylated Lipids

To ascertain the specificity of the interaction between NeutrAvidin and biotinylated lipids, NeutrAvidin was fluorescently labeled and allowed to react with a nonfluorescent bilayer made of 0.3% Biotin-LC-DPPE and 99.7% POPC. The bilayer was treated with 20 or 40 μg/ml FITC-labeled NeutrAvidin (FNA). Additionally, two negative control samples were performed. The application of FNA to a bilayer composed of 100% POPC (no biotin) was the first negative control. The second negative control was performed by adding 100x or 500x molar excess of soluble biotin to the FNA prior to FNA application to the biotinylated bilayer. Theoretically, the soluble biotin should bind to the specific binding sites of the FNA and block its interaction with the biotin in the lipids. The data were taken by measuring the relative fluorescence intensity. The data were background corrected and normalized each day to sample #13 treated with 40 μg/ml FNA. The results are listed in Table 3.3. The control measurement confirmed that when there is no biotin in the lipids, FNA does not interact with the bilayer. Furthermore, treating FNA with an excess of biotin before its application to the biotinylated lipids blocks its binding sites, and in this state FNA does not interact with the biotinylated bilayer. Also, no significant difference was illustrated in the intensities measured from samples treated with 20 μg/ml vs. 40 μg/ml FNA indicating that the avidin-binding sites have been saturated.

Table 3.1 Relative Intensity of Fluorescent NeutrAvidin.

[FNA] (μg ml^{-1})	20	40
#13	1.0 ± 0.2	1 (normalized)
#15	0.04 ± 0.06	0.03 ± 0.03
100× or 500× molar excess soluble biotin (all bilayer types)	0.05 ± 0.05	0.06 ± 0.04

3.5.4 Mobility of FNA Bound to Biotinylated Lipids

The lateral mobility of FNA bound to biotinylated lipids was determined by using FPPR. FPPR curves were fit to Eq. 3.2 with *n=1* and *n=2*, and the F-statistics were performed to discriminate between the two fits. The data were better fit by a single mobile population for greater than 50% of the recovery curves. The results can be seen in table 3.4. They illustrate that FNA does not interfere with the fluidity of the single bilayer.

Table 3.2 FPPR Results for Fluorescently Labeled NeutrAvidin.

Fit model:	***n* = 1**		***n* = 2**				
Sample #	m^a	D (10^{-8} cm^2 s^{-1})	m_1	m_2	m_1+m_2	D_1 (10^{-8} cm^2 s^{-1})	D_2 (10^{-8} cm^2 s^{-1})
#13	78 ± 5	1.1 ± 0.2	56 ± 10	35 ± 9	92 ± 8	1.8 ± 0.3	0.3 ± 0.2

[a]The percent mobility, m=100*f* (Eq. 3.2). Parameters are averaged over approximately six spots per sample, two samples per day, and two days of experiments for each condition; uncertainties are standard deviations.

3.5.5 FPPR Measurements

The lateral diffusion coefficients and fractional mobility of various sample types were determined by FPPR. The reasoning behind determining the diffusion coefficients was twofold. First, one possibility in developing a stacked bilayer of this type is that the secondary bilayer does not form. In its place, it is possible that one finds large unfused vesicles. If there are large unfused vesicles, the diffusion coefficient might be much slower than that seen for a single bilayer. Secondly, if the secondary bilayer is continuous and well formed, the lipids should demonstrate a fluid nature seen in most bilayers. The continuity can be deduced by reference to the diffusion coefficient as it will provide information about long range lateral mobility. Results are shown in Table 3.5.

Table 3.5 FPPR Results on the Stacked Bilayer System and Its Variants.

Fit Model	***n*=1**		***n*=2**				
Sample #	m^a	$D(10^{-8}\ cm^2\ s^{-1})$	m_1	m_2	$m_1 + m_2$	$D_1(10^{-8}\ cm^2\ s^{-1})$	$D_2(10^{-8}\ cm^2\ s^{-1})$
#6	61 ± 5	0.9 ± 0.2	40 ± 5	44 ± 8	83 ± 6	3.7 ± 0.7	0.3 ± 0.1
#7	87 ± 3	1.4 ± 0.2	67 ± 10	31 ± 10	98 ± 14	2.7 ± 0.9	0.5 ± 0.3
#8	76 ± 16	0.8 ± 0.1	38 ± 7	60 ± 10	98 ± 5	3.9 ± 0.8	0.4 ± 0.2
#11	69 ± 6	0.8 ± 0.1	38 ± 4	51 ± 5	89 ± 6	2.7 ± 0.9	0.3 ± 0.2
#12	82 ± 4	1.4 ± 0.2	59 ± 12	33± 11	92 ± 17	3.0 ± 1.0	0.6 ± 0.3
#16	72 ± 9	0.9 ± 0.2	41 ± 6	52 ± 7	93 ± 6	4.2 ± 1.1	0.4 ± 0.2
#17	73 ± 7	0.7 ± 0.1	38 ± 4	59 ± 6	97 ± 3	4.4 ± 0.7	0.3 ± 0.2

[a]The percent mobility, m=100*f* (Eq. 3.2). Parameters are averaged over approximately 6 spots per sample, and 1-10 days of experiments for each sample condition; uncertainties are standard deviations.

Fluorescence recovery curves were fit to Eq. 3.2 with *n*=1 and *n*=2, and an F-statistic analysis was performed (Eq. 3.3). All samples were fit better by two mobile populations in greater than 98% of the curves analyzed. Representative curves are shown in Figure 3.4.

Figure 3.4 Representative FPPR Recovery Curves.

Diffusion coefficients were determined for seven samples using FPPR. a) Sample #7 was a single bilayer fit to *n=1* populations. The best fit of this particular curve to Eq. 3.2 produced f_1=0.91, D_1= 1.45 x 10^{-8} cm^2 s^{-1}, and β=0.7. b) Sample #7 fit to *n=2* populations. The best fit gave $f_1 = 0.73$, $f_2 = 0.26$, $D_1 = 2.4 \times 10^{-8}$ cm^2 sec^{-1}, $D_2 = 0.5 \times 10^{-8}$ cm^2 s^{-1}, and $\beta = 0.7$. c) The data are for sample #12. The best fit of the data to Eq. 3.2 with *n*=1 populations gave f_1=0.78, D_1= 1.45 x 10^{-8} cm^2 s^{-1}, and β=0.7. d) Sample #12 fit to Eq. 3.2 with *n*=2 populations gave $f_1 = 0.52$, $f_2 = 0.33$, $D_1 = 2.9 \times 10^{-8}$ cm^2 sec^{-1}, $D_2 = 0.7 \times 10^{-8}$ cm^2 s^{-1}, and $\beta = 0.7$.

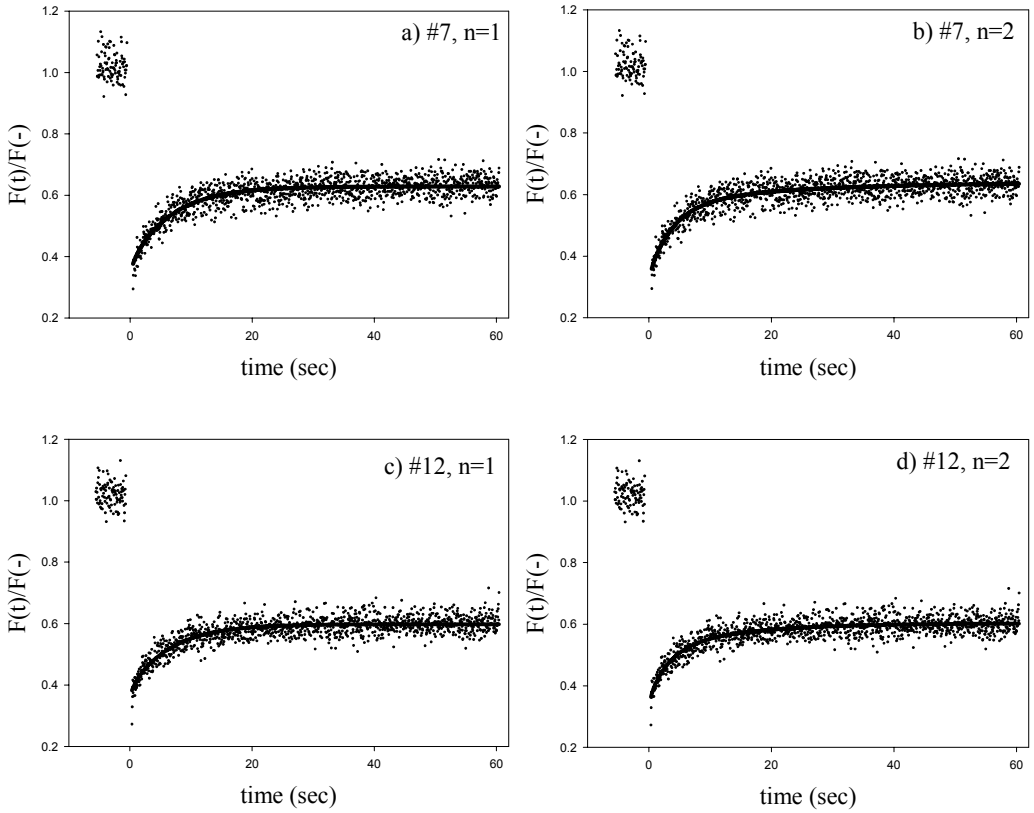

All the samples show plausible diffusion coefficients for lipid mobility in bilayers. Sample #6 particularly addresses lateral mobility in the second layer of a stacked system. Because the diffusion coefficient is within the error that would be expected for a bilayer, sample #6 provides evidence for the formation and continuity of the secondary bilayer. Sample #7 is a control measurement, and it particularly looks at a single bilayer for comparison with the stacked system. Sample #8 addresses the influence that the binding of NeutrAvidin has upon lipid mobility. The diffusion coefficient for Sample #8 yields further information that NeutrAvidin does not impede the fluid mosaic nature of the bilayer. The reasonable diffusion coefficient of sample #11 indicates that the formation of a secondary bilayer atop a primary bilayer does not destroy or interfere with the mobility of the primary bilayer. Sample #12 probes the overall mobility within the stacked system and the diffusion coefficient is indicative of continuity. The mobility of FNA was also measured in the stacked system (between bilayers), and was found to be greatly reduced compared to FNA bound to a single bilayer (data not shown). Overall, the FPPR studies of the stacked bilayer system provide further proof supporting the formation of a true stacked system.

3.5.6 Order Parameter Measurements

Order parameter measurements were performed to determine the orientation distribution ($N(\theta)$) of the absorption dipoles of the NBD-PC or FNA incorporated into the various sample types. The order found in the fluorescent lipids incorporated in the bilayer should be representative of the overall order found in the bilayer. Consequently, this set of experiments should provide information about the order found in the stacked system. The average intensity as measured by epi-illumination was recorded for four spots/sample, in 10° increments, as the polarization was rotated from 0° to 180°. Samples were background

corrected and then normalized by the largest value for each sample type performed on that data. Theoretical plots were made of $F(\psi)$ for a sample with randomly orientated dipoles at theoretical B values (Eq. 3.4) of 0.16. 0.13, and 0.09. These theoretical values for $F(\psi)$ were then used to determine correction values for each angle by dividing the theoretical values by the average values measured for the random sample (FNA). The data were multiplied by the correction factors and fit to Eq. 3.4. Values for B were determined and can be found in Table 3.6.

Table 3.6 Order Parameter Fits.

Sample #	γ=0, B_{random}=0.16	γ=0.1, B_{random}=0.13	γ=0.2, B_{random}=0.09
FNA	-0.16± 6.5e-17	0.15±6.6e-17	0.1±7.3e-17
#4	-0.23±0.04	-0.28±0.04	-0.25±0.03
#6	-0.54±0.01	-0.56±0.01	-0.56±0.03
#7	-0.49±0.02	-0.51±0.02	-0.53±0.02
#8	-0.49±0.01	-0.51±0.01	-0.53±0.01
#9	-0.48±0.01	-0.50±0.01	-0.52±0.01
#10	-0.51±0.01	-0.53±0.01	-0.55±0.01
#11	-0.50±0.01	-0.52±0.01	-0.54±0.01
#12	-0.50±0.01	-0.52±0.01	-0.54±0.01
#13	0.04±0.02	0.02±0.02	-0.05±0.02
#14	0.07±0.02	0.04±0.02	0.01±0.02

Representative curves for all sample types are displayed in Figure 3.5. The values of B determined for similar systems agree well with sample #6 - #12 (Thompson *et al.*, 1984; Timbs and Thompson, 1990; Pearce, 1993). This is indicative of order in these systems providing further support for the formation of a stacked bilayer system. FNA, sample #13, and sample #14 should show no order, and this fits well with what is seen experimentally. Sample #4 follows the theme set by it during the intensity measurements (Section 3.5.2). Sample #4 should display no order as the fluorescent lipid is in the secondary bilayer, and no NeutrAvidin was applied. However, sample #4 displays a small amount of order lending

proof to the hypothesis that some combination of nonspecific binding and lipid transfer is occurring. Overall, the order parameter measurements provide one more piece of proof for the existence of a stacked bilayer system.

Figure 3.5 Representative Order Parameter Curves.
Representative curves are shown for all sample types. All curves shown here were fit to Eq. 3.4 using the correction factor determined assuming a theoretical *B* value of 0.16.

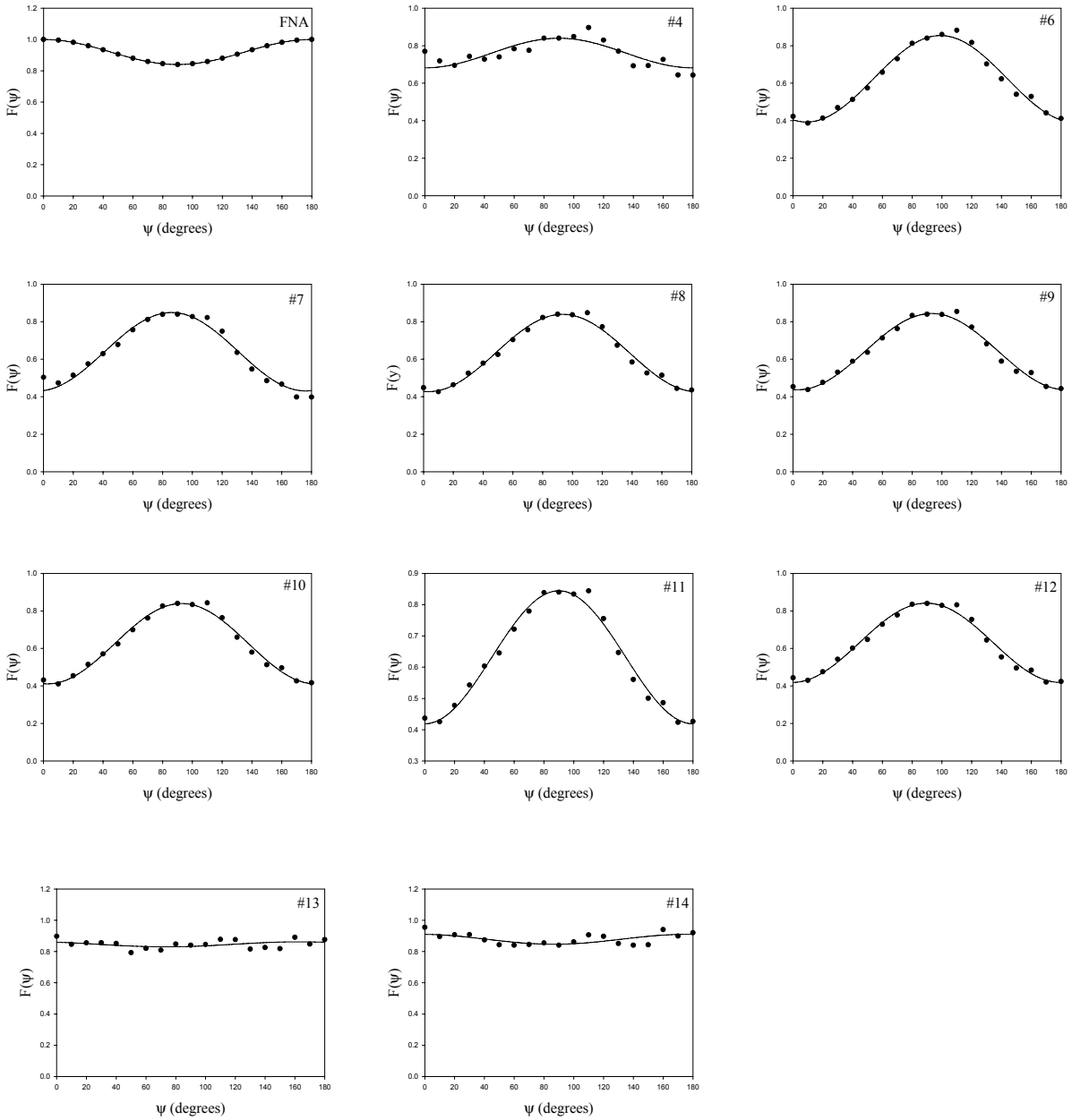

3.5.7 AFM Measurements

As a final characterization of the stacked bilayer system not available via fluorescence microscopy, AFM was employed due to its utility to provide accurate height measurements from the three dimensional surface maps. Specifically, it is anticipated that a bilayer is approximately 5 nm in diameter while NeutrAvidin is approximately 4 nm in diameter. Therefore, the stacked system should be about 14 nm in height with about 1 nm of water between the substrate and the bilayer system. Single bilayers often contain "holes" or regions where the bilayer is not completely continuous and the substrate shows through. The stacked system is likely to contain these holes as well. However, what will distinguish the stacked system from a single bilayer is that it is plausible to expect the holes to be of depths corresponding to the layer thickness. These multiple depths would be due to a hole in the secondary bilayer (5nm), a hole in the secondary bilayer and a missing NeutrAvidin molecule (9nm), or a hole in the stacked system (14 nm). It was anticipated that these holes would be evident in AFM images. Furthermore, they should be made readily more apparent by analysis of a height trace.

Three of the seventeen presented sample types were investigated using AFM. The samples include the primary bilayer (sample #1), the primary bilayer and attached NeutrAvidin (sample #2), the stacked bilayer system (sample #5), and as a control, the bare fused silica substrate (data not shown). However, data obtained for sample #2 was not useable. In retrospect, this is believed to be caused by the biotinylated lipids adhering to the tip, then interacting with exposed NeutrAvidin in other regions of the scan area. This biotin-NeutrAvidin interaction between the tip and planar bilayers caused large interactive forces between the tip and the sample. Consequently, such significant adhesion occasionally

occurred when scanning sample #2 that the tip and substrate had to be manually disengaged and incomplete images were obtained. Similar problems were encountered with sample #5 but to a lesser extent. Representative images and height traces of samples #1 and #5 are shown in Figure 3.6.

Figure 3.6 Representative AFM Images.

All AFM images were obtained with AC mode in PBS buffer (pH 7.4) using Si_3N_4 tips at scan rates of 0.68 to 0.98 Hz. Corresponding section analyses are below respective images. a) Single bilayer showing holes of ca. 2.5 nm depth (*z-scale*: 5 nm). b) Stacked bilayer showing continuous nature of film. Section analysis traces separated to depict (z-scacle: 20 nm). c & d) Stacked bilayers showing holes of corresponding heights expected of the stacked system (*z-scale*: c: 15 nm, d: 25 nm). In c), Section analysis traces separated to clearly depict various hole depths.

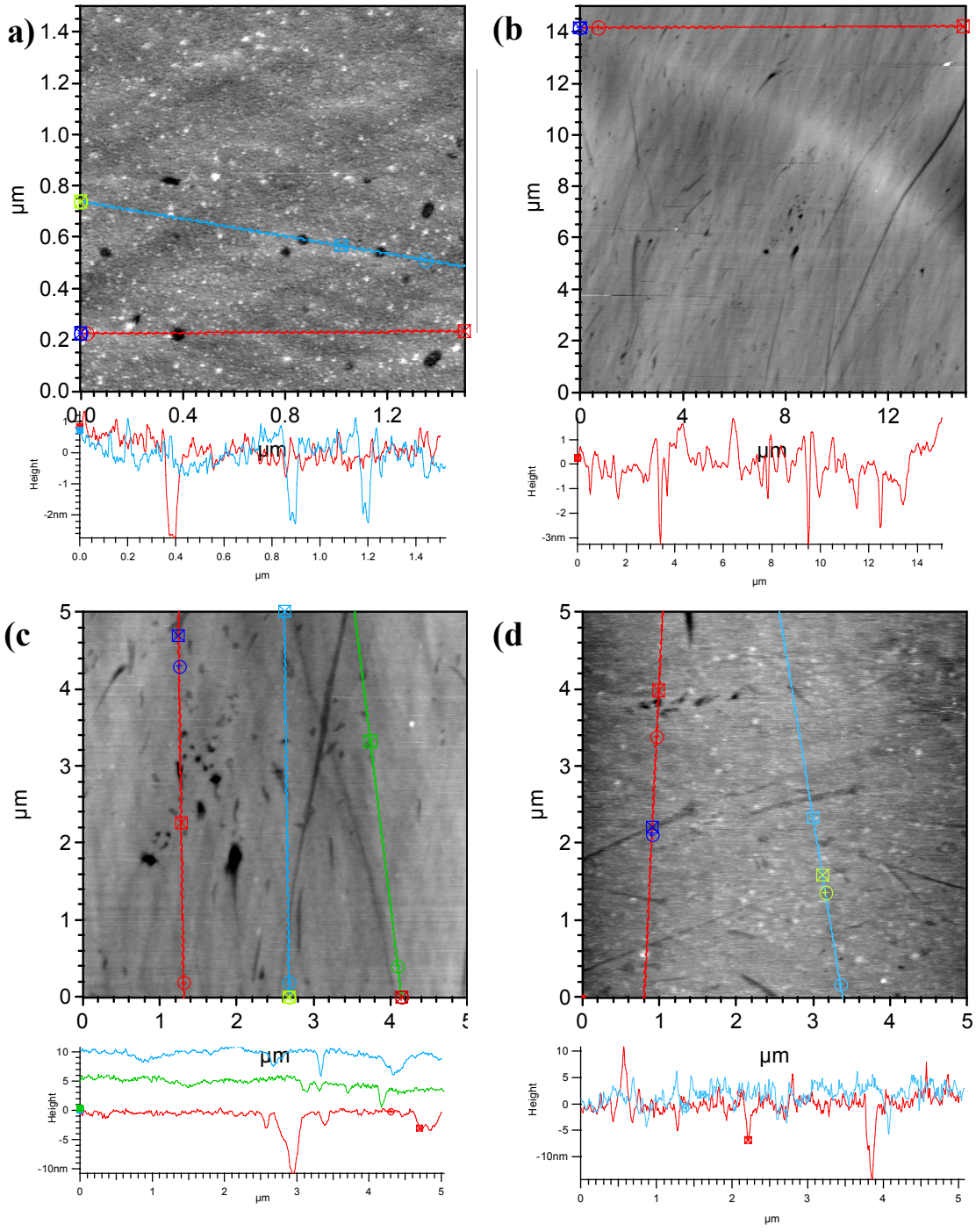

The AFM images provide more information about the nature of the stacked system. By analysis of the image in a) (the single bilayer), it is evident that the holes seen in the height trace are approximately 2.5 nm. The expected size of single bilayer is 5nm. Consequently, it would be reasonable to deduce that the holes are possibly missing pieces of one half of the bilayer (monolayers). However, this would expose the hydrophobic tails of the lipids to an aqueous environment creating an energetically unfavorable interaction. Although the holes of 2.5 nm cannot be identified, the image shows no holes larger than 5 nm and is thus consistent with a single bilayer. The images in Figure 3.6 (b-d) are images taken of the stacked bilayer system. The height trace in b) shows a region of the stacked system with few holes. Although this gives us no information to ensure that this is a stacked system, it does illustrate large regions (5 μm^2) of continuous bilayer. The image in c) demonstrates similar results with a few holes of z-scale 10 nm, 5 nm, and 2.5 nm. The height traces in d) illustrate holes of 15 nm, 5 nm, and 2.5 nm. These are consistent with the expected hole depths for a stacked system. Furthermore, the large depths of the holes eliminate the possibility that what was actually developed was a single bilayer with a layer of NeutrAvidin on top. Secondly, the holes are small enough to negate the possibility that the secondary structures atop NeutrAvidin are unfused vesicles (~50 nm). The majority of the height traces are uniform and continuous providing further evidence that the stacked system is homogenous.

3.6 Discussion

The use of planar model membranes has become an integral part of research and applied science. However, the continued use of model membranes requires that the methodology in building bilayers continues to keep apace of the necessities of ever

increasingly difficult experiments. This requires the amendment of existing techniques to newer protocols and their extension to more diverse ideas. New advancements required in model membrane technology include the need to create "free bilayers" that show little interaction with the substrate upon which they are formed, the need to create more continuous and controlled multilayers, and the need to insert biologically relevant molecules into model membranes.

To this end, we have created a stacked bilayer system using the interaction of biotinylated lipids and NeutrAvidin as a "lock and key" layering mechanism. Furthermore, we have characterized this putative system using four different techniques (three fluorescence techniques and atomic force microscopy). Through each of these techniques we have acquired evidence indicating that a stacked bilayer system was formed and that this system is relatively homogenous.

Through FPPR measures we have confirmed that the lipids are laterally mobile. This provides evidence indicating that the secondary bilayer is not mainly composed of unfused vesicles and the long range lateral mobility is consistent with a continuous bilayer. Order parameter measurements illustrated the stacked bilayer has a continuous order. This evidence is particularly compelling when compared to control measurements on derivatives of the stacked system that showed little or no order. However, the order parameter measurements indicate that some lipid transfer is occurring between bilayers. This transfer must be addressed and quantified if this new methodology is to find application.

The intensity measurements agreed with the order parameter measurements and indicated that lipid transfer is occurring. The intensity measurements indicated that the secondary bilayer is forming, but that it is less fluorescent than the primary bilayer. It is

unknown at this time why this is occurring. It was initially thought that this was indicative of incomplete bilayer coverage, but this possibility is less likely in view of the evidence provided by the other techniques. The reasons behind the less intense fluorescence in the secondary bilayer must also be addressed if this system is to be applied as a technique to experimental research. Finally, atomic force microscopy studies indicated that the stacked bilayer system exists and that it is mostly homogenous. Areas of the multilayer system show "holes." However, this is also seen in bilayers.

Future studies of the stacked bilayer system should attempt to incorporate transmembrane proteins into the stacked system. This was initially attempted in our lab. Results indicated that the protein was not appreciably mobile. However, more experiments must be conducted indicating why the protein is immobile and how the technology can be amended to correct this. The immobility of the protein could be due to simple design flaws in the experimental set-up. These must be investigated before it is assumed that the system is not utilizable here. A detailed characterization of the transmembrane protein integrated into the system must be performed in a manner similar to the system characterization seen here. However, it is anticipated that the stacked system should not be limited to application in this field. It is likely that the technique will be amendable to many studies.

In conclusion, we have devised a novel stacked bilayer system and characterized it using four different techniques. The system has been determined to be continuous and fluid. Its advent will likely find application in biomolecular devices, biofunctionalized inorganic surfaces, multilayer science, and as biological model membranes.

Chapter 4 High Refractive Index Substrates to Generate Very Small Evanescent Wave Depths

4.1 Abstract

The use of TiO_2 and $SrTiO_3$ single crystal substrates in fluorescence based experiments was investigated. The substrates were examined for their native luminescence, and it was concluded that both are extremely luminescent with 488 nm excitation. However, TiO_2 is less luminescent with 514 nm excitation and was consequently deemed more suited for use with an argon ion laser. Studies were conducted to ascertain what concentration of fluorescently labeled antibodies was required to overcome the native luminescence of the TiO_2 substrate at 514 nm. The TiO_2 substrate was utilized in experiments measuring the membrane-adjacent rate of diffusion of IgG antibodies by total internal reflection with fluorescence correlation spectroscopy. The calculated rate of diffusion at the TiO_2/solution interface was much higher than the experimentally determined rate of diffusion for IgG at the fused silica/solution interface. This value fits well with predictions from the theory for ligand diffusion near interfaces (chapter 2). This increased correlation rate corresponds to smaller evanescent wave depths. The TIR-FCS autocorrelation functions are relatively noisy. Further investigations are required to decrease this noise and continue the adaptation of high refractive index substrates to use with TIR-FCS. A novel surface quenching effect was observed where the substrate appeared to quench the fluorescence of fluorescently-labeled protein in the absence of phospholipid bilayers. Further studies into the origin of the

surface quenching effect might provide further insight into the intrinsic luminescence of TiO_2 or possibly provide a new surface characterization technique.

4.2 Introduction

Total internal reflection (TIR) has become a staple of the scientific community over the past two decades (Thompson and Pero, 2005). The myriad of techniques and problems for which it finds application continues to grow. TIR is closely linked and inherently suited to the study of supported phospholipid bilayers (Thompson and Pero, 20005; Sackmann, 1996; Starr and Thompson, 2000; Ajo-Franklin *et al.*, 2001). TIR has been applied in the field of fiber optics and biosensors (Lee, 2003; Kurrat *et al.*, 1997), microfluidics (Yang et al, 2001; Yang *et al.*, 2003), and genomic and proteomic assays (Lehr *et al.*, 2003). TIR has also been combined with numerous techniques to make them surface sensitive or obtain additional complementary information (fluorescence resonance energy transfer, atomic force microscopy, fluorescence correlation spectroscopy, fluorescence recovery after photobleaching, etc.).

One limitation in the use of TIR is the difficulty of obtaining very small evanescent wave depths. Very small evanescent wave depths would be intrinsically important because they would provide more information about surface chemistry closer to interfaces, extend TIR methodology to physical problems with weaker binding constants, and increase the z-axis resolution (Thompson and Pero, 2005). The difficulty in obtaining small evanescent wave depths arises because most TIR studies have been conducted at the interface of water and fused silica. Fused silica has been the medium of choice because it has a well characterized history as a substrate for model membranes; it has lower background fluorescence than glass; it is transparent in the UV and visible regions; and its refractive

index is greater than water (Thompson and Pero, 2005). For an interface between fused silica and water the critical angle is 65°. Consequently, working angles that can bring about TIR on a fused silica substrate are ~70°-85°. These angles produce corresponding z-depths of 63-104 nm by Eq. 4.1

$$d = \frac{\lambda}{4\pi\sqrt{n_1^2 \sin^2 \alpha - n_2^2}} \tag{4.1}$$

where d is the evanescent wave depth, λ is the vacuum wavelength of light, n_1 is the higher refractive index (fused silica), n_2 is the lower refractive index (water), and α is the incident angle of light (Thompson *et al.*, 1993). The incidence angle must be greater than the critical angle,

$$\alpha_c = \sin^{-1}(\frac{n_2}{n_1}) \tag{4.2}$$

where α_c is the critical angle.

One attempt to tweak this limitation and use TIR for depth profiling has been the advent of variable angle-total internal reflection (VA-TIR). VA-TIR utilizes the relationship between the incidence angle of the impinging laser and the depth of the evanescent wave to probe a sample at different depths from the interface by merely changing the incidence angle (Reichert *et al.*, 1987; Liebmann, 1991). This allows the sample to be studied at the full range of evanescent wave depths obtainable by TIR (63-104 nm at the fused silica/water interface). However, the true power of VA-TIR and TIR would be obtainable if samples could be probed at smaller depths.

By examination of Eq. 4.1, it becomes apparent that another way to obtain small evanescent wave depths would be to employ a substrate of much higher refractive index than that of SiO_2. A higher refractive index would produce much smaller evanescent wave

depths, a smaller critical angle, and the possibility of smaller incidence angles. These high refractive index substrates must display many of the intrinsic properties of fused silica if they are to be useful for TIR. They must permit the formation of model phospholipid bilayers if they are to see the wide application of TIR that fused silica has created. Much interest has been focused on TiO_2 and somewhat on $SrTiO_3$ for use as high refractive index substrates (n = 2.5 for both) (Starr and Thompson, 2000; Rossetti *et al.* 2005, Ajo-Franklin *et al.*, 2001; Reimhult *et al.*, 2003; Richter, 2006). A refractive index as high as 2.5 will require a slightly different experimental set-up than traditional total internal reflection where glycerin is used to couple a fused silica prism to a fused silica slide (Figure 4.1). This is because there are not many liquids with a refractive index of 2.5 by which the slide and prism could be coupled. Consequently, the bilayer must be directly formed on the prism.

Figure 4.1 Schematic for TIR with High Refractive Index Substrates.
Due to the lack of refractive index matching liquid, the bilayer is formed directly on the prism. TIR is then performed through the prism.

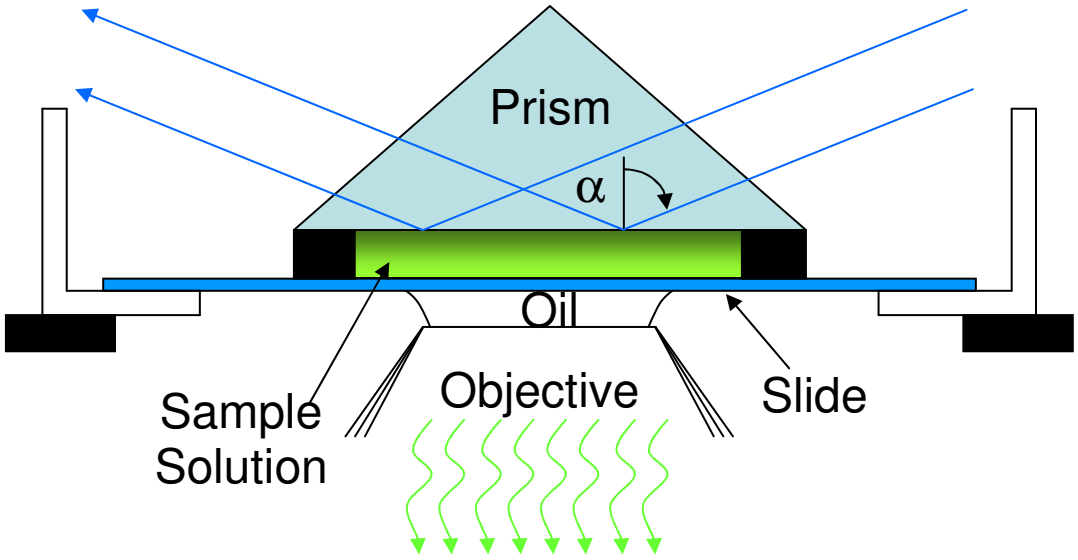

Titanium based single crystals are particularly of interest in this application for several reasons. First, titanium has already spawned much application in the biomedical field as an implant device in hip and knee joints, dental prosthetics, heart values, etc. The biocompatibility of titanium is a consequence of the native layer of oxide that coats its surface (Rosetti *et al.*, 2005) Furthermore, the combination of its biocompatibility and high refractive index make titanium an extremely good candidate for future biosensor applications given that it can be amended to use with TIR. It has already been proven that phospholipid bilayers can be formed on TiO_2 and $SrTiO_3$ (Starr and Thompson, 2000; Rosetti *et al.*, 2005). Although some reports have contrarily stated that titanium based materials oppose the formation of phospholipid bilayers (Ajo-Franklin *et al.*, 2001; Reimhult *et al.*, 2003), the general consensus remains today that bilayers do form on these substrates (Richter, 2006).

The use of high refractive index substrates would be of particular usefulness in the study of protein diffusion near model membranes. In chapter two, the size dependence of protein diffusion was measured. It was determined that as the diffusing proteins moved closer to the membrane, the rate of diffusion decreased as a function of protein radius due to increased frictional coefficients. A complementary study of protein diffusion near model membranes would be to monitor the diffusion as a function of z-distance from the membrane. This could be attempted using conventional VA-TIR. However, as Figure 4.2 illustrates the range of z-distances that can be probed using a fused silica substrate (63-104 nm) show little distance dependence. It is not until much smaller distances from the model membrane, that a dramatic distance dependence is theoretically predicted. TiO_2 and $SrTiO_3$ can produce evanescent wave depths of 18-43 nm. In this region, there is a much stronger distance dependence. By combining high refractive index substrates with VA-TIR, a systematic study of the distance dependence of protein diffusion very near model membranes would be plausible.

Figure 4.2 Theoretical Plot of Eq. 2.9.
Eq. 2.9 describes the diffusion of a particle in close proximity to a boundary. The equation relates the radius (r) of the particle, and the z distance from the interface to the diffusion. The equation is normalized by the diffusion one would expect in bulk solution ($D(\infty, r)$) or the Stokes-Einstein Equation.

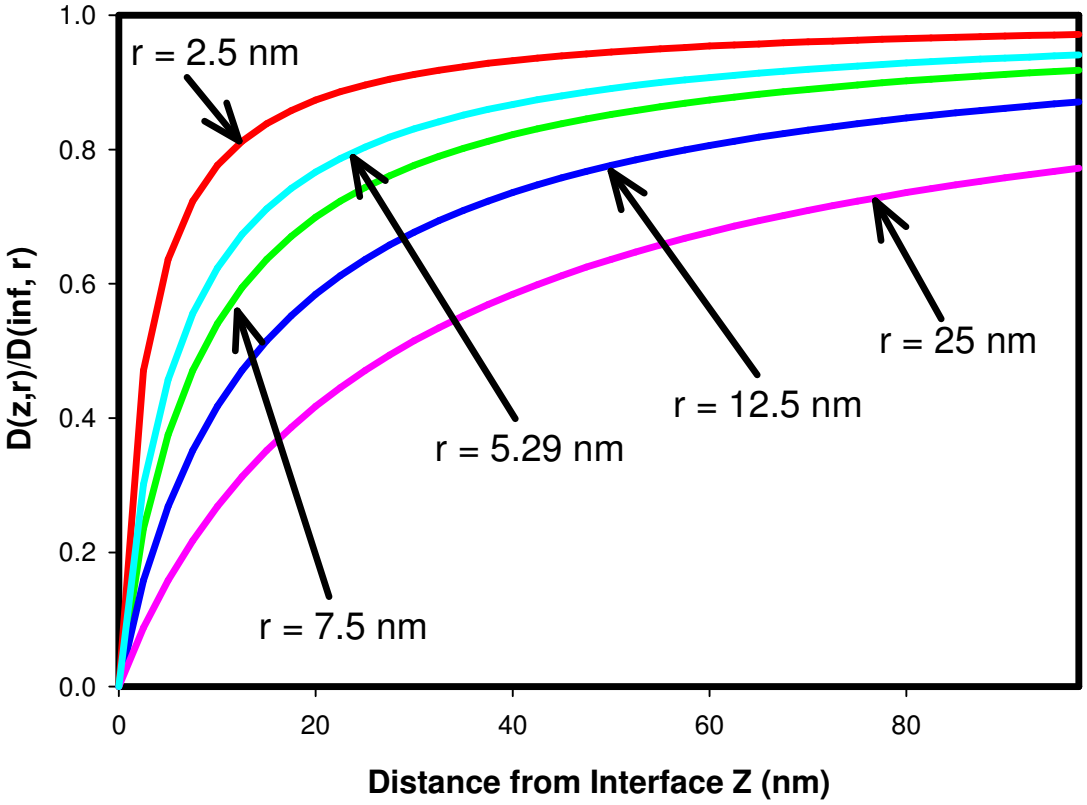

To this end we have begun the application of high refractive index substrates to total internal reflection based techniques. Particularly, TIR-FCS has been used to attempt to characterize the diffusion of Fab fragments and IgG fluorescently-labeled antibodies. There has been some success in this area, and some novel properties of TiO_2 and $SrTiO_3$ have been discovered.

4.3 Theoretical Background

4.3.1 TIR-FCS

The theoretical derivations of the autocorrelation function for these experiments were laid out in chapter 2. In the experiments utilizing high refractive index substrates, the diffusion of Fab fragments and IgG antibodies is measured very near model membranes. No surface binding or adsorption is expected; and consequently, the data should fit to Eq. 2.5. However, the autocorrelation functions performed atop $SrTiO_3$ and TiO_2 fit quite poorly to Eq. 2.5. A simplified limiting version of Eq. 2.5 was used

$$G(\tau) = \frac{1}{2N_e} e^{-R_e \tau} \qquad (4.3)$$

where N_e is the average number of molecules in the observation volume, and R_e is the rate of diffusion through the depth of the evanescent wave.

4.4 Materials and Methods

4.4.1 Substrate Preparation

Epitaxially polished TiO_2 and $SrTiO_3$ crystals (First Reaction, Hampton Falls, NH) were soaked in acetone for one to twenty four hours and rinsed twice with deionized water. No. zero coverslips (Gold Seal Coverglass, Clay Adams, UK) and fused silica slides (Quartz Scientific, Fairport Harbor, OH) were cleaned extensively by boiling in detergent (ICN, Aurora, OH), bath sonicating, rinsing thoroughly with deionized water, and drying at 160 ˚C. All substrates were cleaned in an argon ion plasma cleaner immediately prior to use (10 minutes, 25 °C) (PDC-3XG, Harrick Scientific, Ossining, NY).

4.4.2 Antibody Preparation

IgG antibodies were obtained from the anti-dinitrophenyl mouse-mouse hybridoma 1B711 (American Type Culture Collection, Rockville, MD). Hybridomas were maintained in culture, and the secreted antibodies were purified from cell supernatants by affinity chromatography with DNP-conjugated human serum albumin. Each liter of supernatant yielded approximately 10-15 mg of antibody as determined spectrophotometrically by assuming that the molar absorptivity at 280 nm was 1.4 mL mg^{-1} cm^{-1}. Fab antibodies (Jackson ImmunoResearch Laboratories) were dialyzed into phosphate-buffered saline (PBS; 0.05 M sodium phosphate, 0.15 M NaCl, pH 7.4). All antibodies were fluorescently labeled using the AlexaFluor514 Protein Labeling Kit (Molecular Probes, Inc., Eugene OR) and the AlexaFluor488 Protein Labeling Kit. The free dye was removed by using size exclusion chromatography with Sephadex G-25 or G-50 in PBS. The molar concentrations of antibody and the molar ratios of AlexaFluor514 or AlexaFluor488 to antibody were determined spectrophotometrically according to the manufacturer's protocol.

4.4.3 Phospholipid Vesicles

Small unilamellar vesicles of 1-palmitoyl-2-oleoyl-glycero-3-phosphocholine (POPC) (Avanti Polar Lipids, Birmingham, AL) were prepared by tip sonication of 2 mM suspensions of POPC or POPC/cholesterol in water as previously described (Lagerholm *et al.*, 2000). In fluorescence imaging experiments, 2 mol% of the fluorescent lipid 1-acyl-2-[12-(7-nitro-2-1,3-benzoxadiazol-4-yl) aminododecanoyl]-glycero-3-phophocholine (NBD-PC) was included to monitor bilayer formation and quality, and to replicate previous experiments (Starr and Thompson, 2000) that indicated that bilayers can be formed on titanium based crystals. Vesicle suspensions were clarified by air ultracentrifugation (130,000*g*, 30 min) immediately before use.

4.4.4 Substrate-Supported Phospholipid Bilayers

Supported planar bilayers were deposited onto clean substrates by vesicle adsorption. For fluorescence imaging experiments, TiO_2, $SrTiO_3$, and fused silica substrates were separated by a Teflon spacer; and 65 μL of vesicle containing solution was applied to the substrates (1 h, 25 °C). Then the slide was rinsed with 3 mL of PBS buffer. Slides were sealed with either Elmer's glue (Elmer's products, Inc., Columbus, OH), rubber cement (Ross Products, Inc., Columbus, OH), or clear nail polish (Sally Hanson Teflon Tuff, Del Laboratories, Inc., Farmingate, NY). For TIR-FCS experiments TiO_2 and $SrTiO_3$ prisms were separated by a Teflon spacer and 20 μL of vesicle containing solution was applied to the prisms (1h, 25 °C) and washed with 400 μL of PBS. Slides were sealed using rubber cement.

4.4.5 Fluorescence Imaging

Epifluorescence images were taken on an instrument consisting of an inverted microscope (Zeiss Axiovert 35 with a 40x 0.75 NA objective) and a charge-coupled device (CCD) camera (AT200 Photometrics Ltd. Tucson, AZ). Bilayers were exposed to laser light for times ranging from 100 to 500 ms with a laser power of 50 mW.

4.4.6 TIR-FCS Experiments

TIR-FCS was carried out on an instrument consisting of an argon ion laser (Innova 90-3; Coherent, Palo Alto, CA), an inverted microscope (Zeiss Axiovert 35), and a single-photon counting photomultiplier (RCA C31034A, Lancaster, PA). All experiments were conducted at 25 °C using the 514 nm laser line. For TIR-FCS measurements, the laser beam was s-polarized while incident on the substrate/aqueous interface and generated an evanescent field polarized parallel to the interface. TIR-FCS experiments were performed

with a pinhole with a radius of 50 μm placed at an internal image plane which defined an area with a radius of h $\approx$ 1 μm when projected onto the sample plane. The fluorescence arising from the volume defined by the excitation light and the pinhole was collected through a 100x, 1.3 N.A. objective. The fluorescence signal was autocorrelated by a PC-based correlator board (model 5000/E, ALV). Autocorrelation functions were obtained within 5-10 minutes using incident laser intensities of 4-17 $\mu W/\mu m^2$. Average blank signals were measured from samples containing buffer adjacent to supported bilayers.

4.4.7 Data Analysis

Autocorrelation functions were background-corrected by multiplying by the factor $\langle S\rangle^2/\langle F\rangle^2$, where $\langle F\rangle = \langle S\rangle - \langle B\rangle$ was the average fluorescence calculated by subtracting the average measured blank signal $\langle B\rangle$ from the average measured total signal $\langle S\rangle$. TIR-FCS autocorrelation functions were fit to Eq. 4.3 plus an arbitrary constant G_∞, and the free parameters were R_e, N_e, and G_∞ (see Chapter 2).

4.5 Results

4.5.1 Fluorescence Imaging

To confirm that phospholipid bilayers can be formed upon TiO_2 and $SrTiO_3$, experiments identical to those previously conducted in this lab (Starr and Thompson, 2000) were repeated. Bilayers were only created using vesicle fusion and results can be seen in Figure 4.3. As the fluorescence images show, homogenous and continuous bilayers were made atop high refractive index substrates. It is also important to note that the TiO_2 and $SrTiO_3$ crystals had not recently been polished and that the crystals had been used and cleaned several times since polishing. It was suggested that the formation of bilayers atop

titanium-based materials was due to a silica residue created by polishing (Ajo-Franklin *et al.*, 2001).

Figure 4.3 Epi-fluorescence Images of Bilayers atop SiO_2, TiO_2, and $SrTiO_3$. Bilayers were formed by adsorption and fusion of POPC/NBD-PC or POPC/Cholesterol/NBD-PC atop a) fused silica, b) $SrTiO_3$ and c) TiO_2. Each sample was exposed to 50mW laser light for 200 ms.

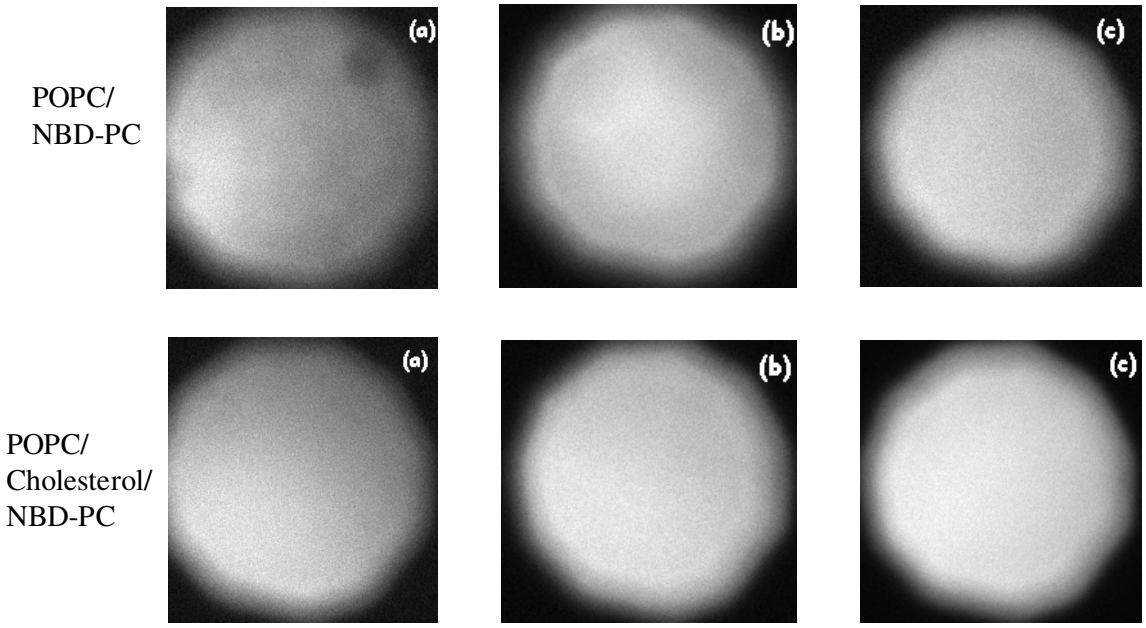

It was previously reported that the TiO_2 and $SrTiO_3$ substrates exhibited decreased fluorescence intensity when compared to SiO_2 during these experiments (Starr and Thompson, 2000). The same phenomenon was observed here. It is interesting to note that this general trend manifests itself throughout experiments conducted on high refractive index substrates. The decreased fluorescence exhibited by fluorescently labeled species is especially intriguing in light of Section 4.5.2.

4.5.2. Native Luminescence of TiO_2 and $SrTiO_3$

As it was attempted to amend TiO_2 and $SrTiO_3$ to use with total internal reflection, it became apparent that both substrates exhibited some native luminescence. This was first noted when total internal reflection was attempted using one of the substrates and a blank solution containing no fluorophore. A bright TIR spot with a "winged" pattern was visible (Figure 4.4). It was decided that the "winged" pattern was due to the intensity of the background luminescence. To determine the wavelength dependence of the native luminescence of the substrates, emission spectra were taken for each (Figure 4.5).

Figure 4.4 Total Internal Reflection on $SrTiO_3$.
TIR was performed on $SrTiO_3$ and also on TiO_2 (data not shown) without a fluorescent bilayer. An elliptical spot with a fringe pattern at its ends was seen. The appearance of TIR indicated that the substrate exhibited intrinsic luminescence.

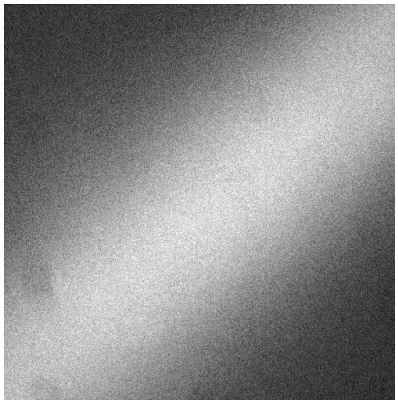

The emission spectra for both substrates were taken at excitation wavelengths of 400 nm, 488 nm, and 514 nm. The scans were taken over 420-800 nm, 495-800 nm, and 520-800 nm respectively. Excitation wavelengths were chosen because 488 nm and 514 nm excitation are the two most popular laser lines of the argon ion laser and 400 nm provides an overall view of the visible region. The emission spectra of $SrTiO_3$ provided some interesting information. Although its main emission peaks are situated at about 420 nm and 550 nm, $SrTiO_3$ has an extremely high overall luminescence intensity throughout the wavelength range scanned. This overall high

background luminescence seen in Figure 4.5a-c makes strontium titanate a bad candidate for use in the visible region. The emission spectra of TiO_2 provided more promising evidence. Although titanium dioxide also exhibits background luminescence, the intensity of this background luminescence is much less intense over the visible region (Figure 4.5d-f). Titanium dioxide exhibits a broad peak from about 400-510 nm. This broad peak complicates the use of the 488 nm line of the argon ion laser. However, it is conceivable (with further experimental controls) to use the 514 nm laser line. Consequently, all further experiments were conducted solely with TiO_2.

Figure 4.5 Fluorescence Emission of $SrTiO_3$ and TiO_2.

Parts a), b), and c) are of $SrTiO_3$. Parts d), e), and f) are of TiO_2. Parts a) and d) were excited at 400 nm and scanned from 420-800 nm. Parts b) and e) were excited at 488 nm and scanned from 495-800 nm. Parts c) and f) were excited at 514 nm and scanned from 520-800 nm. $SrTiO_3$ displays a much higher intensity background luminescence over the range scanned. $Ti0_2$ has a decreased background luminescence that makes the material more amendable to use with visible lasers.

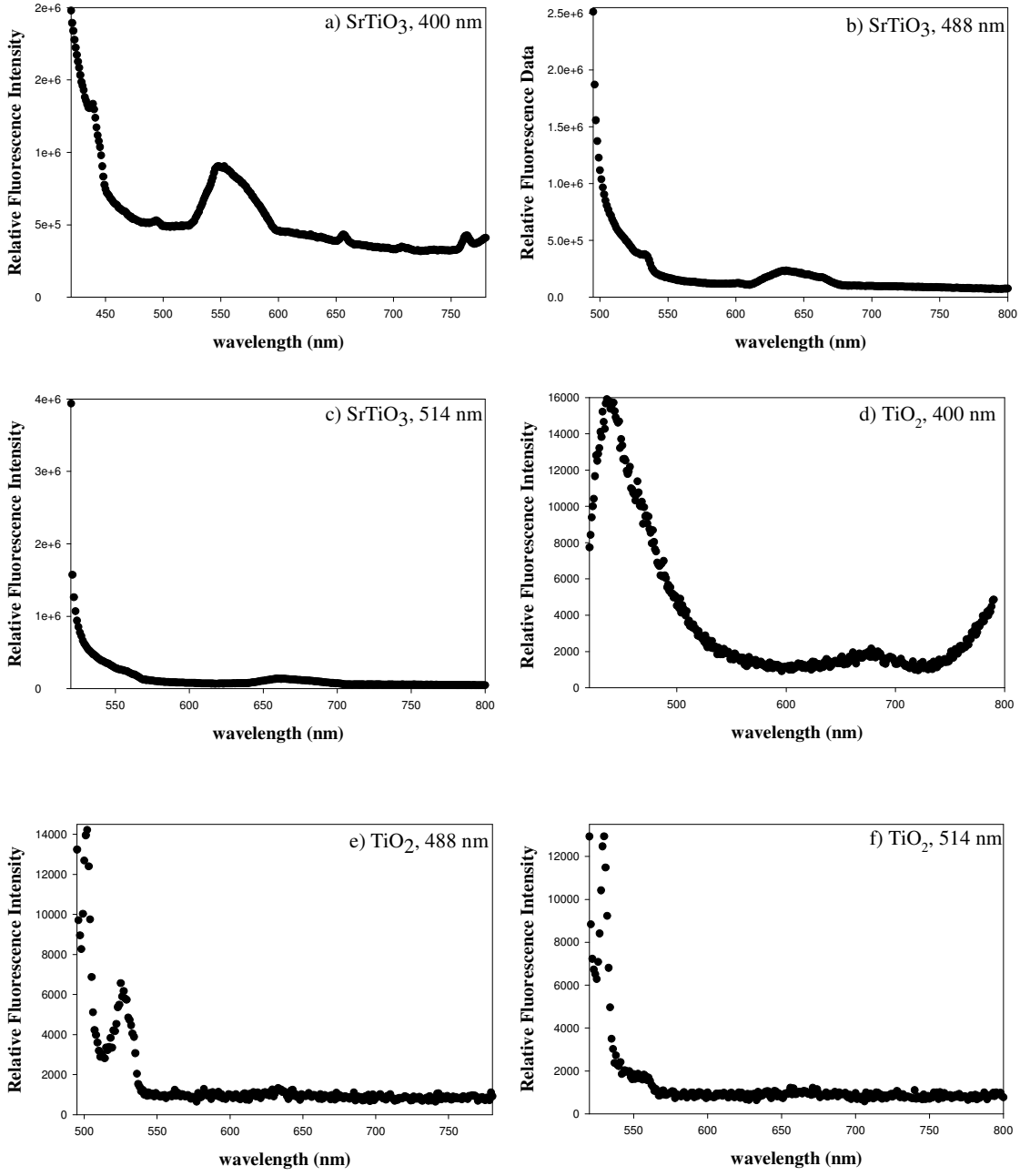

4.5.3 Fluorescent Antibody Experiments

Fluorescence intensity experiments were performed on titanium dioxide to determine at what concentration of fluorescently-labeled antibodies the intrinsic luminescence of the substrate is overcome. These fluorescence intensity experiments were performed on both the 488 nm and 514 nm laser lines of an argon ion laser (Figure 4.6) using IgG antibodies. Intensity data were taken for 300 seconds. An average intensity was calculated and all samples were corrected to the sample containing no antibody.

Figure 4.6a demonstrates that the background intensity effectively overwhelms the fluorescence of the dilute antibodies until about 80 nM on the 488 nm laser line. Although this concentration is still small, the use of high refractive index substrates is being developed for use with TIR-FCS. In TIR-FCS, the number of molecules in the observation volume, and consequently, the solution concentration must be small so that fluctuations in the fluorescent intensity can be seen. Most TIR-FCS measurements are taken below 100 nM, and therefore, it would be optimal to avoid approaching this upper limit. Figure 4.6b demonstrates much more promising results. The expected increase in fluorescence intensity should be linear as concentration increases, and that is what is seen here. The linearity indicates that the background luminescence of the substrate is much less with 514 nm excitation. Resultantly, all TIR-FCS studies were conducted on TiO_2 with 514 nm laser excitation. Furthermore, the concentration plot illustrated that a 30 nM IgG antibody solution was appropriate for these studies.

Figure 4.6 Fluorescence Intensity vs. Concentration Plots.
Fluorescence intensity experiments were performed to determine at what concentration the fluorescence from labeled IgG antibodies overcomes the intrinsic TiO_2 luminescence. a) With 488 nm excitation the fluorescence is swamped by the background signal until high concentrations. b) With 514 nm laser excitation a linear relationship between fluorescence intensity and concentration is seen at all concentrations.

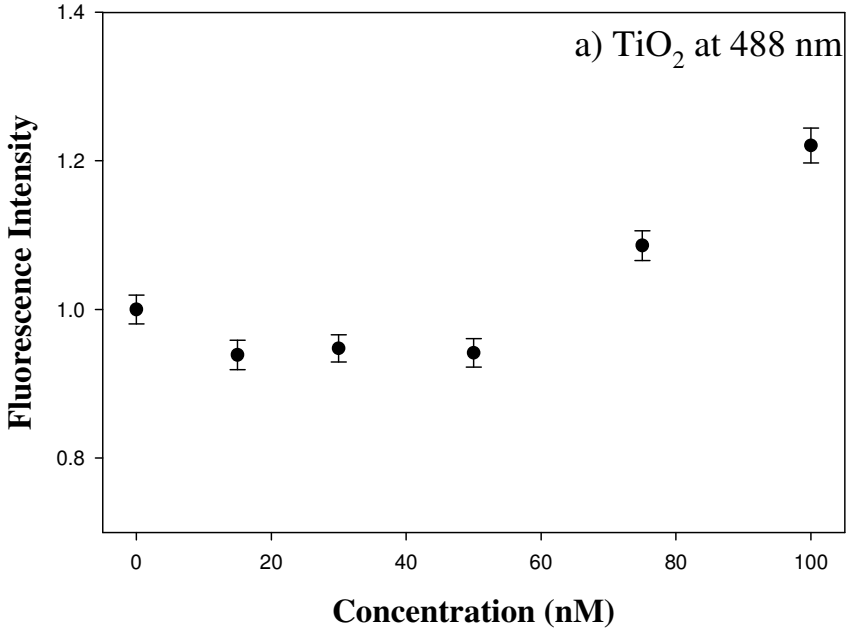

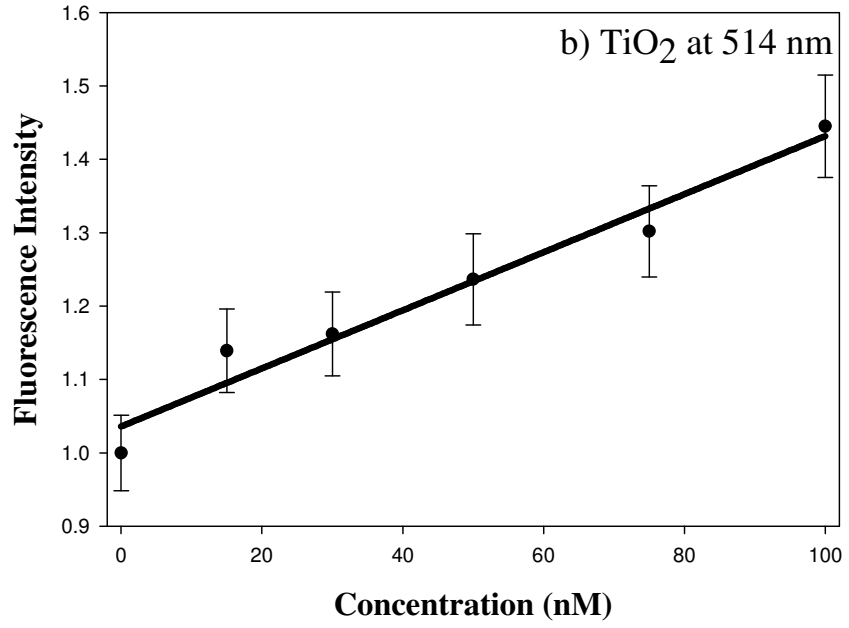

4.5.4 TIR-FCS

Total internal reflection with fluorescence correlation spectroscopy was performed on fluorescently-labeled IgG antibodies using a TiO_2 prism. The use of TiO_2 with TIR-FCS proved finicky during these experiments. Consequently, data were taken for longer periods of time and fit to a simplified autocorrelation function (Eq. 4.3). Figure 4.7 shows an autocorrelation function performed atop a TiO_2 prism. This particular autocorrelation function is an average of sixteen different experiments. The corresponding R_e for this curve is 25.44 ms^{-1} and N_e is 0.3267. In chapter two, the R_e value for IgG was determined at approximately 85 nm from the interface to be ~4.6 ms^{-1}. According to the theory set forth in chapter 2 (Eq. 2.9), the diffusion coefficient, $D(z)$, should decrease as a molecule approaches closer to the membrane. On the contrary, TiO_2 should produce a much smaller evanescent wave depth, d, and consequently, an extremely faster rate of diffusion, R_e. This increase in the rate of diffusion at smaller evanescent wave depths was demonstrated here. The incidence angle is unknown for the experiments using TiO_2 and consequently, the evanescent wave depth cannot be calibrated. However, by utilizing the rate of diffusion for IgG at 85 nm, an estimate of the R_e value for evanescent wave depths of 18-43 nm can be calculated. These estimated R_e values are 18 ms^{-1} to 102 ms^{-1}, respectively, which fit well with the R_e value calculated here. It should be noted, however, that these estimates ignore the possible hydrodynamic effect illustrated in chapter 2.

The next logical question to ask is how well the increase in R_e fits the hydrodynamic theory laid out in chapter 2. This can be deduced by comparing the theoretical values for the initial slope, S_e (Eq. 2.10), to the experimental R_e value obtained atop the TiO_2 prism. Theroretical values of S_e were generated at 18 nm, 35 nm, and 43 nm evanescent wave

depths for an IgG antibody. The theoretical values of S_e are 61.30 ms^{-1}, 20.39 ms^{-1}, and 14.32 ms^{-1}. An R_e value of 25.44 ms^{-1} fits well within this range. However, to fully ascertain the impact of the hydrodynamic surface effect a more comprehensive study must be performed at known evanescent wave depths.

As figure 4.7 illustrates, the data appear not to fit well to the autocorrelation function at times less than 0.1 ms. This noise prevents TiO_2 from being used to its full potential with TIR-FCS. Consequently, future experiments should concentrate on the origin of the noise. One plausible explanation is that a photochemical reaction is occurring on TiO_2. Such reactions would manifest themselves at these earlier times in the autocorrelation function. Once the nature of the noise has been addressed, emphasis can then be placed on a more comprehensive study of the hydrodynamic effect predicted near interfaces.

Figure 4.7 Representative Autocorrelation Function for Fluorescently Labeled IgG Antibodies atop a TiO_2 Prism.

An autocorrelation function obtained by TIR-FCS for 16 different experiments averaged together performed using 30 nM IgG antibodies. The best fits for this particular experiment to Eq. 4.3 were R_e = 25.44 ms^{-1} and N_e = 0.3267.

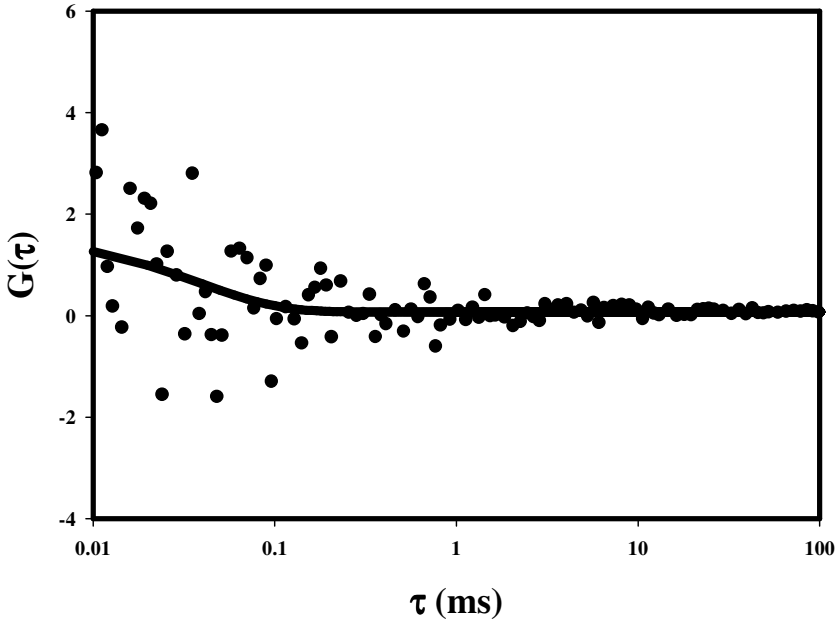

4.5.5 Quenching Phenomenon

Serendipitously, in one day of experiments, the vesicles were mistakenly not tip sonicated. This prevented unilamellar vesicles from forming, and no bilayer was adsorbed onto the surface. Experiments identical to those in Section 4.5.3 were performed where increasingly high concentrations of fluorescently-labeled IgG were placed in the sample chamber between the prism and coverslip. Remarkably, in the absence of a bilayer, increasing the concentration of the antibody caused a linear decrease in the fluorescence (data not shown). This quenching phenomenon that is responsive to increasing the concentration is noteworthy for two reasons. Primarily, during the fluorescence imaging experiments (Section 4.5.1) the high refractive index substrates produced lower fluorescence intensity than SiO_2. It is plausible to deduce that the decreased fluorescence from the bilayers during the imaging experiments is related to the decreased fluorescence with increasing antibody concentration seen here. Secondly, TiO_2 is natively luminescent and so a decrease in fluorescence intensity under this situation is unexpected. It is possible that a FRET-like scenario is occurring between the substrate and fluorescent material very near to it. Further experiments are required to deduce the nature of this quenching phenomenon.

4.6 Discussion

The purpose of these experiments was to experimentally pioneer the use of $SrTiO_3$ and TiO_2 as total internal reflection elements. The first step in accomplishing this was to reconfirm that phospholipid bilayers can be formed atop these two substrates. This was accomplished as demonstrated in Section 4.5.1. The second step in amending $SrTiO_3$ and TiO_2 to use with TIR technologies was to prove that TIR can be accomplished through these prisms. TIR was created using these two substrates, and an autocorrelation function was

obtained by TIR-FCS for TiO_2. However, more work is required in this area so that the data obtained from total internal reflection atop a TiO_2 substrate can be fit to any autocorrelation function and not just simplified versions of the appropriate autocorrelation function. The success achieved thus far in this area provides ample evidence indicating that TiO_2 can be used in total internal reflection.

One obstacle that must be addressed is the high background luminescence exhibited by these substrates. The extremely high background luminescence of $SrTiO_3$ eliminated the possibilities for its use with TIR-FCS, and all efforts were focused on TiO_2. Although TiO_2 exhibited significantly less background luminescence, it is still considerably natively luminescent. This native luminescence is much less a deterrent to obtaining data at 514 nm light. Noisy autocorrelation functions were obtained at this wavelength by utilizing a simplified version of the appropriate autocorrelation function and by taking data at longer times.

Future investigations must also address the quenching phenomenon that has been observed. At high concentrations of fluorophore, it is not uncommon to see self-quenching or self-absorption present in fluorescence data that would cause a negative deviation from linearity in intensity vs. concentration plots (Skoog *et al.*, 1998). Although concentrations in the nanomolar range are not considered high, the lack of a bilayer increases the propensity for nonspecific adsorption which would cause a high surface concentration. Alternatively, perhaps the high background luminescence of the substrate is enough to cause self-quenching or self-absorption. Right now there is not enough evidence to conclusively say if it is self-quenching, self-absorption, a photochemical process, or a FRET-like substrate-fluorophore

interaction. It is clear that if more knowledge is obtained about the luminescent activity seen on TiO_2, this information might provide an avenue around these experimental complications.

Future studies in this area should concentrate on several important points. First of all, with TiO_2, the argon ion laser might not be the most appropriate laser choice. Although there is significantly less background luminescence at 514 nm (Figure 4.5b), moving to a higher wavelength in the visible region might provide better results. Potentially useful lasers in include the Nd:YAG laser (532 nm line) or a Krypton-Argon laser (568 nm or 647 nm laser line).

Secondly, the possibility of a photochemical reaction occurring on TiO_2 can be addressed by taking intensity dependent measurements. The possibility of a photochemical interaction occurring is plausible because the data does not fit well to Eq. 4.3 at fast times (less than 0.1 ms). This is the time scale where one would expect to see a photochemical interaction manifest itself. By doubling the laser intensity, obtaining TIR-FCS data, and monitoring the rate of diffusion one could probe this scenario. The rate of diffusion is not intensity dependent, and so large changes in the calculated R_e at high intensity would indicate that a photochemical reaction is occurring.

Another approach in determining the problems associated with using TiO_2 with TIR-FCS would be to choose a different antibody (with a different radius) to study or change the angle at which the laser is incident on the prism. Both of these situations should produce different R_e values according to the theory laid out in chapter 2. The values obtained by these experiments would provide insight into the rates of diffusion already measured and if the substrates are accurately measuring the rate of diffusion.

In conclusion, TiO_2 was proven to be utilizable in TIR-FCS measurements and total internal reflection based techniques. Future experiments are required before TiO_2 can be successfully applied in a research study involving TIR-FCS. These investigations should concentrate on eliminating the noise seen in the autocorrelated data. It has also been experimentally verified that phospholipid bilayers can be formed on these substrates. These experiments should provide a foundation for future applications in this area.

Chapter 5 Summary and Future Directions

This compilation of work represents advancements in both theory and methodology. These advancements have application mainly in the field of biophysics, but contributions will be felt elsewhere. Chapter 2 represents a theoretical and experimental study that demonstrates that the theory regarding ligand-receptor interactions near model membranes should be amended to include an increasing frictional force acting upon the molecules as they approach the membrane. This experimental proof will most likely see the widest application from this body of work, because membranes are the site of a plethora of ligand-receptor type interactions, and they govern many inherently important processes.

Since the publication of Chapter 2 new ideas have surfaced about possible further investigations into how the membrane affects translational mobility. Originally, the hope in working with high refractive index substrates was that they would provide an additional study of this manner. By combining high refractive index substrates with VA-TIR, depth profiling experiments can be accomplished. However, additional studies are required before this line of logic can be brought to fruition. Another possible approach would be to investigate how altering solution viscosity changes diffusion near model membranes. A study published in 2000 examined the rebinding of IgE Fab fragment antibodies at model membranes when increasing the glycerol concentration (Lagerholm *et al.*, 2000). By sequentially increasing the amount of glycerol, two things happen in a total internal reflection experiment (Table 5.1). Primarily, the solution becomes increasingly viscous thus increasing the frictional coefficient. The increase in the frictional coefficient causes a decrease in

translational mobility similar to that seen as the molecule approaches the membrane. Secondly and perhaps more interesting, the increasing glycerol solution causes an increase in the refractive index of the buffer solution. The increase in the refractive index of the buffer solution elicits an affect similar to that seen with high refractive index substrates; it causes a change in the critical angle and subsequently alters the evanescent wave depth.

Table 5.1 Relationship Between Glycerol Addition and Solution Viscosity[a].

Volume Fraction of glycerol (v)	**0**	**25**	**35**
Viscosity (theory) (g/cm s) x 10^2	1.002	2.404	3.714
Viscosity (expt) (g/cm s) x 10^2	0.95 ± 0.01	2.29 ± 0.03	3.68 ± 0.02
Refractive index $n_2(v)$	1.334	1.370	1.385
Critical angle α_c (deg)	65.4	69.0	70.7
Evanescent depth d (nm)	70.0	84.7	94.5

[a] Table is a partial reproduction of Table 3 from Lagerholm *et al.*, 2000.

An examination of the relationship between translational mobility and viscosity could be accomplished by performing TIR-FCS on the original five unaltered antibodies from chapter 2 (IgM, IgA, IgG, IgG $(Fab')_2$, and IgG Fab). The data would then be fit to Eq. 2.10 which is the equation for the initial slope of autocorrelation function for a sample displaying spatially dependent diffusion. In Chapter 2 the initial slope, S_e, was corrected by antibody radius, r, to correct for contributions from the Stokes-Einstein Equation. In this case, S_e should be corrected by viscosity, η, to correct for similar contributions. Theoretical curves have been prepared for the five antibody types at the three viscosities (glycerol additions) listed in Table 5.1 (Figure 5.1).

Figure 5.1 Theoretical Plots of ηS_e vs. η.
The five unaltered antibody types from chapter 2 (IgM, IgA, IgG, IgG (Fab')$_2$, and IgG Fab) were fit to equation 2.10 plus a correction for η. The data were plotted at the three viscosity values from Table 5.1. Lines represent IgM (red), IgA (pink), IgG (blue), IgG (Fab')$_2$ (green), and IgG Fab (yellow).

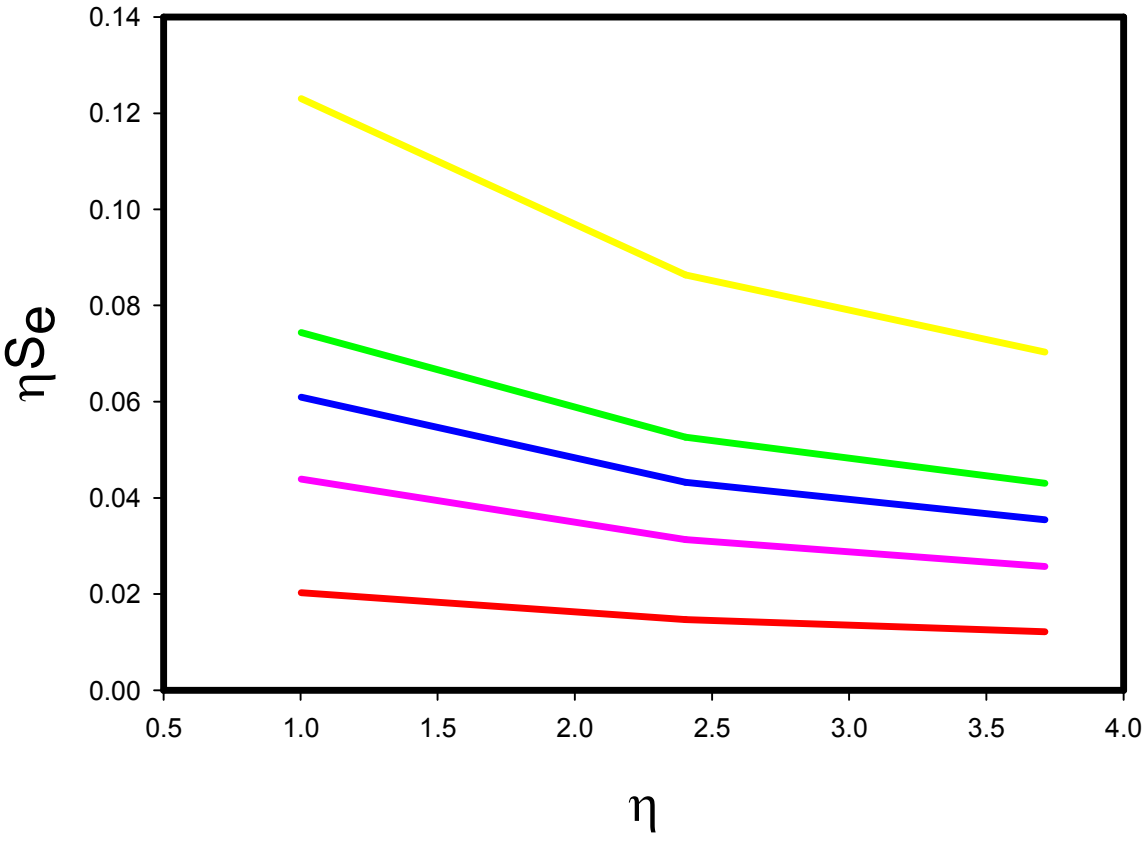

A study of this nature would be beneficial for many reasons. Primarily, the data in Chapter 2 (Figure 2.5) is a bit noisier than one would hope. The noise was evident due to day to day variability in the evanescent wave depth which was increased due to the amount of time it took to study nine antibody types and also due to evanescent wave depth at which the measurements were taken. The data in Chapter 2 were taken approximately 85 nm from the membrane, and the size dependence of diffusion should not be as strong here as it would be closer to the membrane. Although a definite trend was established in Chapter 2, a second study confirming the results would increase its impact. Furthermore, the viscosity experiments could possibly require less time than the original experiments in Chapter 2 as

there are less sample points and as the researcher has grown more advanced in the use of TIR-FCS. Consequently, this shorter time period should correlate to less variability in the evanescent wave depth.

Another experimental possibility that has manifested itself is to study the diffusion of ligands near model membranes at a different ionic strength. The experiments conducted in Chapter 2 were performed at a high ionic strength (50 mM sodium phosphate with 150 mM NaCl). It would be interesting to perform TIR-FCS on fluorescently labeled antibodies and record the rate of diffusion as a function of antibody radius in a solution of low ionic strength. Originally, the set of experiments that laid the background for the work accomplished in Chapter 2 measured the diffusion of fluorescently labeled IgG near a planar model membrane. These studies found that IgG diffusion was faster at low ionic strength and slower at high ionic strength (Starr and Thompson, 2002). These experiments also found that diffusion showed no dependence upon solution pH negating the hypothesis that the decreased diffusion at high ionic strengths is due to electrostatic interactions. It is also interesting to note that in bulk solution diffusion only demonstrates an ionic strength dependence at extremely high protein concentrations (~10 mg/mL). This provides further indication that the decreased diffusion is a hydrodynamic effect impacted by the close proximity of the model membrane. A next logical step would be to combine these two pieces of evidence. Further information would be gained about the nature of this effect if the decreased diffusion near model membranes was probed at low ionic strength in a systematic controlled approach.

It is still anticipated that a depth profiling study be initiated using high refractive index substrates. However, before this can be done TiO_2 must be optimized for use with TIR

technologies. This requires a systematic study of the native luminescence exhibited by titanium dioxide and also the quenching effect demonstrated by the prism. Other possible approaches were outlined in Chapter 4. They include utilizing the TiO_2 prism on a different laser with a higher excitation wavelength. This could possibly help minimize the native luminescence. The possibilities of a photochemical reaction causing artifacts in the autocorrelation function can be probed by conducting TIR-FCS in a similar manner to that done in chapter 4 while using a higher incident power. Then a systematic comparison of the data at the two incident powers will reveal any photochemical effects. Finally, once these issues have been addressed, TIR-FCS should be performed on TiO_2 using different antibodies and at different incidence angles.

In Chapter 3 the homogeneity and continuity of a stacked bilayer developed by our lab was probed. The fluorescence and atomic force microscopy experiments demonstrated that the technology is ready to be applied to various problems including multilayer applications, and possibly as a cushioning system. Before each new application is attempted, it must be validated that the stacked bilayer can be applied. For instance, for the stacked bilayer to be applied in multilayer applications it would be worthwhile to perform light scattering experiments on the system and compare them to similar measurements already accomplished on other multilayer construction techniques. This would be interesting because it would indicate if the stacked bilayer system can elicit the same increase in signal seen in other multilayers. Also, if the stacked bilayer is to be used to incorporate a transmembrane protein, many more studies must be conducted to see why there exists an inherent difficulty in inserting transmembrane proteins into bilayers while maintaining their lateral mobility. Finally, if the stacked bilayer is to be applied to a situation where surface roughness is an

issue and a more fluid bilayer is required, tests must be performed that validate that the stacked bilayer decreases surface roughness.

APPENDIX: TIR-FCS AUTOCORRELATION FUNCTION FOR SPATIALLY DEPENDENT DIFFUSION

As described previously (Starr and Thompson, 2001)

$$\frac{G_e(\tau)}{G_e(0)} = \frac{2}{< A > d} \int_0^\infty dz' \exp(-\frac{z'}{d}) \int_0^\infty dz \exp(-\frac{z}{d}) \varphi(z, z', \tau) \tag{A1}$$

where $\varphi(z,z',\tau)$ denotes the concentration fluctuation autocorrelation function; i.e.,

$$\varphi(z, z', \tau) =< \delta A(z, \tau) \delta A(z', 0) > \tag{A2}$$

$A(z,\tau)$ is the concentration at position z and time τ, $<A>$ is the average concentration, and $\delta A(z,\tau) = A(z,\tau) - <A>$ is the concentration fluctuation at position z and time τ. The partial differential equation describing the behavior of $\varphi(z,z',\tau)$, for spatially dependent diffusion, is (Bevan and Prieve, 2000)

$$\frac{\partial}{\partial \tau} \varphi(z, z', \tau) = \frac{\partial}{\partial z} [D(z) \frac{\partial}{\partial z} \varphi(z, z', \tau)] \tag{A3}$$

The boundary conditions are

$$\begin{aligned} &[\varphi(z, z', \tau)]_{z=\infty} = 0 \\ &[\frac{\partial}{\partial z} \varphi(z, z', \tau)]_{z=0} = 0 \end{aligned} \tag{A4}$$

and the initial condition is

$$[\varphi(z, z', \tau)]_{\tau=0} =< A > \delta(z - z') \tag{A5}$$

where $\delta(z-z')$ is a Dirac delta function. Using Eq. A5 in Eq. A1 shows that $[G_e(\tau)/G_e(0)]_{\tau=0} = 1$. We calculate the initial slope as (see Eqs. 10, A1 and A3)

$$S_e = \frac{2}{< A > d}\left\{\int_0^\infty dz' \exp(-\frac{z'}{d})\int_0^\infty dz \exp(-\frac{z}{d})[\frac{\partial}{\partial z}[D(z)\frac{\partial}{\partial z}\varphi(z,z',\tau)]\right\}_{\tau=0} \quad \text{(A6)}$$

Evaluating the integral over the variable z by parts (twice) and using the condition that D(0) = 0 implies that

$$S_e = \frac{2}{< A > d^2}\left\{\int_0^\infty dz' \exp(-\frac{z'}{d})\int_0^\infty dz \exp(-\frac{z}{d})[\frac{1}{d}D(z) - \frac{d}{dz}D(z)]\varphi(z,z',\tau)\right\}_{\tau=0} \quad \text{(A7)}$$

By using Eq. A5, one finds that

$$S_e = \frac{2}{d^2}\int_0^\infty dz' \exp(-\frac{2z'}{d})[\frac{1}{d}D(z') - \frac{d}{dz'}D(z')] \quad \text{(A8)}$$

Evaluating the second integral by parts yields

$$S_e = \frac{2}{d^3}\int_0^\infty \exp(-\frac{2z'}{d})D(z')dz' \quad \text{(A9)}$$

Eq. A9 with Eq. 6 implies Eq. 10.

REFERENCES

Abramowitz, M., and Stegun, I. *Handbook of Mathematical Functions,* Dover Publications, New York, 1968. pp 297-329.

Ajo-Franklin, C.M., Kam, L., and Boxer, S.G. 2001. High refractive index substrates for fluorescence microscopy of biological interfaces with high z contrast. *Proc. Natl. Acad. Sci. USA.* 98:13643-13648.

Allen, N.W., and Thompson, N.L. 2006 Ligand binding by estrogen receptor beta attached to nanospheres measured by fluorescence correlation spectroscopy. *Cytometry A.* 69A:524-532.

Amenitsch, H., Rappolt, M., Teixeira, C.V., Majerowicz, M., and Laggner, P. 2004. In situ sensing of salinity in oriented lipid multilayers by surface x-ray scattering. *Langmuir*. 20:4621-4628.

Anderson, T.G., and McConnell, H.M.1999. Interpretation of biophasic dissociation kinetics for isometric class II major histocompatibility complex-peptide complexes. *Biophys. J.* 77:2451-2461.

Armstrong, J.K., Wenby, R.B, Meiselman, H.J., and Fischer, T.C. 2004. The hydrodynamic radii of macromolecules and their effect on red blood cell aggregation. *Biophys. J.* 87::4259-4270.

Beretta, S., Chirico, G., and Baldini, G. 2000. Short-range interactions of globular proteins at high ionic strengths. *Macromolecules.* 33:8663-8670.

Berquand, A., Mazeran, P.E., Pantigny, J., Proux-Delrouye, V., Laval, J.M., and Bourdillon, C. 2003. Two-step formation of streptavidin-supported lipid bilayers by PEG-triggered vesicle fusion. Fluorescence and atomic force microscopy characterization. *Langmuir.* 19:1700-1707.

Bevan, M.A., and Prieve, D.C. 2000. Hindered diffusion of colloidal particles very near to a wall. *J. Chem. Phys.* 113:1228-1236.

Binnig, G., and Quate, C.F. 1986. Atomic force microscopy. *Phys. Rev. Lett.* 56:930-933.

Bowen, W.R., Liang, Y.C., and Williams, P.M. 2000. Gradient diffusion coefficients – theory and experiment. *Chem Eng. Sci.* 55:2359-2377.

Brenner, H. 1961. The slow motion of a sphere through a viscous fluid towards a plane surface. *Chem. Eng. Sci.* 16:242-251.

Brian, A.A., and McConnell, H.M. 1984. Allogenic stimulation of cytotoxic T cells by supported planar membranes. *Proc. Natl. Acad. Sci. USA.* 81:6159-6163.

Burghardt, T.P., and Thompson, N.L. 1984. Effect of planar dielectric interfaces on fluorescence emission and detection. *Biophys. J.* 46:729-737.

Butt, H. and Jaschke, M. 1995. Calculation of thermal noise in atomic-force microscopy. *Nanotech.* 6:1-7.

Chiruvolu, S., Walker, S., Isrealachvili, J., Schmitt, F.-J., Leckband, D., and Zasadzinski, J.A., 1994. Higher order self-assembly of vesicles by site-specific binding. *Science.* 264:1753-1756.

Domagala, T., Konstantopoulos, N., Jorissen, R.N., Fabri, L., Geleick, D., Lax, I., Schlessinger, J., Sawyer, W., Howlett, G.F., Burgess, A.W., and Nice, E.C. 2000. Stoichiometry, kinetic and binding analysis of the interaction between epidermal growth factor (EGF) and the extracellular domain of the EGF receptor. *Growth Factors.* 18:11-29.

Dufresne, E.R., Squires, T.M., Brenner, M.P., and Grier, D.G. 2000. Hydrodynamic coupling of two Brownian spheres to a planar surface. *Phys. Rev. Lett.* 85:3317-3320.

Edidin, M. 2003.The state of lipid rafts: from model membranes to cells. *Ann. Rev. Biophys. Biomol. Struct.* 32:257-283.

Edmiston, P.L., and Saavedra, S.S. 1998. Molecular orientation distributions in protein flims. 4. A multilayer composed of yeast cytochrome *c* bound through an intermediate streptavidin layer to a planar supported phospholipid bilayers. *J. Am. Chem. Soc.* 120:1665-1671.

Elson, E.L., Magde, D. 1974. Fluorescence correlation spectroscopy. I. conceptual basis and theory. *Biopolymers.* 13:1-27.

Elson, E.L. 1985. Fluorescence correlation spectroscopy and photobleaching recovery. *Ann. Rev. Phys. Chem.* 36:379-406.

Enderlein, J., Gregor, I., Patra, D., and Fitter, J., 2004. Art and artifacts of fluorescence correlation spectroscopy, *Curr. Pharm. Biotech.* 5:155-161.

Forsten, K.E., and Lauffenburger, D.A. 1994. Probability of autocrine ligard capture by cell surface receptors: implications for ligard secretion measurements. *J. Comput. Bio.* 1:15-23.

Fradin, C., Abu-Arish, A., Granek, R., and Elbaum, M. 2003. Fluorescence correlation spectroscopy close to a fluctuating membrane. *Biophys. J.*84:2005-2020.

Frauenfelder, H., Sligar, S.G., and Wolynes, P.G. 1991. The energy landscapes and motions on proteins. *Science*. 254:1598-1603.

Frej, N.A., and Prieve, D.C. 1993. Hindered diffusion of a single sphere very near a wall in a nonuniform force field. *J. Chem. Phys.* 98:7552-7564.

Frieden, C., Chattopadhyay, K., and Elson, E.L. 2002. What fluorescence correlation spectroscopy can tell us about unfolded proteins. *Adv. Protein Chem.* 62:91-109.

Gaigalas, A.K., Hubbard, J.B., McCurley, M., and Woo, S. 1992. Diffusiion of bovine serum albumin in aqueous solutions. *J. Phys. Chem.* 96:2355-2359.

Gösch, M., and Rigler, R. 2005. Fluorescence correlation spectroscopy of molecular motions and kinetics. *Adv. Drug Deliv. Rev.* 57:169-190.

Grigsby, J.J., Blanch, H.W., and Prausnitz, J.M. 2000. Diffusion of lysozyme in acqueous McCl.2. solutions from dynamic light scattering data: effect of protein and salt concentrations. *J. Phys. Chem. B.* 104:3645-3650.

Hansen, R.L., and Harris, J.M. 1998a. Total internal reflection fluorescence correlation spectroscopy for counting molecules at solid/liquid interfaces. *Anal. Chem.* 70:2565-2575.

Hansen, R.L., and Harris, J.M. 1998b. Measuring reversible adsorption kinetics of small molecules at solid/liquid interfaces by total internal reflection correlation spectroscopy. *Anal. Chem.* 70:4247-4256.

Harlepp, S., Robert, J., Darnton, N.C., and Chatenay,D. 2004. Subnanometric measurements of evanescent wave penetration depth using total internal reflection microscopy combined with fluorescence correlation spectroscopy. *Appl. Phys. Lett.* 85:3917-3919.

Hassler, K., Anhut, T., Rigler, R,, Gosch, M., and Lasser, T. 2005. High count rates with total internal reflection fluorescence correlation spectroscopy. *Biophys.* 88:L01-3.

Haustein, E., and Schwille, P. 2004. Single-molecule spectroscopic methods, *Curr. Opin. Struct. Biol.* 14:531-534.

Hillesheim, L.N., and Muller, J.D. 2005. Photo-detector effects on the photon counting histogram. *Biophys. J.* 89:3491-3507.

Hink, M.A., Borst, J.W., and Visser, A.J.W.G. 2003. Fluorescence correlation spectroscopy of GFP fusion proteins in living plant cells. *Meth. Enzymol.* 361:93-112.

Hirschfeld T., and Block M.J. 1977. Virometer: real time virus detection and identification in biological fluids. *Opt. Eng.* 16:406-407.

Hirschfeld T., Block M.J., and Mueller, W. 1977. Virometer: an optical instrument for visual observation, measurement, and classification of free viruses. *J. Histochem. Cytochem.* 25:719-723.

Holt, M., Cooke, A., Neef, A., and Lagnado, L. 2004. High mobility of vesicles supports continuous exocytosis at a ribbon synapse. *Curr. Bio.* 153:177-190.

Hsieh, H.V., and Thompson, N.L. 1995. Dissociation kinetics between a mouse Fc receptor (FcyRII) and IgG: measurement by total internal reflection with fluorescence photobleaching recovery. *J. Biol. Chem.* 34:12481-12488.

Huang, L. 1985. Incorporation of acylated antibody into planar lipid multilayers: Characterization and cell binding. *Biochem.* 24:29-34.

Johns, L.M., Levitan, E.S., Shelden, E.A., Holtz, R.W., and Axelrod, D. 2001. Restriction of secretory granule motion near the plasma membrane of chromaffin cells. *J. Cell Bio.* 153:177-190.

Kaasgaard, T., Mouritsen, O.G., and Jorgensen, K. 2002. Lipid domain formation and ligand-receptor distribution in lipid bilayer membranes investigated by atomic force microscopy. *FEBS Lett.* 515:29-34.

Kahya, N., Scherfeld, D., Bacia, K., and Schwille, P. 2004. Lipid domain formation and dynamics in giant unilamellar vesicles explored by fluorescence correlation spectroscopy. *J. Struct. Bio.* 147:77-89.

Kalb, E., Frey, S., and Tamm, L.K. 1992. Formation of supported planar bilayers by fusion of vesicles to supported phospholipid monolayers. *Biochim. Biophys. Acta.* 1103:307-316.

Kask, P.: Palo K. Introduction to the theory of fluorescence intensity distribution analysis. In *Fluorescence Coeewlation Spectroscopy: Theory and Applications,* Rigler, R., Elson, E.I., Eds. Springer-Verlag: Berlin, 2001. pp 438-458.

Kim, J.H., Huganir, R.L. 1999. Organization and regulation of proteins at synapses. *Curr. Opin. Cell Biol.* 1999. 11:248-254.

Kopelman, R. 1988. Fractal Reaction Kinetics. *Science*. 241:1620-1626.

Kuehner,D.E., Heyer, C., Ramsch, C., Fornfeld, U.M., Blanch, H.W., and Prausnitz, J.M. 1997. Interactions of lysozyme in concentrated electrolyte solutions from dynamic light-scattering measurements. *Biophys. J.* 73:3211-3224.

Kühner, M., Tampé, R., and Sackmann, E. 1994. Lipid mono- and bilayer supported on polymer films: composite polymer-lipid films on solid substrates. *Biophys. J.* 67:217-226.

Kurrat, R., Textor, M., Ramsden, J.J., Boni, P., Spencer, N.D. 1997. Instrumental improvements in optical waveguide light mode spectroscopy for the study of biomolecule adsorption. *Rev. Sci. Instrum.* 68:2172-2176.

Lagerholm, B.C., and Thompson, N.L.1998. Theory for ligand rebinding at cell membrane surfaces. *Biophys. J.* 74:1215-1228

Lagerholm, B.C., Starr, T.E., Volovyk, Z.N., and Thompson. N.L. 2000. Rebinding of IgE fabs at haptenated planar membranes: measurement by total internal reflection with fluorescence photobleaching recovery. *Biochemistry*. 39:2042-2051.

.Lagerholm, B.C., Weinreb, G.E., Jacobson, K., and Thompson, N.L. 2005. Detecting microdomains in intact cell membranes. *Ann. Rev. Phys. Chem.* 56:309-336.

Lanteri, N., Rolandi, R., Cavatorta, P., Polverini, E., Riccio, P., and Gliozzi, A. 2000. Myelin basic protein-lipid complex: an atomic force microscopy study. *Coll. Surf. A.* 175:3-9.

Lauffenburger, D.A.: Lindermann, J.J. *Receptors: Models for Binding, Trafficking, and Signaling. Oxford University Press. Oxford, 1993.*

Le Bon, C., Nicolai, T., Kuil, M.E., and Hollander, J.G. 1999. Self-diffusion and cooperative diffusion of globular proteins in solution. *J. Phys. Chem. B.* 103:10294-10299.

Lee, B. 2003. Review of the present status of optical fiber sensors. *Opt. Fiber Technol.* 9:57-79.

Lehr, H.P., Reimann, M., Brandenburg, A., Sulz, G., and Klapproth, H. 2003. Real-time detection of nucleic acid interactions by total internal reflection fluorescence. *Anal. Chem.* 75:2414-2420.

Levin, M.D., Shimizu, T.S., and Bray, D. 2002. Binding and diffusion of CheR molecules within a cluster of membrane receptors. *Biophys. J.* 74:1215-1228.

Levin, M.K., and Carson, J.H. 2004. Fluorescence correlation spectroscopy and quantitative cell biology. *Different.* 72:1-10.

Liebmann, L.W., Robinson, J.A., Mann, K.G. 1991. A dual beam total internal reflection fluorescence spectrometer for dynamic depth resolved measurements of biochemical liquid-solid interface binding reactions in opaque solvents. *Rev. Sci. Instrum.* 62:2083-2092.

Lieto, A.M. 2003. Membrane dynamics measured by total internal reflection with fluorescence correlation spectroscopy. *PhD Thesis*, University of North Carolina at Chapel Hill.

Lieto, A.M., Cush, R.C., and Thompson, N.L. 2003. Ligand-receptor kinetics measured by total internal reflection with fluorescence correlation spectroscopy. *Biophys. J.* 85:3294-3302.

Lieto, A.M., and Thompson, N.L. 2004. Total internal reflection correlation spectroscopy: nonfluorescence competitors. *Biophys. J.* 87:1268-1278.

Lin, B., Yu, J., and Rice, S.A. 2000. Direct measurements of constrained Brownian motion of an isolated sphere between two walls. *Phys. Rev. E.* 62:3909-3919.

Livnah, O., Bayer, E.A., Wilchek, M., and Sussman, J.L. 1993. Three-dimensional structures of avidin and the avidin-biotin complex. *Proc. Natl. Acad. Sci. USA*. 90:5076-5080.

Mashanov, G.I., Tacon, D., Peckman, M., and Molloy, J.E. 2004. The spatial and temporal dynamics of pleckstrin homology domain binding at the plasma membrane measured by imaging single molecules in live mouse myoplasts. *J. Biol. Chem*.279:15274-15280.

McCain, K.S., and Harris, J.M. 2003. Total internal reflection fluorescence –correlation spectroscopy study of molecular transport in thin silica sol-gel films. 75:3616-3624.

McCain, K.S., Schuesche, P., and Harris, J.M. 2004a. Modifying the adsorption behavior of polyamidoamine dendrimes at silica surfaces investigated by total internal reflection correlation spectroscopy. *Anal. Chem.* 76:930-938.

McCain, K.S., Schuesche, P., and Harris, J.M. 2004b. Poly(amidoamine) dendrimers as nanoscale diffusion probes in sol-gel films investigated by total internal reflection spectroscopy. *Anal. Chem.* 76:939-946.

McKiernan, A.E., MacDonald, R.I., MacDonald, R.C., and Axelrod, D. 1997. Cytoskeletal protein binding kinetics at planar phospholipid membranes. *Biophys. J.* 73:1987-1998.

Muller, J.D., Chen, Y., and Gratton, E. 2003. Fluorescence correlation spectroscopy, *Meth. Enzymol.* 361: 69.

Murray, D., and Honig, B. 2002. Electrostatic control of the membrane targeting C2 domains. *Molecular Cell.* 9:145-154.

Naumann, C.A., Prucker, O., Lehmann, T., Rühe, J., Knoll, W., and Frank, C.W. 2002. The polymer-supported phospholipid bilayer: tethering as a new approach to substrate-membrane stabilization. *Biomacromolec.* 3:27-35.

Oetama, R.J., and Walz, J.Y. 2005. A new approach for analyzing particle motion near an interface using total internal reflection microscopy. *J. Colloid Interface Sci.* 284:323-331.

Pagac, E.S., Tilton, R.D., and Prieve, D.C. 1996. Hindered mobility of a rigid sphere near a wall. *Chem. Eng. Comm.* 148:105-122.

Payne, M.A., Igo, J.D., Cao, Z.H., Foster, S.B., Newton, S.M., and Klebba, T.E. 1997. Biphasic binding kinetics between FepA and its ligands. *J. Biol. Chem.* 272:21950-21955.

Pearce, K.H. 1993. Investigation of the Ca^{2+} -dependent lipid-binding properties of prothrombin and its fragment 1: Applications using total internal reflection fluorescence microscopy. *PhD Thesis*, University of North Carolina at Chapel Hill.

Pero, J.K., Haas, E.M., and Thompson, N.L. 2006 Size Dependence of Protein Diffusion Very Close to Membrane Surfaces: Measurement by Total Internal Reflection with Fluorescence Correlation Spectroscopy *J. Phys. Chem. B.* 110:10910-10918.

Poglitsch, C.L., and Thompson, N.L. 1990. Interaction of IgG with Fc receptors in substrate-supported planar membranes measured by total internal reflection fluorescence microscopy. *Biophys. J.* 57:A292.

Pompeo, G., Girasole, M., Cricenti, a., Cattaruzza, F., Flamini, A., Prosperi, T., Generosi, J., and Congiu Castellano, A. 2005. AFM characterization of solid-supported lipid multilayers prepared by spin coating. *Biochim et Biophys Acta.* 1712:29-36.

Pralle, A., Florin, E.L., Stelzer, E.H.K., and Horber, J.K.H. 1998. Photonic force microccope calibration by thermal noise analysis. *Appl. Phys. A Mater.* 66:S75-S71.

Pramanik, A. 2004. Ligand-receptor interactions in live cells by fluorescence correlation spectroscopy, *Curr. Pharm. Biotech.* 5:205.

Proux-Delrouye, V. Elie, C., Laval, J.M, Moiroux, J., and Bourdillon, C. 2002. Formation of tethered and streptavidin-supported lipid bilayers on a microporous electrode for the reconstitution of membranes of large surface area. *Langmuir*. 18:3263-3272.

Ravetch, J.V., and Bolland, S. 2001. *IGG FC receptors.* 19:275-290.

Reichert, W.M., Suci, P.A., Ives, J.T., and Andrade, J.D. 1987. Evanescent detection of adsorbed protein concentration distance profiles: fit of simple models to variable-angle total internal reflection fluorescence data. *Appl. Spec.* 41:503-508.

Reimhult, R. Höök, F., and Kasemo, B. 2003. Intact vesicle adsorption and supported biomembrane formation from vesicles in solution: influence of surface chemistry, vesicle size, temperature, and osmotic pressure. *Langmuir.* 19:1681-1691.

Richter, R.P., Bérat, R., and Brisson, A. 2006. Formation of solid-supported lipid bilayers: an integrated view. *Langmuir.* 22:3497-3505.

Rigler, R., and Elson, E.L. *Fluorescence Correlation Spectroscopy: theory and Applications.* Springer, Berlin. 2001

Rinia, H.A., Snel, M.M.E., van der Eerden, J.P.J.M., and de Kruijff, B. 2001. Visualizing detergent resistant domains in model membranes with atomic force microscopy. *FEBS Lett.* 501:92-96.

Rosano, C., Arosio P. , and Bolognesi, M. 1999. The x-ray three-dimensional structure of avidin. *Biomol. Eng.* 72:2117-2123.

Rossetti, F.F., Bally, M., Michel, R., Textor, M., and Reviakine, I. 2005. Interactions between titanium dioxide and phospatidyl serine-containing liposomes: formation and

patterning of supported phospholipid bilayers on the surface of a medically relevant material. *Langmuir.* 21:6443-6450.

Russel, W.B., Saville, D.A., Schowalter, W.R. *Colloidal Dispersions.* Cambridge University Press: Cambridge, 1989. Chapters 2-4.

Sackmann, E. 1996. Supported membranes: scientific and pratical applications. 1996. *Science.* 271:43-48.

Sahu, A., Soulika, A.M., Morikis, D., Spruce, L., Moore, W.T., and Lambirs, J.D. 2000. Binding kinetics, structure activity relationship and biotransformation of the complement inhibitor compstatin. *J. Immunol*. 165:2491-2499.

Schmidt, A., Spinke, J., Bayerl, T., Sackmann, E., and Knoll, W. 1992. Streptavidin binding to biotinylated lipid layers on solid supports: A neutron reflection and surface Plasmon optical study. *Biophys. J.* 63:1185-1192.

Schweitzer-Stenner, R., Licht, A., and Pecht, I. 1992. Oligomerization and ring closure of immunoglobulin E class antibodies by divalent haptens. *Biophys. J.* 63:551-562.

Schwille, P. 2003. TIR-FCS: staying on the surface can sometimes be better. *Biophys. J.* 85:2783-2784.

Sholl, D.S., Fenwick, M.K., Atman, E., and Prieve, D.C. 2000. Brownian dynamics simulation of the motion of a rigid sphere in a viscous fluid very near a wall. *J. Chem. Phys.* 113:9268-9278.

Shoup, D., Lipari, G., and Szabo, A. 1981. Diffusion controlled biomolecular relation rates. The effect of rotational diffusion and orientation constraints. *Biophys. J.* 36:697-714.

Skoog, D.A., Holler, F.J., and Niemann, T.A. 1998. *Principles of Instrumental Analysis.* Saunder College Printing/Harcourt Brace and Co., Orlando, FL.

Smith, B.A., and McConnell, H.M. 1978. Determination of molecular motion in membranes using periodic pattern photobleaching. *Proc. Natl. Acad .Sci.* 75:2759-2763.

Spinke, J., Yang, J., Wolf, H., Liley, M., Ringsdorf, H., and Knoll, W. 1992. Polymer-supported bilayer on a solid substrate. *Biophys. J.* 63:1667-1671.

Starr, T.E., and Thompson, N.L 2000. Formation and Characterization of Planar Phospholipid Bilayers Supported on TiO_2 and $SrTiO_3$ Single Crystals. *Langmuir*. 16:10301-10308.

Starr, T.E., and Thompson, N.L. 2001. Total internal reflection with fluorescence correlation spectroscopy: combined surface reaction and solution diffusion. *Biophys. J.* 80:1575-1584.

Starr, T.E., and Thompson, N.L. 2002. Fluorescence pattern photobleaching recovery for samples with multi-component diffusion. *Biophys. J.* 97:29-44.

Starr, T.E., and Thompson, N.L. 2002. Local diffusion and concentration near planar membranes: measurement by total internal reflection with fluorescence correlation spectroscopy. *J. Phys. Chem. B.* 106:2365-2371.

Stryer, L. *Biochemsitry.* W.H. Freeman and Co.: New York City, NY, 1995

Tamm, L.K., and McConnell, H.M. 1985. Supported phospholipid-bilayers. *Biophys. J.* 47:105-113.

Taylor, J. *An Introduction to Error Analysis: The Study of Uncertainties in Physical Measurements*, Oxford University Press: Mill Valley, CA, 1982.

Thompson, N.L., Burghardt, T.P., and Axelrod, D. 1981. Measuring surface dynamics of biomolecules by total internal relection fluorescence with photobleaching recovery or correlation spectroscopy. *Biophys. J.* 33: 435-454.

Thompson, N.L. 1982. Surface binding rates of nonfluorescent molecules may be obtained by total internal reflection with fluorescence correlation spectroscopy. *Biophys. J.* 38:327-329.

Thompson, N.L., and Axelrod, D. 1983. 43:103-114. Immunoglobulin surface-binding kinetics studied by total internal reflection with fluorescence correlation spectroscopy. *Biophys. J.* 43:103-114.

Thompson, N.L., McConnell, H.M., and Burghardt, T.P. 1984. Order in supported phospholipid monolayers detected by the dichroism of fluorescence excited with polarized evanescent illumination. *Biophys. J.* 46:739-747.

Thompson, N.L. Fluorescence correlation spectroscopy. In *Topics in Fluorescence Spectroscopy.* Lakowicz, J.R., Eds. Plenum Press: New York, 1991. Vol. 1, pp 337-378.

Thompson, N.L., Pearce, K.H., and Hsieh, H.V. 1993. Total internal reflection fluorescence microscopy: application to substrate-supported planar membranes. *Eur. Biophys. J.* 22:367-378.

Thompson, N.L.: Mitchell, J.L. High order autocorrelation in fluorescence correlation Spectroscopy. In *Fluorescence Correlation Spectroscopy: Theory and Applications,* Rigler, R., Elson, E.L., Eds. Springer-Verlag: Berlin, 2001, pp 438-458.

Thompson, N.L., Lieto, A.M., and Allen, N.W. 2002. Recent advances in fluorescence correlation spectroscopy. *Curr. Opin. Struct. Bio.* 12:634-641.

Thompson, N.L., and Pero, J.K. Total internal reflection florescence microscopy: applicationsin biophysics. In *Fluorescence Spectroscopy in Biology: Advanced Methods and Their Applications to Membranes, Proteins, DNA and Cells,* Wolfbeis, O.S., Hof, M., Hutterer, R., Fidler, V., Eds. Springer-Verlag: Berlin, 2005, pp 79-103.

Thompson, N.L., and Pero, J.K. Total internal reflection-fluorescence correlation spectroscopy. In *Reviews in Fluorescence.* Geddes, C.D., Lakowicz, J.R., Eds. Kluwer Academic / Plenum Press: New York, in press.

Timbs, M.M., and Thompson, N.L. 1990. Slow rotational mobilities of antibodies and lipids associated with substrate-supported phospholipid monolayers are measured by polarized fluorescence photobleaching recovery. *Biophys. J.* 58:413-428.

Ueda, M., Sako, Y., Tanaka, T., Devreotes, P., and Yanagida, T. 2001. Single-molecule analysis of chemotactic signaling in dictyostelium cells. *Science*. 294:864-867.

Vukojevic, V., Pramanik, A., Yakovleva, T., Rigler, R., Terenius, L., and Bakalkin, G., 2005. Study of molecular events in cells by fluorescence correlation spectroscopy, *Cell. Molec. Life Sciences.* 62:535-550.

Wagner, M.L., and Tamm, L.K. 2000. Tethered polymer-supported planar lipid bilayers for reconstitution of integral membrane proteins: silane-polyehtyleneglycol-lipid as a cushion and covalent linker. *Biophys. J.* 79:1400-1414.

Weiss, M., and Nilsson, T. 2004. In a mirror dimly: tracing the movements of molecules in living cells. *Trends Cell. Biol.* 14:267.

Weissman, M.B., Pan, R.C., and Ware, B.R. 1979. Electrostatic contributions to the viscosities and diffusion coefficients of macroion solutions. *J. Chem Phys.* 70:2897-2903.

Wong, J.Y., Majewski, J., Seitz, M., Park, C.K., Isrealachvili, J.N., and Smith, G.S. 1999. Polymer-cushioned bilayers. I. A structural study of various preparation methods using neutron reflectometry. *Biophys. J.* 77:1445-1457.

Wright, L.L., Palmer, A.G., and Thompson, N.L. 1988. Inhomogenous translational diffusion of monoclonal antibodies on phospholipid Langmuir-Blodgett films. *Biophys. J.* 54:463-470.

Yang, T., Jung, S., Mao, H., and Cremer, P.S. 2001. Fabrication of phospholipid bilayer-coated microchannels for on-chip immunoassays. *Anal. Chem.* 73:165-169.

Yang, Y., Wang, H., and Erie, D.A. 2002. Quantitative characterization of biomolecular assemblies and interactions using atomic force micrscoscpy. *Methods*. 29:175-187.

Yang, T., Barysnikova, O.K., Mao, H., Holden, M.A., and Cremer, P.S. 2003. Investigation of bivalent antibody binding on fluid-supported phospholipid bilayers: the effect of hapten density. *J. Am. Chem. Soc.* 125:4779-4784.

Yuan, C., and Johnston, L.J. 2000. Distribution of ganglioside GM1 in L-α-Dipalmitoylphosphatidylcholine/cholesterol monlayers: a model for lipid rafts. *Biophys. J.* 79:2768-2781.

Zhao, S., and Reichert, W.M. 1992. Influence of biotin lipid surface density and accessibility on avidin binding to the tip of an optical fiber sensor. *Langmuir* 8:2785-2791.

Zhao, S., Walker, D.S., and Reichert, W.M. 1993. Cooperativity in the binding of avidin to biotin-lipid-doped-Langmuir-Blodgett films. *Langmuir* 9:3166-3173.

Zorzano, A., Fandor, C., and Palacin, M. 2000. Role of plasma membrane transporters in muscle metabolism. *Biochem J.* 349:667-688.